Investigation of Mechanical Properties of Bulk and Additively Manufactured Ni-Mn-Ga Shape Memory Alloy using Nanoindentation and Microhardness Techniques

by

Yash Nipun Trivedi

Submitted in Partial Fulfillment of the Requirements

for the Degree of

Master of Science in Engineering

in the

Mechanical Engineering

Program

YOUNGSTOWN STATE UNIVERSITY

May, 2019

Investigation of Mechanical Properties of Bulk and Additively Manufactured Ni-Mn-Ga Shape Memory Alloy using Nanoindentation and Microhardness Techniques

Yash Nipun Trivedi

I hereby release this thesis to the public. I understand that this thesis will be made available from the OhioLINK ETD Center and the Maag Library Circulation Desk for public access. I also authorize the University or other individuals to make copies of this thesis as needed for scholarly research.

Signature:

Yash Nipun Trivedi, Student Date

Approvals:

Dr. C. Virgil Solomon, Thesis Advisor Date

Dr. Hazel Marie, Committee Member Date

Dr. Jae Joong Ryu, Committee Member Date

Dr. Salvatore A. Sanders, Dean of Graduate Studies Date

Abstract

Monocrystalline Ni-Mn-Ga magnetic shape memory alloys are known for producing reversible strains up to 10% in the presence of the magnetic field. Two main problems with the material are the high production cost and brittleness of the material. Due to complexity in manufacturing process mass production of the part becomes difficult limiting its application. High brittleness in material restricts any machining operation on both monocrystalline and polycrystalline bulk part, limiting the use of material for various applications. A possible alternative is to use porous polycrystalline Ni-Mn-Ga alloys produced using additive manufacturing process, which was first time introduced using binder jetting technology. But, little knowledge is available for both bulk and polycrystalline Ni-Mn-Ga part. The purpose of this study is to investigate the mechanical properties of bulk and 3D printed parts using nanoindentation and microhardness techniques. The methods are well known for investigation of small volumes of material with high accuracy. Two different synthesis techniques were used to prepare the bulk and 3D printed sample. Ingot for Bulk and 3D printed Ni-Mn-Ga part was produced using arc melting process. By varying the chemical composition of the alloy, two different parts with phases, namely austenitic (Ni49.12Mn22.57Ga28.31wt.%) and martensitic (Ni52.49Mn23.11Ga24.40wt.%) at room temperature were prepared. The 3D printed Ni-Mn-Ga parts (Ni51.32Mn33.06Ga15.62wt.%) were prepared from ball milled powder using binder-jet technology. The properties of interest in this research were hardness (H), elastic modulus (E), yield strength (σ_y), and fracture toughness (K_{Ic}) for all the three types of samples. Hardness (H), elastic modulus (E), and yield strength (σ_y) were determined

using nanoindentation technique while the microindentation technique was used to determine fracture toughness (K_{IC}). The fracture toughness was determined using two different types of model models based on Palmqvist and radial crack. There were three different models used based on radial crack length including, Laugier, Anstis and Niihara's model, while there were two different models based on Palmqvist crack length suggested by Laugier and Niihara. Both crack length and crack geometry were determined using light and electron microscopy investigations of the fractured nano- and micro- indents. High accuracy in crack length measurement was needed, as the models heavily depended on them. Interestingly, pseudoelastic behavior, a shape memory effect governed by external loading, was observed in austenitic and 3D printed samples during nanoindentation experiments with sharp indenter.

Acknowledgments

First, I would like to thank Dr. C. Virgil Solomon, my thesis advisor for continuously guiding me in the research work and throughout the master's program. Perfection and hard work are the two important qualities of Dr. Solomon which were the driving force for the research in this period of two years. This helped me in enhancing my skills and ability in the engineering field.

My thesis committee members Dr. Jae Joong Ryu and Dr. Hazel Marie were an integral part of this work and I would thoroughly like to acknowledge them for putting all the time and effort.

Further, I would like to thank Dr. Drew Hirt for helping me conduct all the microindentation tests at Materials Research Laboratory (MRL). Dr. Matthew Caputo and Ms. Mecedes Ferraro for helping me learn different experimental techniques for my research work.

Also, like to mention Mr. Stephen Issaco and Mr. Christopher Bansah my lab members, for helping me in conducting various experiments and putting the team spirit up in difficult times. Mr. Edward Cudjoe, Mr. Mihir Patel, Mr. Keldeep Yeola and Mr. Younus Ulus for supporting me in hard times and being my family away from home.

I would also like to thank my parents Mr. Nipun Trivedi and Mrs. Rindu Trivedi, my brother Mr. Maitray Trivedi and my grandparents Mr. Vishnukant Trivedi and Mrs. Damyanti Trivedi for giving me moral support and help me in achieving my goals. They are my inspiration and role model in life, and would like to dedicate this work to them.

Table of Contents

List of Figures

List of Tables

Chapter 1 Introduction

1.1 Background

In the era of miniaturizing the mechanical systems and drives, need for discovering new functional materials with extraordinary material properties is needed. Some of the alloys with the functional property of shape recovery are nickel-based alloys, and particularly Ni-Ti and Ni-Mn-Ga are well known among them. Ni-Mn-Ga alloy is in the center of focus in this research, due to the shape memory effect (SME) found in material governed by a magnetic field. [1] Magnetic shape memory (MSM) effect is governed by two phenomena (1) magnetically induced reorientation of martensitic variants and (2) magnetically induced martensitic phase transformation. [2] It is easy to reorient the martensitic twin boundaries and produce magnetic field induced strain (MFIS) when compared to phase transformation into induced martensitic phase. It is more feasible to design actuators governed by shape memory effect due to twin orientation since the small magnetic field generated by the conventional electric magnet is enough for actuation. [3] It was demonstrated, that single crystal Ni-Mn-Ga alloy has magnetic field induced strain (recoverable strain) up to 10% which is unique among shape memory alloys.[4]–[6] With such a high strain recovery we can simply replace a whole system with just a single part made from Ni-Mn-Ga alloy. For example, producing a component of 10 mm in length using Ni-Mn-Ga alloy would have a stroke length of 1 mm in a particular direction only with help of twin re-orientation when brought under particular direction of the magnetic field. Some of the important properties of material include high thermal stability and large magnetic field induced strain under a low magnetic field, which makes Ni-Mn-Ga

predominant among other shape memory alloys. [5] Ni-Mn-Ga can be produced in many different forms according to its application. The known forms of Ni-Mn-Ga alloy are: (1) bulk monocrystalline and polycrystalline - made by melting the pure metals together couple of times [1],[5]–[11], (2) Ni-Mn-Ga alloy thin films - produced by sputtering Ni-Mn-Ga on different material substrates [4], [12]–[16], (3) Ni-Mn-Ga alloy foams – produced by replication method [17],[18], (4) powder metallurgy of Ni-Mn-Ga alloy, [3] and (5) additively manufactured parts of Ni-Mn-Ga alloy. [19]- [21] Efforts have been made to produce thin films from Ni-Mn-Ga alloy to investigate the mechanical properties and compare the results with the bulk material. This was because of the poor mechanical properties of bulk Ni-Mn-Ga part. [4] Later on, it was demonstrated that thin films possess better mechanical properties such as elastic modulus and hardness than the bulk part. More importantly, results depicted improved ductility, which was a major issue with bulk samples. Use of 3D printing technology for printing Ni-Mn-Ga parts is the most recent discovery. [19], [20] The method used for printing Ni-Mn-Ga powder is called binder jetting technology, where the powder is bind together layer by layer using special binder resin.

1.2 Applications of Ni-Mn-Ga alloy

There are many anticipated applications of Ni-Mn-Ga alloy in the field of miniaturized devices. Some of them are for manufacturing highly sensitive actuator switches and sensors. These sensors and actuators can be governed using the external magnetic field, which would trigger the shape memory effect. [7], [22] Due to shape recovery taking place at a rapid pace under the applied magnetic field, sensors built using Ni-Mn-Ga alloy could be used for high frequency applications. [4] This would help in

replacing a whole system with just a single part made from the alloy. Some of the other applications of the material include damping the vibrations in small systems. It is because the material can stay stiff or can oscillate with the frequency of the system under a controlled magnetic field surrounding. A direct phase transformation from paramagnetic austenite to ferromagnetic martensite in a Ni-Mn-Ga thin film was used in several actuation mechanisms. It was used for applying bending, torsion, tension or any combination of these motions. [12] Based on the mechanism discussed in a study, an optical micro-scanner was developed with a wide range of scanning angles and operation frequencies. More than 20,000 worldwide patents were issued on shape memory alloy (SMAs) applications, although viable products from the intellectual property are limited. Some of the studies even suggested the replacement of commercial electric motors, pneumatics, and hydraulics is possible to be done using microactuators made from SMAs. [23] The mechanical systems and drives governed by the SME of Ni-Mn-Ga alloy would also help in replacing the commercially used sensors in different instruments. With the advancement in technology, this material could be used more efficiently and at the same time, it is also eco-friendly which would help in attaining sustainable development. Magnetic materials have been used for advancement in computer peripherals such as voice coil motors and actuators. It helps in both decreasing the size as well as enhancing the work performance. [24] There are many efforts done to manufacture and use Ni-Mn-Ga polymer composites. The polymer and alloy powder are mixed to make a composite material, which is then vacuum treated to remove air bubbles from the mixture. It is cured in the air with a magnetic field of 0.5T. Moreover, thermo-mechanical magnetic training is done to enhance the MSME of the composite. [2] Some of the shape memory alloys

(SMAs) are governed by the change in surrounding temperature and are known as high temperature magnetic materials (HTMM). Efforts to decrease coercivity in HTMM have been made, to minimize eddy current losses in the material. They can be used for power generation and conversion application. [25] It is again a complex discussion but helps us understand the importance of shape memory alloys and their ability.

1.3 Challenges with Ni-Mn-Ga alloy

Ni-Mn-Ga alloy has many unique properties, but there are few drawbacks of the material as well. Brittleness of the material is limiting the use of the alloy in many applications.[5], [6], [8], [13] Due to the brittleness of material it becomes almost impossible to do any kind of machining operations on it. Therefore, it becomes very difficult to manufacture the material into complex shapes and hence could be used in limited applications. Efforts have been made to change the mechanical properties by using different chemical composition, but care has to be taken that it does not affect the shape memory effect. Combinational studies regarding fatigue life of the material are done to acquire knowledge regarding material behavior against fracture and to do efficient use in micro-scale actuators. The study included determining the life span of the component made from Ni-Mn-Ga alloy, so as to predict the failure and further work on improving the mechanical properties according to the requirements. [9] Many case studies included altering the chemical compositions of the alloy. Attempts to reduce the amount of gallium metal and add boron to the alloy were done, to enhance the mechanical properties of the material. [5] The experiment gave some fruitful results, as there was an appreciable increase in the material hardness. On the contrary due change in

composition, it altered the phase transformation temperature of the material. Many case studies focused on controlling the elastic modulus value of Ni-Mn-Ga alloy by replacing nickel with gallium when the material is in the austenitic phase. It was discovered that by substitution of nickel with gallium, there was an increase in elastic modulus values for material in the austenitic phase. But, apparently had a negative effect on martensitic phase property, as they encountered a decrease in elastic modulus value. [7] Corrosion and passivation behavior of polycrystalline Ni-Mn-Ga alloy was the center of focus in one of the researches. Here reaction with the environment and its effect on structural strength due to corrosion was investigated. [26] Bulk Ni-Mn-Ga alloy parts with only austenitic and only martensitic phase were prepared for tests. They were then dipped into an acidic solution (pH<5) simultaneously. Higher reactivity in the martensitic phase sample was detected which was mainly due to enhanced dissolution processes occurring at multiple twin boundaries. In conclusion, free corrosion and passivation activity of the Ni-Mn-Ga alloy depends on the phase as well as the composition of the alloy. [26]

In thin films, experiments with different film thickness, substrate material, and deposition temperature were done to see the effect on mechanical properties.[4], [13]–[15] There were considerable changes in hardness and elastic modulus values of the material with changes in the film thickness. It was demonstrated that there was a decrease in elastic modulus and hardness of the material due to an increase in film thickness. Many different experiments with the heat treatment of the alloy after producing the part were carried out by annealing it at a particular range of temperatures for the different time period. [10], [14] It was found that an increase in annealing temperature enhances the mechanical properties if done for a limited time period. One of the case studies was based

on the polishing technique used to get a mirror like surface. It suggested that the polishing technique affects the hardness value as the surface roughness changes. Samples that were electrochemically polished had reduced hardness values, as compared to mechanically polished samples. [9] Different concentration gradient covering a large composition range were produced from diffusion couples of selected Ni-Mn-Ga alloys. These couples with various compositions of Ni-Mn-Ga alloy were then assembled and annealed. Nanoindentation technique was used to analyze the diffusion couples. Results obtained from the indentation hardness and elastic modulus showed very scattered values for martensitic sample. It was concluded that the results were affected due to twin variants present in the martensitic phase. [10]

1.4 Additively manufactured Ni-Mn-Ga alloy parts

Additive manufacturing (AM) of Ni-Mn-Ga alloy is an innovative technique. The sparse information on mechanical properties of AM Ni-Mn-Ga parts has drawn certain attention lately. It is, therefore, one of the main reasons of this research to thoroughly understand the mechanical behavior of the material. Further, one of the biggest advantages of 3D printing technique is its ability to produce complex shaped parts, with high accuracy. This increases the material feasibility and application in various fields. Thus, the purpose of the present research is to investigate and determine the mechanical properties of this material when produced using a 3D printing technique. As we discussed before, one of the challenges is the weak mechanical properties of the material. Also, there are many issues due to the high production cost of Ni-Mn-Ga alloy. For this research limited quantities of powder had been produced using laboratory set-up. It is not feasible to produce a dog bone specimen from the material and do tensile testing. This

again increases the challenges related to the methodology used for investigating mechanical properties of the material. Nanoindentation is one of the testing techniques well known among mechanical testing of materials at the nanoscale. This technique was used in this research and will be discussed in the next section.

1.5 Importance of nanoindentation technique

Some of the important applications of the material are at the microscale level, and so the knowledge of the mechanical properties of the material at micro and nanometer scale is required. Care must be taken while carrying out mechanical testing of the material as it will be eventually used for the development of miniaturized devices. And to actually compensate this, nanoindentation testing for evaluating the mechanical properties was considered to be most appropriate. [4] It must be noted that nanoindentation is very helpful in understanding the mechanical behavior of the material at nanoscale. Mechanical properties such as hardness (H), and elastic modulus (E) can be accurately determined using nanoindentation technique. Results such as 'Elastic recovery ratio' and the ratio of residual depth to maximum indentation depth (h_r/h_{max}) obtained from nanoindentation depth also helps in understanding the mechanical behavior of the material. Nanoindentation technique, due to its ability to probe mechanical properties for small volumes, helps in measuring mechanical properties in relation with grain orientation and hence in estimating the anisotropy. Investigation for relating the mechanical properties with the crystallographic orientation has also been carried out using electron backscattered diffraction technique (EBSD) in the scanning electron microscope (SEM). [6] It helps in scrutinizing the results and have a better understanding of material behavior in certain predefined loading conditions. Correlation between the

grain size and mechanical properties of the material were also investigated in a study, which will eventually be related to the magnetic property of the material. [6] Ni-Mn-Ga thin films were tested in the research, as the end goal was to design a MEMS device. They concluded that there was a decline in the hardness of the material with an increase in grain size, which they proposed was consistent with the Hall-Petch effect. All these case studies were done using nanoindentation technique, so as to determine local mechanical properties of the material at different spots. [13] [27] It was also accounted that nanoindentation is used to investigate local mechanical properties of engineered surfaces, composites, hierarchical biological tissues such as bones and teeth, and microelectromechanical systems and other miniature devices. [16] [28] This was possible only due to the high spatial resolution possessed by nanoindentation. Thus, the nanoindentation technique was used for determining the hardness (H), elastic modulus (E) and yield strength (Y) of Ni-Mn-Ga bulk and 3D printed part produced from Ni-Mn-Ga powders.

1.6 Importance of microhardness testing

Furthermore, another mechanical property investigated in this research was fracture toughness (K_{IC}) of material. It was found while doing a compression test on Ni-Mn-Ga 3D printed part that the material cracked in two different ways: (1) inter-granular cracking and (2) trans-granular cracking. [29] Inter-granular cracking takes place by crack propagation along grain boundary, while in transgranular cracking the crack propagates across the grain. This was a unique phenomenon and was interesting to understand the factors affecting the crack propagation, as well as crack orientation in 3D printed material. It becomes important to understand the nature of the material, as it could

be disadvantageous in many ways. If components made from Ni-Mn-Ga alloy would have uncertainty in failure, eventually it might lead to a system failure. Such encounters were noted, and it was observed that the material failed after a relatively small number of cycles, leading to a loss in material performance. Combinatorial study of the influence of the magneto-mechanical loading on the growth of already nucleated cracks was also studied. [11] It was concluded from the study that fracture toughness depends on the magneto-mechanical loading conditions and stated that it could be confirmed that material was brittle in nature. Further, it suggested that crack nucleation was caused due to hoop stress and depending on the ratio of the applied magnetic field to compressive stress. It was documented that high material instability was encountered as it switched from austenite to martensite. [11]

It is to be noted here that the parts tested in the present research were bulk and 3D printed monocrystalline part and microhardness tester was used instead of nanoindentation machine for conducting fracture toughness analysis. There are again several aspects to it which we shall further discuss in the experimental methodology chapter. One of the case studies determined that the extreme brittleness of the material was attributed due to fracture along the low strength grain boundaries. It is a result of high directionality of the bonds in the ordered structure which breaks down at the grain boundaries. [6] Also, their coarse-grained microstructure combined with large mechanical anisotropy was susceptible to intergranular cracking. Thus, investigating the crack orientation and then the crack propagation for determining the fracture toughness of Ni-Mn-Ga bulk and 3D printed part became one of the important aspects of this research. Microhardness tester was used to investigate all the samples and determine the cracking

force. Again, to broaden the study, the 3D printed parts were sintered for three different time periods and then tested for fracture toughness. Table 1-1 shows the chemical composition, heat treatment, and mechanical properties obtained from the case studies available for Ni-Mn-Ga alloy. It is important to note the change in the mechanical properties of the alloy with the slightest change in chemical composition, making, or post heat treatment.

Table 1-1 Summary of Mechanical Properties (H and E)

No.	Material	Chemical composition	Methodology	Heat treatment	H (GPa)	E (GPa)	Ref.
1	Ni-Mn-Ga (A)	$Ni_{52}Mn_{18}Ga_{30}$	Re-melted 5 times using arc melting in Argon atmosphere	Homogenization heat treatment at 1223 K for 168 hrs	-	85 to 135	[7]
2	Ni-Mn-Ga (B)	$Ni_{46}Mn_{30}Ga_{24}$	Re-melted 5 times using arc melting in Argon atmosphere	Homogenization heat treatment at 1223 K for 168 hrs	-	85 to 135	[5]
3	Ni-Mn-Ga (C)	$Ni_{52}Mn_{30}Ga_{18}$	Re-melted 5 times using arc melting in Argon atmosphere	Homogenization heat treatment at 1223 K for 168 hrs			
4	Ni-Mn-Ga (D)	$Ni_{58}Mn_{18}Ga_{24}$	Re-melted 5 times using arc melting in Argon atmosphere	Homogenization heat treatment at 1223 K for 168 hrs			

No.	Material	Chemical composition	Methodology	Heat treatment	H (GPa)	E (GPa)	Ref.
5	Ni-Mn-Ga	$Ni_{51}Mn_{28.5}Ga_{20.5}$	Vacuum arc melting in water-cooled Cu crucible	Annealed at 1073 K for 72 hrs	2.35 (240 HV)	-	[5]
6	Ni-Mn-Ga thin film. [Glass (4.1) substrate] 2" diameter	$Ni_{50}Mn_{30}Ga_{20}$	D.C. magnetron sputtering under Ar atm. of 0.01 mbar. Sputtering power of 36W	-	5.35	100.3	[4]
7	Ni-Mn-Ga thin film. [Si(100) substrate] 2" diameter	$Ni_{50}Mn_{30}Ga_{20}$	D.C. magnetron sputtering under Ar atm. of 0.01 mbar. Sputtering power of 36W	-	5.51	151.2	
8	Ni-Mn-Ga thin film. [Glass (2.4) substrate] 2" diameter	$Ni_{50}Mn_{30}Ga_{20}$	D.C. magnetron sputtering under Ar atm. of 0.01 mbar. Sputtering power of 36W	-	3.25		
9	Ni-Mn-Ga Bulk material	$Ni_{50}Mn_{26.25}Ga_{23.75}$	Grain orientation (010)	Vacuum arc melting using 99.8% pure elements	3.7 ± 0.04	81 ± 0.7	[6]

No.	Material	Chemical composition	Methodology	Heat treatment	H (GPa)	E (GPa)	Ref.
10	Ni-Mn-Ga Bulk material	$Ni_{50}Mn_{26.25}Ga_{23.75}$	Grain orientation (231)	Vacuum arc melting using 99.8% pure elements	3.39 $\pm$ 0.05	69.2 $\pm$ 0.7	[6]
11			Grain orientation (120)	Vacuum arc melting using 99.8% pure elements	3.3 $\pm$ 0.04	70.2 $\pm$ 0.7	
12			Grain orientation (121)	Vacuum arc melting using 99.8% pure elements	3.2 $\pm$ 0.03	64.8 $\pm$ 0.6	
13			Grain orientation (232)	Vacuum arc melting using 99.8% pure elements	2.9 $\pm$ 0.06	58.9 $\pm$ 0.8	
14	Ni-Mn-Ga	$Ni_{52}Mn_{18}Ga_{30}$	Vacuum arc melting in Ar atm.	Annealed at 1223.15 for 168 hrs	3.5 to 6	85 to 130	[10]
15	NMGRT 300	$Ni_{49.6}Mn_{30.6}Ga_{19.8}$	Vacuum arc melting	Annealing At 673 K for 30 min	0.8	3.6	[15]
16	NMG500 500		Vacuum arc melting	Annealing At 673 K for 30 min	5.3 $\pm$0.6	69.7 $\pm$11.2	

No.	Material	Chemical composition	Methodology	Heat treatment	H (GPa)	E (GPa)	Ref.
17	NMG600 600	$Ni_{49.6}Mn_{30.6}Ga_{19.8}$	Vacuum arc melting	Annealing At 673 K for 30 min	6.8 ±0. 6	103 ± 7.09	[15]
18	Ni-Mn-Ga (single crystal)	$Ni_{50.4}Mn_{28.3}Ga_{21.3}$	Electropolished	-	3.2-3.8	-	[9]
19	Ni-Mn-Ga (single crystal)		Mechanically polished	-	3.9-6.3	-	
20	Ni-Mn-Ga (A)	$Ni_{43.8}Mn_{29.2}Ga_{27}$	Sputtering for 30 min. Thickness- 1.5 µm	Post annealed at 823K for 1 hour	5.5	155	[15]
21	Ni-Mn-Ga (B)	$Ni_{43.8}Mn_{29.2}Ga_{27}$	Sputtering for 50 min. Thickness- 2.4 µm	Post annealed at 823K for 1 hour	4.2	125	
22	Ni-Mn-Ga (C)	$Ni_{43.8}Mn_{29.2}Ga_{27}$	Sputtering for 90 min. Thickness- 4.0 µm	Post annealed at 823K for 1 hour	3	110	
24	Ni-Mn-Ga Substrate Temp. 400 °K	$Ni_{49.9}Mn_{29.0}Ga_{21.1}$	DC Magnetron sputtering	No Annealing	4.92± 0.27	79±4	[13]

No.	Material	Chemical composition	Methodology	Heat treatment	H (GPa)	E (GPa)	Ref.
25	Ni-Mn-Ga Substrate Temp. 450 °K	$Ni_{49.1}Mn_{28.9}Ga_{22.0}$	DC Magnetron sputtering	No Annealing	4.17± 0.21	66±3	[13]
26	Ni-Mn-Ga Substrate Temp. 500 °K	$Ni_{49.9}Mn_{27.2}Ga_{22.9}$	DC Magnetron sputtering	No Annealing	1.11± 0.17	24±5	

Table 1-2 Summary of Mechanical Properties (K_{IC})

No.	Material	Chemical composition	Methodology	Surface no.	(K_{IC}) (MPa √m)	Ref.
27	Ni_2-Mn-Ga	$Ni_{50}Mn_{28.5}Ga_{21.5}$	Vacuum arc melting	Surface-1	6.55	[11]
28	Ni_2-Mn-Ga	$Ni_{50}Mn_{28.5}Ga_{21.5}$	Vacuum arc melting	Surface-2	9.25	

Chapter 2 Experimental and Numerical Methodology

2.1 Synthesis of bulk Ni-Mn-Ga alloy

The main ingredients of the alloy, nickel, manganese, and gallium were melted together using arc melting process. High purity Ni (99.99 at%), Mn (99.95 at%) and Ga (99.99 at%) metal were used to produce two distinct ingots one having austenitic phase at room temperature and the second one being in pure martensitic phase at room temperature. Table 2-1 shown below documents the chemical composition of the two ingots prepared using arc melting process.

Table 2-1 Chemical composition of bulk samples

Material	Phase	Chemical composition wt. %
Ni-Mn-Ga alloy (bulk)	Austenitic phase	Ni49.12Mn22.57Ga28.31
Ni-Mn-Ga alloy (bulk)	Martensitic phase	Ni52.49Mn23.11Ga24.40

The high purity elements were melted in Edmund Buhler GmbH MAM-1 arc melting furnace shown in Fig. 2-1. Electrical breakdown of inert gas produces continuous electrical discharges, known as an 'arc'. The source, an electrical current, is passed through a nonconductive medium, which in this case is ultra-high purity (UHP) argon gas. The arc relies on thermionic emissions of electrons from the tungsten electrode, creating high temperatures which depend on the voltage applied and creates visible lightning kind of arc. The melting of the Ni-Mn-Ga alloy is conducted under a positive argon pressure (0.05 - 0.07 Bar). [30] The ingot was hammered to break into pieces and re-melted a couple of times to confirm the homogeneity throughout the alloy. These ingots were further bisected into two pieces using a diamond wafer blade. The cut pieces

were heat treated at 1273 K for 24 hr. in quartz tube under UPH argon gas. The heat treatment is done to ensure chemical homogenization. After homogenization, ingots were sliced using a diamond blade mounted on Buhler Isomet-1000 low-speed precision saw machine.

Figure 2-1 Edmund Buhler GmbH MAM-1 arc melting furnace

The bulk samples were further polished using different size Si grit papers to obtain a mirror like surface. While conducting the polishing process, the formation of plastically deformed layers takes places at the material surface due to polishing action. Also, the debris or small particles of the material formed from scratches are still present on the polished surface. To remove those strained layers and contamination on the surface, cloth polishing was done for about 10 to 15 mins, with very small pressure. Further, the samples were electrochemically etched to reveal the microstructures like grain boundaries

and also twin boundaries present in case of the martensitic sample. Detail discussion on the etching process is done in section 2.3.

2.2 Additive manufacturing of Ni-Mn-Ga parts (3D printing)

Several ingots with chemical composition as shown in Table 2-2, were prepared using arc melting process. Ingots were heat treated to confirm the homogenized throughout the material.

Table 2-2 Chemical composition of the material used for 3D printed samples

Material	Phase	Chemical composition wt. %
Ni-Mn-Ga (3D printed)	Austenitic and martensitic phase	Ni51.32Mn33.06Ga15.62 (wt %)

Once the ingots were heat treated, they were sliced into small pieces using the diamond blade and Buhler Insomet-1000 instrument. They were then placed in a zirconia crucible with two zirconia milling balls. The vessel containing the zirconia balls and ingot was then placed in SPEX Sample Prep mixture 8000M ball mill. Due to milling action, the ingots were converted into powders. After ball milling process the powder was sieved to a size less than 100 μm. The detail information regarding the powder characterization, XRF, and SEM analysis could be found in other research dissertation. [30] The powder with size < 100μm was used for 3D printing the part. X1-Lab machine, by ExOne, was used for conducting binder jetting 3D printing to produce the parts. For the nanoindentation and microindentation testing the cubes with dimension, 5 mm x 5mm x 5

mm and cylinders were printed which can be seen in Fig. 2-2 and 2-4. The 3D printed parts were cured and further sintered to increase mechanical strength.

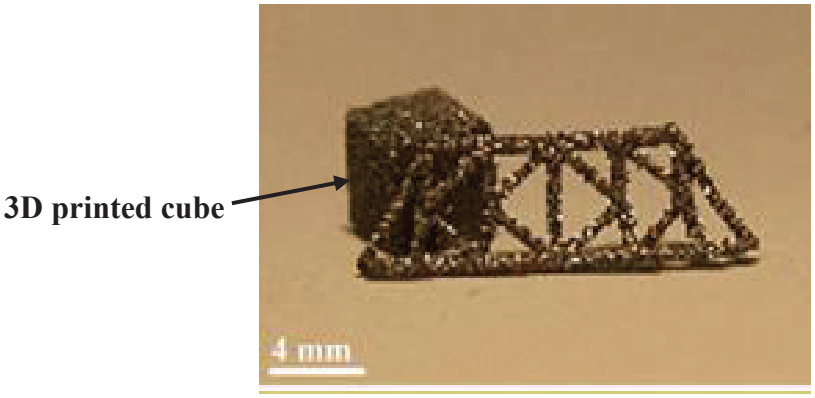

Figure 2-2 3D printed Ni-Mn-Ga parts [30]

There were three 3D printed parts sintered at 1353 K temperature at for three different time period. Sample-1 was sintered for 24hrs, sample-2 for 40 hrs. and sample-3 was sintered for the longest time period, 50 hrs., respectively. All the samples were entrapped in a quartz tube with high vacuum, which is then purged three times with argon to remove all the oxygen in the tube. It is really very important to prevent any oxygen from entering the tube, as it would oxidize the sample very fast. Fig. 2-3 depicts the image of an oxidized sample due to the presence of oxygen in the quartz tube during the sintering process.

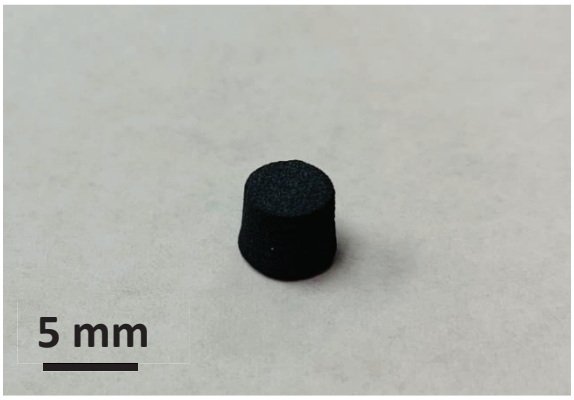

Figure 2-3 Oxidized 3D printed sample

The cross-sectional surfaces of the 3D printed parts were then polished using high number grit size Si papers. A mirror like polished surface was produced which was further cloth polished using MasterPolish 0.05 μm was polishing liquid from Buehler to remove stress layers. Fig. 2-4 shows the polished surface of 50 hrs. sintered sample supported rigidly on an SEM stub.

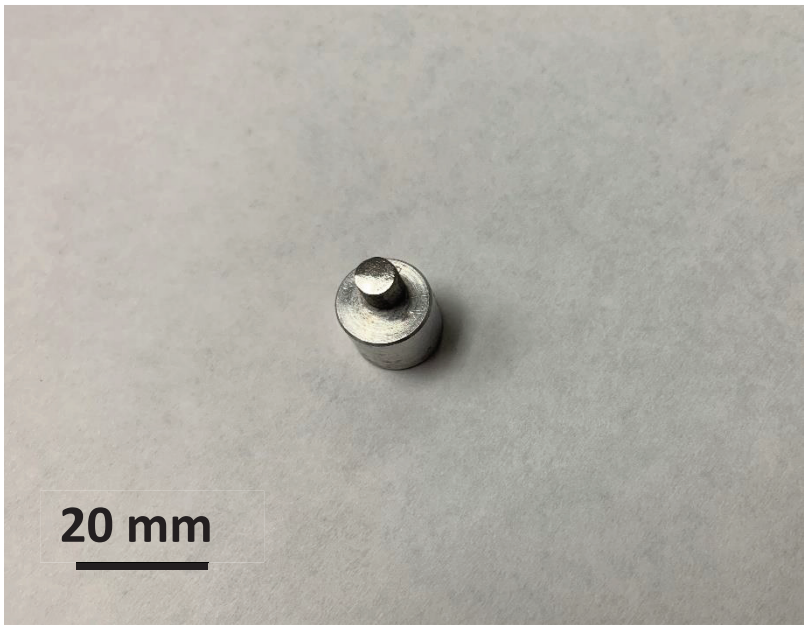

Figure 2-4 50 hrs. sintered 3D printed sample glued on a SEM stub

2.3 Electrochemical Etching

The mirror polished surfaces were further etched to reveal their microstructures. Two different methods were used to etch Ni-Mn-Ga sample: (1) chemical etching, and (2) electrochemical etching. For chemical etching, the solution used was Nital (70 % Ethanol + 30 % Nitric acid, by vol. %). In this case, the chemical instantly attacked the polished surface and the process was so quick and intense that it created big pores on the surface. These pores were not favorable for nanoindentation testing and so the samples were

eventually etched using electrochemical etching technique. Fig. 2-5 shows the surface after conducting the chemical etching. As visible from the figure, there are large pits all over the surface of the sample which would affect the nanoindentation tests.

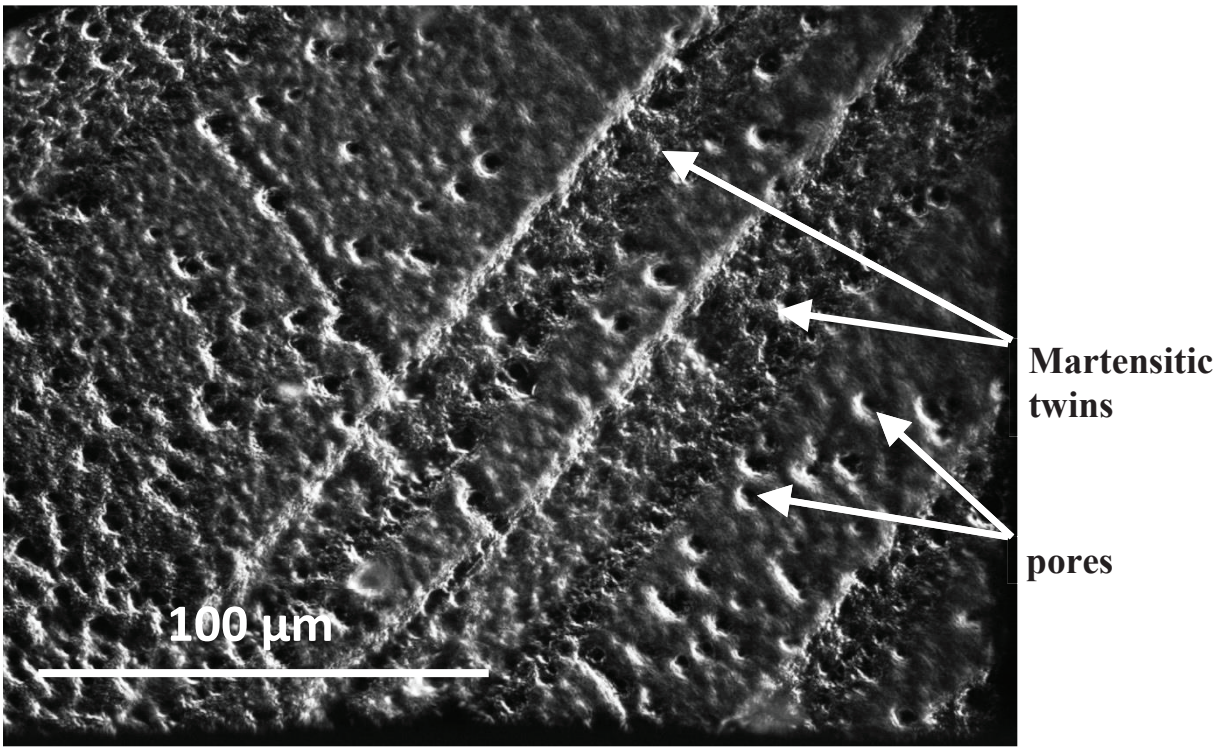

Fig. 2-5 Dark field light microscopy image of martensitic sample after chemical etching

If the nanoindent is done near the pit or in the pit, the result obtained will not have the true depth of indent and thus cannot be considered accurate. Therefore, the electrochemical etching technique was used to etch the polished samples. The results from electrochemical etching were better than chemical etching, as the pit size decreased. Also, it did not contaminate or destroy the surface, providing a large area for nanoindentation testing. In electrochemical etching, the sample acts as an active electrode while the etchant works as an electrolyte.

There are several aspects which must be considered while doing the electrochemical etching which includes the etching temperature, amount of voltage applied to the circuit, as well as etching rate. At the beginning of the test, the optimum parameters for etching were not known, due to which a separate investigation was carried out for different voltage and etching rates. The ingots were further cut into three pieces for testing a number of samples, one after another. The difficulty with the process was, once the test failed the sample had to be re-polished with 1000 to 4000 grit size Si paper till it again had a mirror polished surface. Fig. 2-6 shows the Struers-POLECTROL instrument used for electrochemical etching.

Figure 2-6 Struers-POLECTROL electrochemical etching instrument

Again, the same nital etchant was used as an electrolyte in electrochemical etching. [31] Voltage is the first parameter which was changed by keeping etching rate and intensity same for the first few tests. It was found that high voltage produces more heat while etching and is very rigorously destructing the polished surface. Thus, keeping a very low voltage, of 2-3 V, the intensity or the current (ampere) flow was adjusted. It was found

that, lower the intensity, slower the etching process. Also, by controlling the current flow, the polished surface was intact with a very small removal of the material, layer by layer. Many parameters were tried and tested before defining the optimum parameters for etching the Ni-Mn-Ga samples. The etched sample was rigorously cleaned and sonicated with de-ionized water and methanol, right after the etching process was done. They were sonicated for about 10 to 12 mins with methanol and de-ionized water one after another, which is very important to stop any further reaction of the material with oxygen in the atmosphere.

First few tests were done at room temperature which was not very favorable and almost raptured the sample surface. This helped in defining that that etching was very intense and had to be done at a low temperature around 243 K to 253 K to decrease the reaction rate. Fig. 2-7 shown below depicts the surface of the martensitic sample which was electrochemically etched at room temperature (300 K).

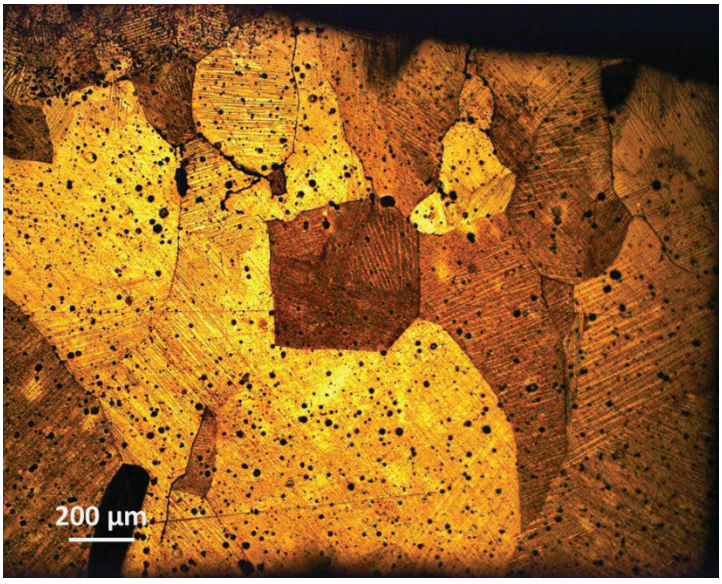

Figure 2-7 Bright field light microscopy image of the electrochemically etched martensitic sample at room temperature

Due to the failure in the etching process, all the remaining test were done at a temperature below 273 K which helped in decreasing the reaction rate and surface destruction. Also, the samples should be wiped using cotton wipes and not the paper wipes as there are chances of making small scratches while wiping them.

Light microscopy images of a properly etched surface are shown in Fig. 2-8 and Fig. 2-9. Fig. 2-8 shows the surface of austenitic phase sample while Fig. 2-9 depicts the martensitic sample surface etched electro-chemically below 273 K. From the micrographs, the grain boundaries, as well as twin boundaries with small pits all over the surface, are visible. By comparison of Fig. 2-7 and Fig. 2-9 we can see that the pit size reduced to a great extent, as well as a decrease in pit density.

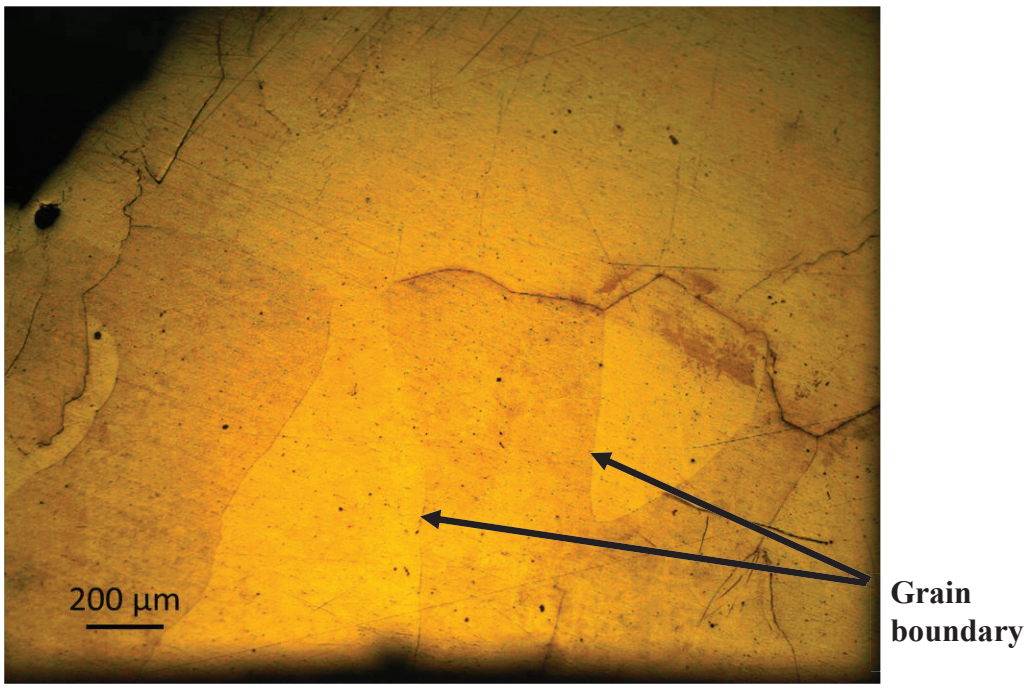

Figure 2-8 Bright field light microscopy image of austenitic phase sample (number 10 from Table 5)

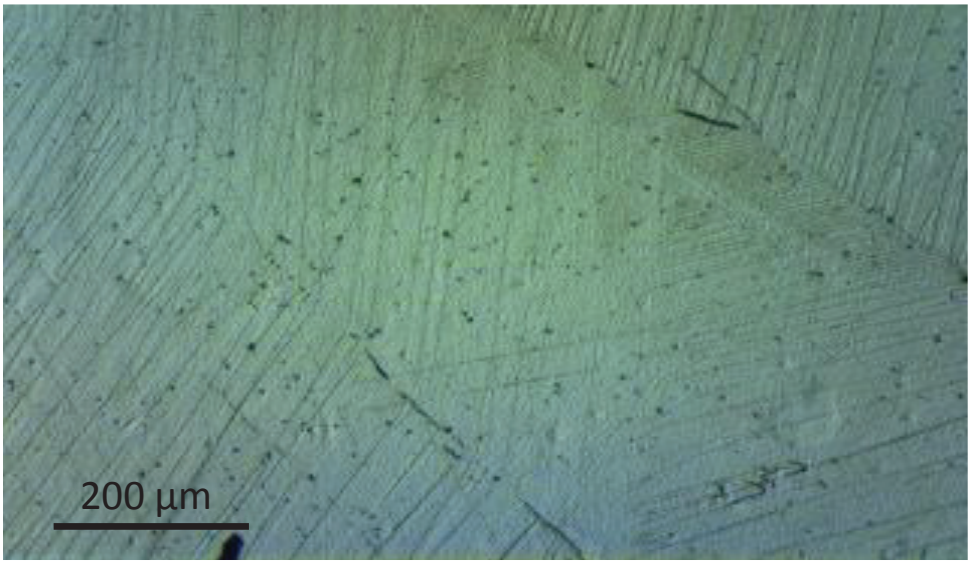

Figure 2-9 Bright field light microscopy image of martensitic phase sample (number 11 after etching from Table 5)

The summary of results from the etching process is shown in table 2-3 shown below.

Table 2-3 Summary of result from the etching process

Sample number	**Phase**	**Parameters used**	**Comments**
1	Martensitic	t = 4 mins T = 295 K (room temperature) V = 4V	• Surface etched too much. • Pits all over the surface.
2	Martensitic	t = 2 mins T = 295 K V = 4V	• Surface etched properly. • Too many big pits.

Sample number	Phase	Parameters used	Comments
3	Austenitic	t = 5 mins T = 243 K V = 4.1 V	• Pit size small, but surface ruptured. • Contamination on the surface of the sample due to the reaction after etching. • ***Clean the sample in methanol after etching is done to stop the reaction.*** • Etching time was OK.
4	Austenitic	t = 3 mins T = 243 K V = 4.1 V	• Pit size decreased. • Grain boundary visible only in the dark field.
5	Austenitic	t = 7 mins T = 243 K V = 4.1 V	• Surface etched too much. • Large pits all over the surface.
6	Martensitic	t = 5 mins T = 243 K V = 4.1 V	• Twin boundary revealed. • Surface properly etched. • Pits all over the surface.
7	Martensitic	T = 243 K V_1= 1 V (6 min) V_2 = 3.5 V (1-2 min) (not so favourable)	• Surface etched, and twin boundary visible. • ***Small scratches all over the surface due to Kim wipe. Use cotton wipes to avoid it.*** • ***Surface contamination occurs due to repetitive use of the same electrolyte.*** • ***Change electrolyte after every 2 or 3 samples.***

Sample number	Phase	Parameters used	Comments
8	Martensitic	T = 243 K V_1 = 1.5 V (3 min) V_2 = 4 V (4 min)	• Parameters favourable for etching. • Pit size large due to etching at high voltage. • Etching at lower voltage may help in getting a shiny surface.
9	Austenitic	V = 3V t = 5 min T = 243 K	• Pit size decreased and grain boundary visible very well. • Small surface cracks produced through grain boundary. • The decrease in etching time may help.
10	Austenitic	V = 2V t = 11 min T = 243 K	• Etching parameters very favourable. • Pit size very small as compared to indent size. • Pit all over the surface. • The surface is not ruptured and is shiny. • Surface contaminated as it was not cleaned with methanol to stop reactions. • Use of plasma etching to clean the contamination, which helped up to a limit.

Sample number	Phase	Parameters used	Comments
11	Martensitic	V_1 = 2.5 V (5-8 min) V_2 = 3 V (less than 2 min) T = 243 K (or less) Check sample after every minute when working at high voltage.	• Twin boundary visible very well • Pit size very small. • No surface destruction, or any depression on the sample. • Etched with fresh electrolyte helped in decreasing the contamination.
12	Austenitic	V_1 = 3.5 V (3 min) V_2 = 4.0 V (1-2 min) T = 243 K	• Pit size large and spread all over the surface. • Grain boundary visible.

In conclusion, sample number 10 and 11 showed the best results and gave the best surfaces as compared to others. A minor change in parameters and use of fresh electrolyte can give the required surface for both the phases.

2.4 Nanoindentation testing

In this technique, nanoscale indents were done on the surface of the sample using different shaped nanoindenters. The projected area of the indent is calculated using the dimensions of the indenter as well as depth at maximum load. [32], [33] The shape of the load-displacement curve is often found to be a rich source of information, not only for providing a means to calculate modulus and hardness of the specimen material, but also for the identification of non-linear events such as phase transformations, cracking, and

delamination of films. [34] Fig. 2-10 shows the nanoindentation instrument, Nanovea M1 hardness tester used in this research.

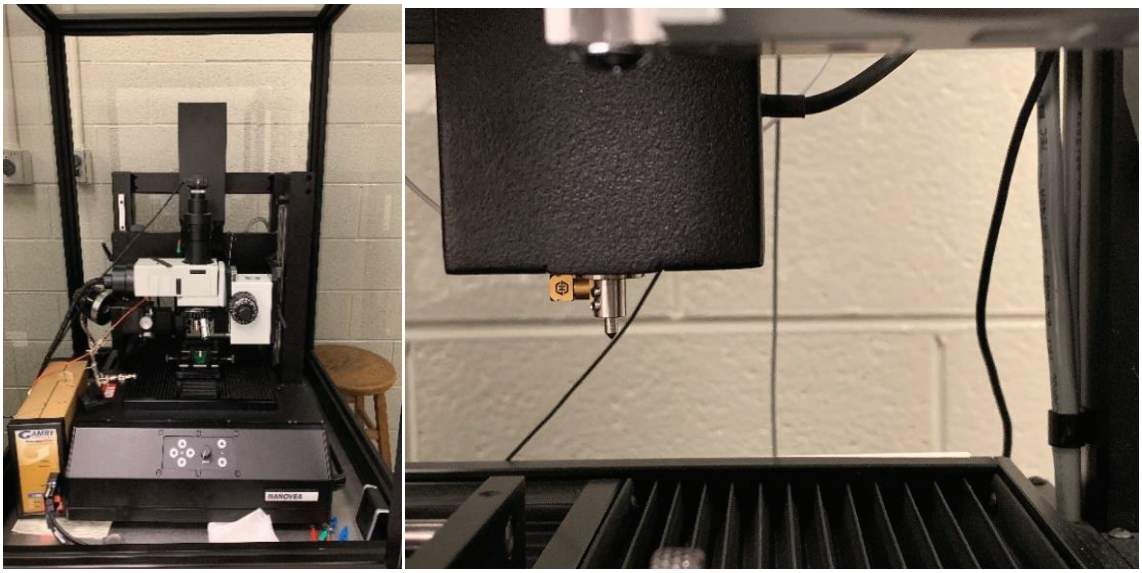

(a) (b

Figure 2-10 (a) Front view of Nanovea M-1 Hardness Tester instrument (b) Detail view show indenter unit

Different types of indenters are used, according to the mechanical property to be calculated. The mechanical properties investigated in this research are hardness (H), elastic modulus (E) and yield strength (Y). Two different types of indenters were used in nanoindentation testing: (1) Berkovich indenter and (2) flat tip indenter.

2.4.1 Hardness (H)

Fig. 2-11 (a) depicts the typical loading-unloading curve obtained while conducting a nanoindentation test. The indenter displacement or penetration depth versus the change in load is plotted on a graph by the software which helps in determining the mechanical properties. [35], [36] Berkovich indenter (three-sided pyramidal shaped indenter) shown

in Fig. 2-11 (b) and (c) was used for hardness testing, as the sharp tip penetrates the material surface easily and the plastically deformed area generated is clearly visible.

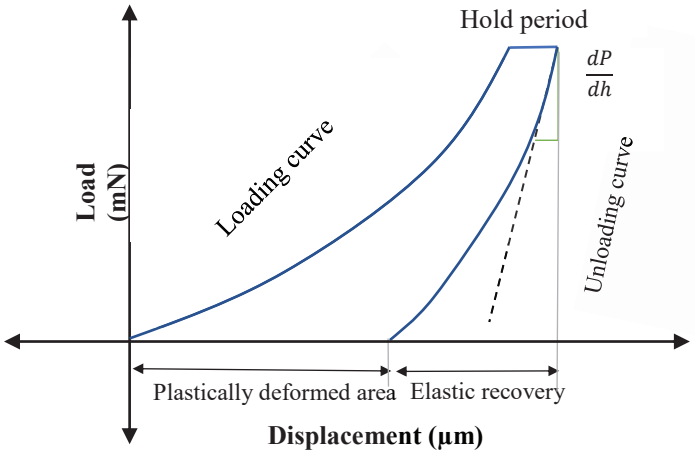

(a)

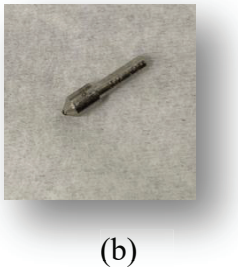

(b)

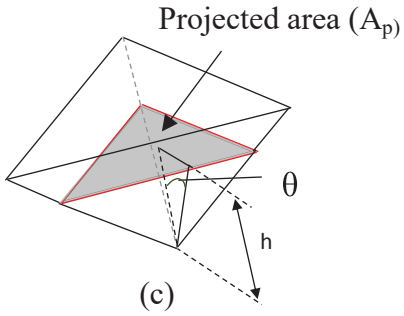

(c)

Figure 2-11 (a) Load vs depth plot obtained during nanoindentation using Berkovich indenter, (b) actual Berkovich indenter, and (c) schematic diagram of projected area by Berkovich indenter

Fig. 2-11 (b) shows the typical Berkovich indenter used for hardness testing. The grey area in Fig. 2-11 (c) shows the projected area (A_p) produced by the indenter at maximum load.

The equation for the projected area is defined as [2.1], [2.2]:

$$A_p = 3\sqrt{3} * h^2 * (tan\theta)^2 \tag{2.1}$$

The ‘h’ is the penetration depth at maximum load and the angle ‘***P***’ is the indenter angle. The indenter used for this research had θ = 65.27°. When substituted in the equation,

$$A_p = 24.56(h)^2 \tag{2.2}$$

Thus, the hardness can be expressed as:

$$H = \frac{P\ (\max load\ applied)}{A} \tag{2.3}$$

As the Ni-Mn-Ga alloy is a viscoelastic material, the elastic recovery of the material was of a substantial amount and thus there were several measures taken while conducting the hardness test. In elastic materials, where the recovery rate of the material is high, material pushes the indenter in the backward direction and would try to regain its original shape. In this action of the material, the phenomenon of pilling up around the indent occurs which creates error as well the hardness of the material would be noted low, which is not true. This hardness is known as ‘Indentation hardness’ and is found comparatively low as compared to the actual material hardness.

There are several ways to overcome this error, out of which one is using the holding period, or creep timing. It is basically putting a small hold period at the maximum load which would show the pseudo-elastic behavior of the material as well as reveals the actual plastically deformed area. [34] One more measure taken to check whether the hardness calculated is the accurate hardness of material was done by conducting several numbers of tests with the creep timing in different parts of the sample and statically checking the average values and standard deviation in the results. Fig. 2-12 depicts the image of pile-up phenomenon that occurred while conducting nanoindentation. Fig. 2-12 (b) shows the actual picture of pile up material on one the edges of indent impression.

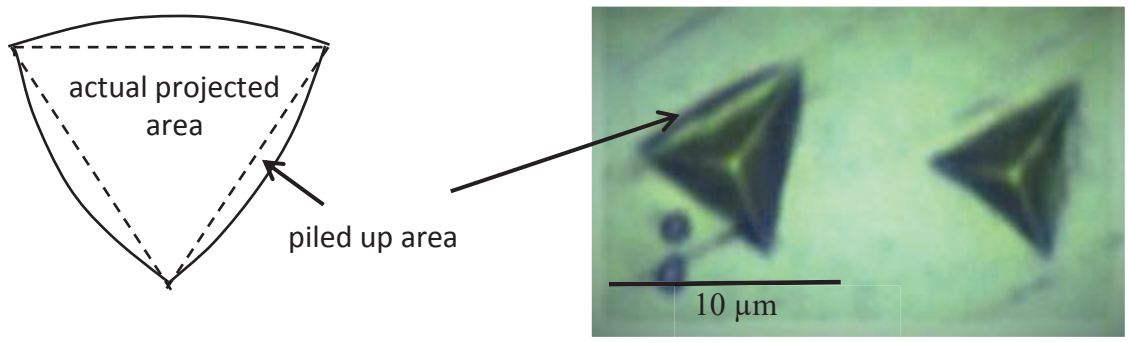

(a) (b)

Figure 2-12 Piling up phenomenon (a) Piling up around projected area (b) Piled up material around the indent in martensitic sample

2.4.2 Modulus of Elasticity (E)

The unloading curve is related to the elastic behavior of the material. The slope of the unloading curve shown in Fig. 2-11 (a) gives the value of the elastic modulus of the material. The expression for elastic modulus can be given by [33], [34]:

$$Elastic\ modulus\ (E) = \frac{dP(change\ in\ load)}{dh(change\ in\ depth)} \tag{2.4}$$

The modulus measured in this way is formally called the "indentation modulus" (E_{IT}) of the specimen material. Ideally, the indentation modulus has precisely the same meaning as the term "elastic modulus" or "Young's modulus" but this is not the case for some materials. The value of indentation modulus may be affected greatly by material behavior (e.g. piling-up) that is not accounted for in the analysis of load-displacement data. For this reason, care must be taken when comparing the modulus for materials generated by different testing techniques and on different types of specimens. [34] Variations on the basic load-unload cycle includes partial unloading during each loading increment,

superimposing an oscillatory motion on the loading, and holding the load steady at a maximum load and recording changes in depth. These types of tests allow the measurement of viscoelastic properties of the specimen material.

2.4.3 Yield Strength (σ)

For calculating the yield strength of the material, it is very important to define the inflection point or yield point at which the plastic deformation of the material started. And to define this, the transition of the elastic-plastic deformation must be smooth which is very difficult to obtain using a sharp indenter such as a Berkovich indenter. Therefore, the yield strength test is done using a flat tip indenter, which has basically a flat diamond tip with a circular radius of 20-30μm, shown in Fig. 2-13.

Figure 2-13 Flat tip indenter

The yield strength evaluation through indentation method is based on strain hardening principle. [35], [36] Similar kind of nanoindentation tests were conducted to obtain the load versus depth data, by using the flat indenter, shown in Fig 2-13. The load versus depth data was then analyzed to obtain the yield strength of the material. A MATLAB code was developed which would help pinpoint a location on the curve from where there was a sudden increase in the slope of loading curve.

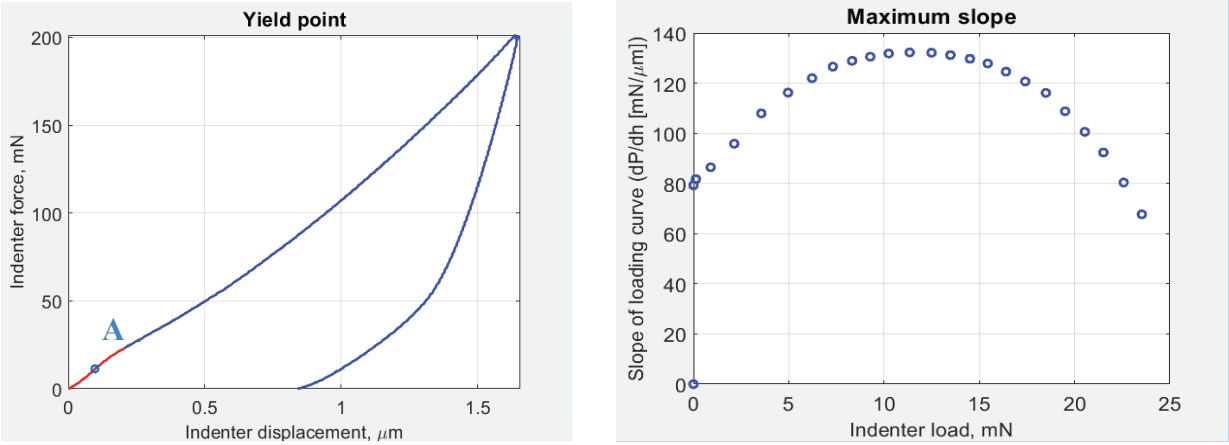

(a) (b)

Figure 2-14 Plots used for calculating yield strength (a) plot for determining the yield point A- inflection, (b) plot for finding load at maximum slope

That point is the yield point, defining the starting point of plastic deformation, shown in Fig 2-14 (a) as point 'A'. The second graph is also plotted in MATLAB for slope versus load, Figure 2-14 (b). This graph helps define the load at the maximum slope. Once the load value is defined, the values can be substituted in yield strength equation to obtain the value of yield strength of the material.

The phenomenon of strain hardening is the base for calculating the yield strength using the nanoindentation technique. [34] As the indenter first starts indenting it generates an elastically deformed area around the indenter and beneath the surface of the material. The elastically deformed area is found to produce a half penny like shape beneath the surface, which further pushes the next layer of material. Once the elastic limit of the material is reached, the deformation of the material starts plastically and at a faster rate for the amount of load applied. This transition helps define that the plastically deformed area has started producing around the contact point of indenter with the surface. The point on loading curve is thus defined as the yield point of the material, and the load

at that point is used for calculating the yield strength of the material. The yield strength is also calculated by the nanoindentation module, but it is more accurate by calculating it analytically using MATLAB.

2.5 Microhardness testing

The evaluation of the fracture toughness of material could be done with respect to different loading conditions such as tensile or in-plane shear loading. Particularly, failure in tensile loading (Mode I loading) is more prominent among other loading conditions, as most brittle materials fail in Mode I. It is due to this reason that Mode I loading is taken into consideration for this study. [37] In this research microhardness technique was used for the determination of fracture toughness of material at the micro level. It is because the technique is particularly useful for brittle material with low fracture toughness. It is also very simple, rapid and permits small sample size for testing purpose. [38] Microhardness test can probe a surface and map its properties on a spatially resolved basis, sometimes even with a high resolution of 1 μm. [39] There are many theories and models available which when related to the experimental outcome, helps in defining the mechanical properties such as hardness (H) and elastic modulus (E). But, particularly for this research work, microhardness tester was used to nucleate a crack in the sample and understand one of the most important mechanical property of the material which is fracture toughness (K_{IC}). Microton Hardness tester shown in Fig. 2-15 was used for fracture toughness evaluation in this research. The difficulties and assumptions to be considered while conducting the fracture toughness test on different kinds of samples shall be discussed in the next few sections.

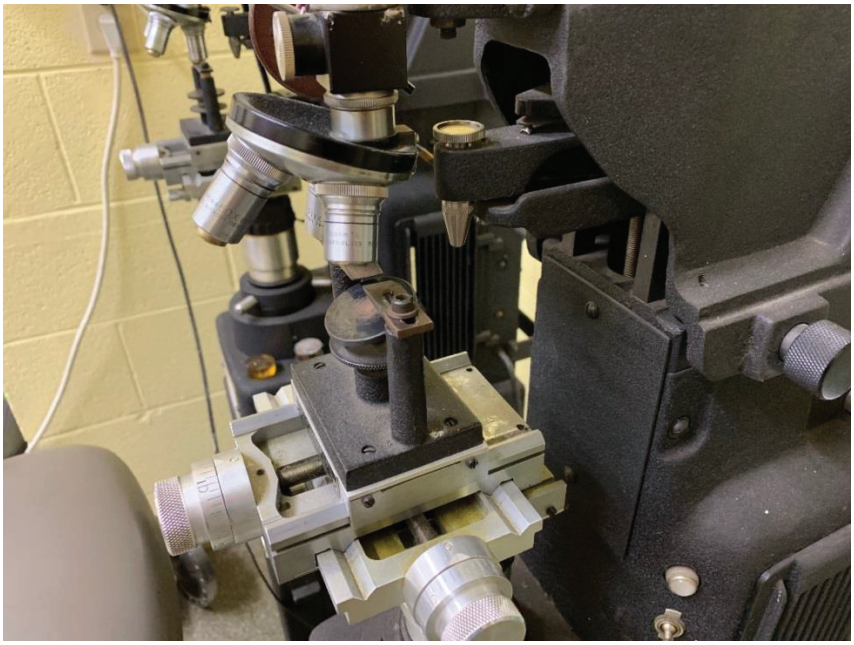

Figure 2-15 Microton microhardness tester used in this research and available at Materials Research Laboratory (MRL), Struthers, Ohio

2.5.1 Fracture toughness measuring technique for Ni-Mn-Ga bulk samples

A question may arise that, why was nanoindentation technique not used for conducting fracture toughness tests? The answer to that would be the maximum load limit on the nanoindentation machine. Particularly, if we consider the M1 Hardness tester from Nanovea (Fig 2-10) which was used for conducting other mechanical tests, the maximum load that could be imposed or applied using that machine was 400 mN. At this load, it was found that indent could be created on the surface, which was surrounded by the stressed area. It was also observed that due to access load on the austenitic phase sample, the area around the indent had stress-induced martensitic twins. However, no signs of cracking in the material were noted at maximum load. Due to this limitation, fracture toughness investigation had to be carried out using microhardness tester which helps in conducting test till maximum load of 100 N. Further, the indenter used for this

test was also different, Vickers indenter instead of Berkovich indenter (three-sided pyramidal). There are few reasons for it: (1) availability of only Vickers indenter for micro-hardness testing, (2) theoretical models available for interpretation of experimental results were found more accurate for Vickers indenter, and (3) simplicity in the correlation of data. These were important aspects which were considered for deciding the indenter tip for experimental purpose.

2.5.2 Fracture toughness measuring technique for 3D printed samples

The 3D printed samples are more porous, and fragile when compared to the bulk material. Tests were initially conducted on these samples using nanoindentation technique. While there were few cracks nucleated from the edges of the triangular tips, the determination of maximum load needed, and the connecting parameters was very difficult. It was because, although the max load and loading/unloading parameters were unchanged, the cracks nucleation was not uniform. Sometimes the sample cracked locally while sometimes it would only produce the indent with stress area around it. In this situation, the consideration of a fixed load at which the sample would crack every time was not possible. Thus, the samples were tested using the microhardness tester. As discussed before, the three samples with the same chemical composition were sintered at 1353 K for different time periods, 24 hrs., 40 hrs. and 50 hrs. The issue with the 3D printed sample is its high porosity. For conducting indentation on any sample, one of the important factors is a flat surface with no surface features such as pits, scratches or large pores. Due to this reason, it was difficult to find an area having at least a flat surface of twice the radius of an indent. Further, with increasing the sintering time, the porosity was

found to be decreasing. Thus, in the process of preparing the samples, the sintering time was increased gradually to increase the density of the material. One more thing which has to be taken care of is the shape memory effect of the material. The porosity in the material is very important for maintaining the shape memory effect of the material. [30] If the part would be over sintered the porosity of material would reduce, and it might affect the functional property of the material. Also, by sintering the samples at different time period, would help in comparing the effect of the manufacturing process on mechanical properties. This would certainly help in understanding the effect of density on the mechanical strength of the material. Certainly, comparing the fracture toughness of samples sintered for different time period help in understanding the mechanical behavior of the material.

2.5.3 Fracture toughness (K_{IC}) evaluation methods

Fracture toughness for the material is defined as the resistance of the material to rapid crack propagation and is characterized as one parameter (K_{IC}). [39] There are many efforts to minimize the errors in various fracture toughness models. But, one has to take into consideration several external factors which may affect the results such as material handling procedure, processing flaws or finishing flaws which would directly affect the crack size. [37] Investigations are also classified on the basis of sizes of crack. Two main aspects of fracture toughness are (1) initiation- the origin of the crack and (2) propagation- the path at which the crack propagates and measurement of the crack size. Investigation on crack nucleation and propagation from surface flaws and deformities has also been studied in various researches. One of the models for crack initiation beneath sharp indenter was proposed for understanding the microfractures in material, using an

approximation for tensile stress distribution in elastic/plastic indentation field. It discussed the functional relationship between the size of a critical flaw to the load required for inciting a crack from it. [40] The study helped to understand the relation of the load to the initial crack nucleation and gave a profound understanding regarding the allowable flows in the material which would not affect the results.

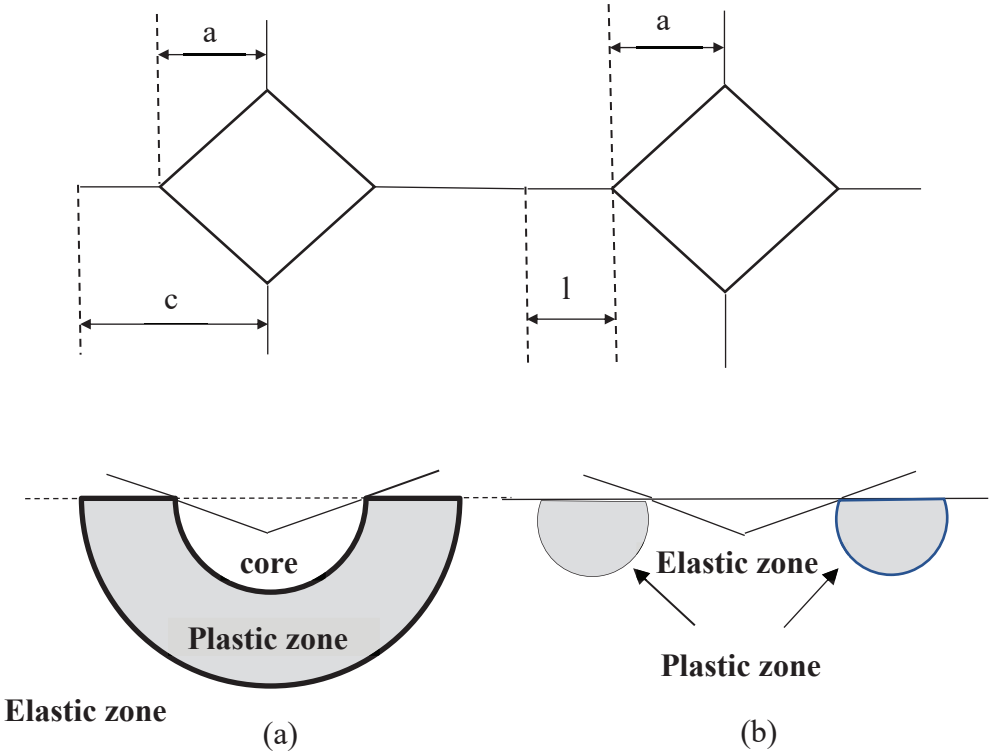

Figure 2-16 Fracture toughness models for Vickers indenter (a) Radial crack propagation, (b) Palmqvist crack propagation from Vickers indenter. 'a' is average diagonal length, 'c' is radial crack length and 'l' is Palmqvist crack length

Fracture analysis models have also been classified on the basis of different types of cracks, namely: (1) radial cracks and (2) Palmqvist crack. For the micro-fracture phenomenon in materials, a number of studies suggested that brittle material tends to fracture forming a Palmqvist crack. On further increase in load, the cracks radially extend along median planes of the indentation and remain close to the specimen surface. During

the unloading process, the crack grows deeper and propagates further through the material. These eventually form, half-penny shape as shown in Fig. 2-16. [41] Several models were used to evaluate fracture toughness of the material, which was governed by the crack type, length of these cracks, and value of hardness (H) and elastic modulus (E) of the material.

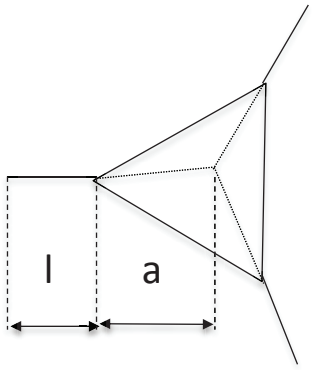

Figure 2-17 Fracture toughness evaluation from Palmqvist model based on Berkovich indenter

Models considered in this study were differentiated on the basis of the type of indenter, and type of crack.

Vickers indenter models: (1) radial crack length models - Anstis model, Laugier's model, and Niihara's model and (2) Palmqvist crack length models – Laugier's model and Niihara's model.

Berkovich indenter model: Laugier's model

I. ***Anstis model for fracture toughness evaluation:*** This model is based on radial crack length. [42] This model considers crack length measurement from the center of the indent to the end of the longest crack. Fig. 2-16 (a) shows the radial crack of length 'c', emerged from an indent impression by Vickers indenter. It is

important to notice here that, Fig. 2-16 (a) shown above depicts the ideal cracking phenomenon, but in reality, some discrepancy is observed in crack propagation. The most widely used expression for radial cracks was proposed by Anstis model as [42]:

$$K_{IC} = A * \left(\frac{E}{H}\right)^{1/2} * \left[\frac{P}{c^{\frac{3}{2}}}\right] \tag{2.5}$$

In equation (2.5), the A is an empirical constant defined by Anstis, and P is defined as indentation load. Also, H and E are hardness and elastic modulus of material respectively.

II. **Laugier's models for fracture toughness evaluation:** The models by Laugier are based on both types of cracks, namely radial and Palmqvist crack. Also, the models are based on both kinds of indenters that are Berkovich and Vickers indenter. Fig. 2-16 (a) and (b) shows the schematic diagram for the Vickers indenter model, of how the crack propagation occurs through the vertices of indent. The expression developed by Laugier for radial and Palmqvist crack is almost identical with a minor change in fitting constant. The general equation is showed as [40], [42]

$$K_{IC} = X_v * \left(\frac{a}{l}\right)^{\frac{1}{2}} * \left(\frac{E}{H}\right)^{\frac{2}{3}} * \left(\frac{P}{c^{\frac{3}{2}}}\right) \tag{2.6}$$

X_v in equation (2.6) has a value of 0.015 for Palmqvist model based on Vickers indenter and 0.016 for Berkovich indenter. 'l' is the Palmqvist crack length as shown in Fig. 2-16 (b) and 2-17. These were the two models widely used for determining the fracture toughness of brittle materials, and there are still different

studies going on to make the equations more generalized and understand the fracture toughness phenomenon deeply.

Laugier's radial crack length model based on Vickers indenter is defined as shown in equation (2.7) below, where the crack ratio is not used as seen in Palmqvist crack model. Further, X_v value used for this model is 0.01. [40], [42]

$$K_{IC} = X_v * \left(\frac{E}{H}\right)^{\frac{2}{3}} * \left(\frac{P}{c^{\frac{3}{2}}}\right) \tag{2.7}$$

III. **Niihara's model for fracture toughness evaluation:** The model is found to be only based on radial cracks. [41] The expression used for radial cracks length is shown by (2.8), where the A is determined as 0.0309.

$$K_{IC} = A * \left(\frac{E}{H}\right)^{1/2} * \left[\frac{P}{c^{\frac{3}{2}}}\right] \tag{2.8}$$

All the crack models discussed above were to investigate the fracture toughness value of all the three types of samples, (1) austenite (bulk), (2) martensite (bulk) and (3) 3D printed samples.

2.6 Light microscopy

The etched samples were brought under the light microscope to confirm the phases of the samples visually.

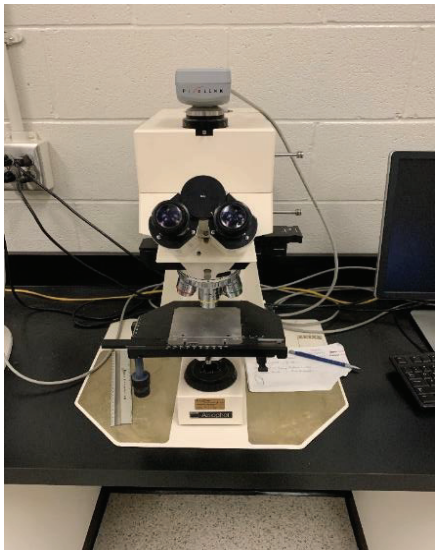

Figure 2-18 ZEISS Axiphot - Pixelink camera

To conduct this test the ZEISS Axiphot microscope equipped with Pixelink high-resolution camera was used. Fig 2-18 shows the microscope used for obtaining optical micrographs. To obtain a DIC image of the samples, LECO 300 Metallograph machine was used.

2.7 Differential scanning calorimetry (DSC)

Differential scanning calorimetry is a measuring method used in different research areas, to obtain accurate values of heat capacity, the heat of transition, kinetic data and glass transition. Thermal effects over a large range of temperature, for substance quantities in milligram range, can be quickly identified. One of the important results is the DSC curve which helps in identifying substance phase change, and degrees of crystallinity. [43] The technique is used in this research work, to determine the phase change temperature of the Ni-Mn-Ga alloy. There are two main phases of the alloy namely: (1) parent phase (austenitic phase) and (2) martensitic phase. In this study, there

were two ingots prepared with such a chemical composition that, one of them would be in the austenitic phase at room temperature while the other would be in the martensitic phase at room temperature. The objective of calorimetry is to measure the heat exchange with respect to time, as the change in heat exchange is directly affected by the temperature of the material. The process of heat exchange creates a heat flow which leads to change in local temperature along its path which again would help in determining the heat flow. Many physical and chemical transitions are connected with the consumption or generation of heat in the material. So, the phase change of material is determined with respect to the change in heat flow. [43] In an actual test, different values for the test sample are calculated with respect to the reference sample, for which all the parameters for different amount are pre-determined. An accurate definition for differential scanning calorimetry is given by G. W. H. Hohne as: "Differential Scanning Calorimetry (DSC) means the measurement of the change of the difference in the heat flow rate to the sample and to the reference sample while they are subjected to a controlled temperature program." [43]

DSC measures change in heat flow rate difference, which is normally due to alterations of sample temperature. If there is zero value for difference in heat flow rate, it means that the samples have the same heat flow rate and are at the same temperature. On the other hand, a non-zero heat flow rate difference implies the temperature difference between the samples or their surroundings, and a change of heat flow rate difference implies a change of the temperature as well. There are two basic modes of differential scanning calorimetry, (1) heat flux DSC and (2) power compensation DSC. We shall only discuss heat flux DSC as it was used in this research and brief information regarding

every method can be obtained elsewhere.[43] Heat flux DSCs are heat-exchanging calorimeters, where the exchange of heat is measured with the surroundings with the help of a well-defined heat conduction path with given thermal resistance. The temperature difference is the primary signal for measuring the intensity of the exchange and the resulting heat flow rate (ϕ) proportional to it. [43] Again there is a sub-classification among the design of measuring system, (1) disk-type measuring system, (2) turret-type measuring system, and (3) cylindrical type measuring system. We shall only discuss the disk type measuring system as it is relatable to the test system, but brief knowledge about all the system could be found elsewhere. [43] Fig. 2-19 is the schematic curve which is obtained as a result of the experiment. As the test starts, the furnace heats the sample with the help of heat flow through disks. It is assumed that the heat flow is the same for the test sample and the reference sample. Now, as the test precedes differential temperature signal (ΔT) in the form of electric potential difference is transmitted to the receptors and is then zero. If this steady state equilibrium is disturbed by a sample transition, a differential signal is generated proportional to the difference between the heat flow rates to the sample and to the reference sample. [43]

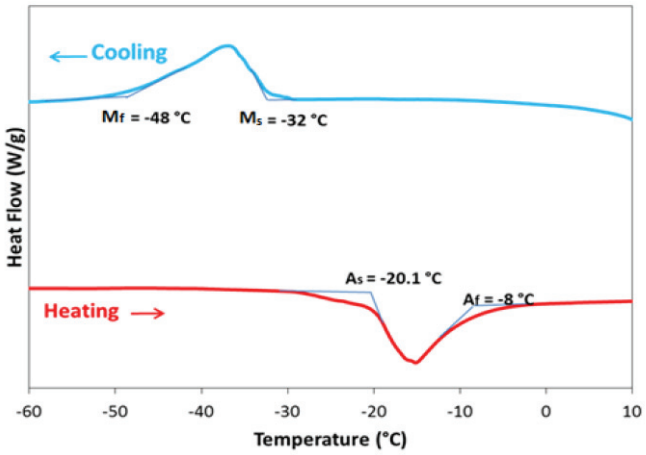

Figure 2-19 Typical DSC plot

Analytically presented as:

$$\phi(FS) - \phi(FR) \sim \Delta T \quad \text{where, } \Delta T = T_S - T_R \tag{2.9}$$

An important point to be noted here is measurement signal is always recorded or received by the system in the form of an electric voltage. In the software, the heat flow rate ϕ_m measured is internally assigned to signal ΔT by factory installed provisional calibration. Detail instructions for calibration of the machine are explained elsewhere. [43] The curve in Fig. 2-19 depicts the phase transition in material, as we could see a bump in the heat flow through the material. It confirms that phase transformation took place and it can confirm in which phase the material is. Heat flux DSCs with disk type measuring systems have generally a working temperature range between 83 K and 1873 K, with a maximum heating rate of 100 $Kmin^{-1}$. The typical time constant of the empty system or system without the test sample is between 3 and 10 seconds. Depending on the working temperature and heating rate, the noise disturbance of the measurement signal lies between 0.5 μW to 20 μW.The total error or uncertainty in the measurement of heat amounts to around 5% and it is expected that least it could be reduced to is 2%. [43]

2.7.1 DSC equipment used for the experiments

There were two different differential scanning calorimeters used for conducting the test: (1) Universal V2.6D TA instruments and (2) Diamond DSC - Perkin Elmer. The Universal V2.6D TA instrument was used for austenitic phase sample. It was because the chemical composition of the ingot was chosen in such a way that the phase transformation temperature of the austenitic phase sample was at very low temperature (93 K). The temperature range of Universal instrument is from 93 K to 973 K.

(a) (b)

Figure 2-20 Diamond DSC - Perkin Elmer: (a) Whole unit, (b) Detail view

Liquid nitrogen was used to acquire such a low temperature while the cooling cycle. Diamond DSC – Perkin Elmer was used for the pure martensitic phase sample. The phase transformation of the martensitic phase sample was at high temperature (over 473 K) for the heating cycle.

Fig. 2-20 shows the DSC machine used for martensitic phase sample. Fig. 2-21 shows the aluminum crucible (pan-kit) in which the sample is sealed and then kept into the instrument for conducting the test.

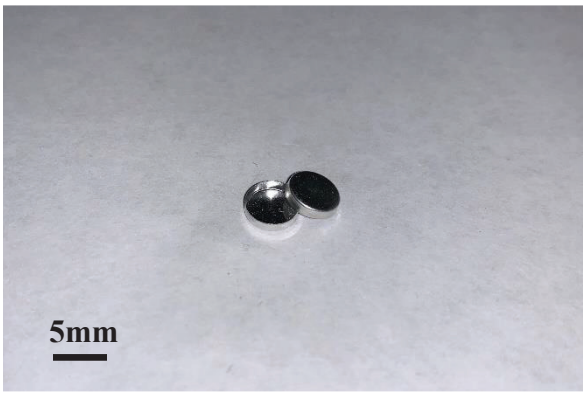

Figure 2-21 Pan-kit

2.8 Scanning electron microscopy

After the sample surface and the indents from the microindentation testing were analyzed using the light microscopy, the further analysis of results was done using a scanning electron microscope. Fig. 2-22 shows the comparison between the image contrast obtained while using different detectors namely: (a) Secondary electron (SE) detector and (b) backscattered electron detector (BSE). It is important to note that, the image from the BSE detector showed black color for surface deformities like pores and cracks which was very useful in determining the cracks, as shown in Fig. 2-22 (b)

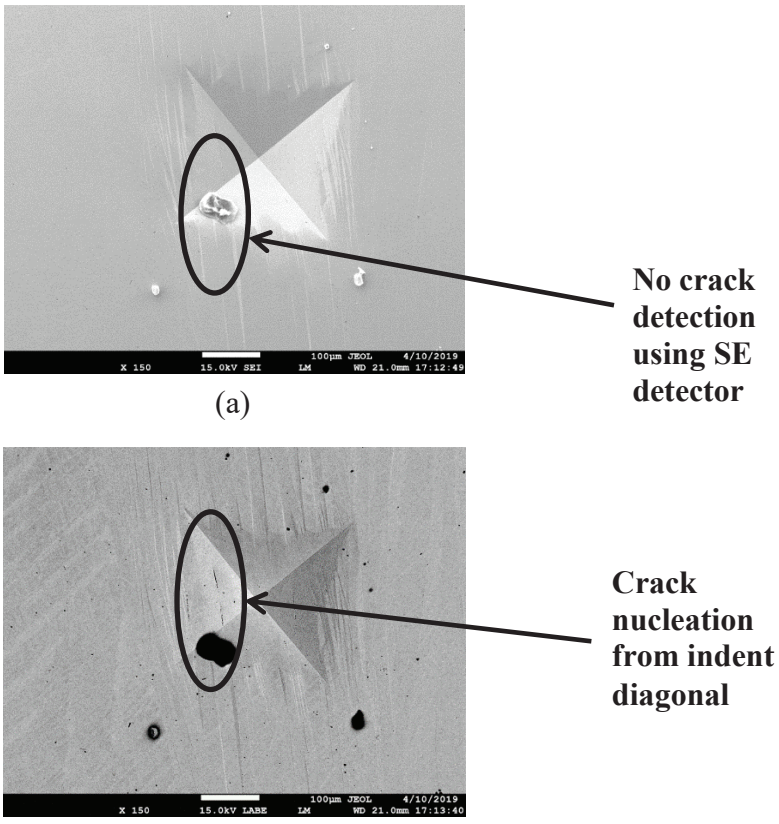

Figure 2-22 Micrographs of martensitic sample, (a) SE micrograph and (b) BSE micrograph

The SE image showed in Fig. 2-22 (a), helps in confirming that the black spot in the image is not a surface deformity, while it is some external contamination from the paper wipes sitting on the surface. In conclusion, both the detectors were used to confirm the actual deformity and contamination on the surface to attain high accuracy in results.

2.9 Numerical modeling

The reason for conducting the numerical modeling is to investigate the strain in material under the indenter tip, with respect to indenter displacement in the material. It is important to understand that, the motivation of numerical modeling is to confirm the half-penny assumption made previously while using the radial crack models.

Model of the nanoindentation testing setup for two-dimensional analysis was done on DELL OPTIPLEX 7010 four core processor computer using SolidWorks 2017. The geometry of the model from SolidWorks is shown in Fig. 2-23, with respective dimensions. It is important to note here, that the model is scaled to inches, as the effect by the indenter is assumed to be same with equivalent loading conditions for nano- and micro and macro- scale investigation. The indenter angle with the surface is used as 24.7 degrees which make the face angle of indenter as 65.27 degrees, depicting the Berkovich indenter.

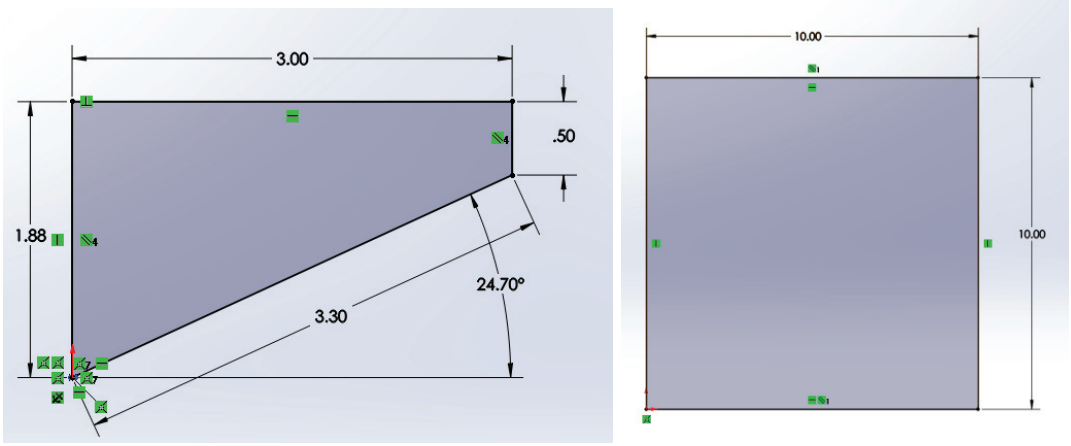

(a) (b)

Figure 2-23 Indentation model, (a) indenter geometry and (b) part geometry (All dimensions are in inches)

In the actual indentation test, the material to be indented that is Ni-Mn-Ga alloy which is softer than the indenter material, diamond. Similarly, while modeling the nanoindentation test numerically, the material used for indentation was taken as steel and material to be indented was aluminum. Initially, while conducting the tests with a sharp indenter, the point of contact was a single point, experiencing very high stress known as singularity error. [44] To overcome this error a small radius was given at the tip of the indenter as shown in Fig. 2-24 (b).

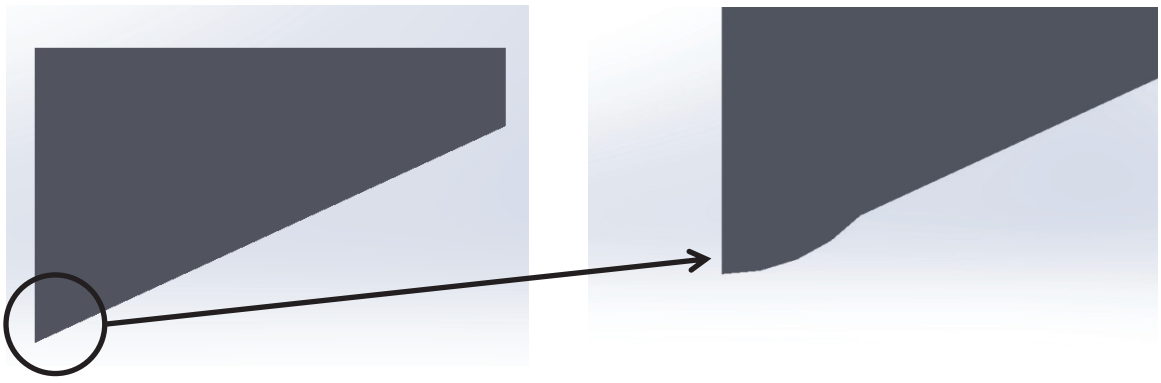

(a) (b)

Figure 2-24 Indenter geometry, (a) profile view and (b) detail picture of tip radius

This makes edge contacts, rather than a single point contact, dissipating the excess stress. It is important to note here that, in actual condition as well, due to continuous use of the indenter for several years, makes the tip somewhat blunt with a really small radius at the tip. This confirms the finite element analysis model would not be affected with the tip radius given to the indenter. Further, the SolidWorks geometry was assembled and was imported in ANSYS 19.1 modeling software. Design modeler was used for modeling the part file from SolidWorks, as 2D plane geometry.

2.9.1 Modeling parameters

As determined before, the indenter was given properties of steel, while the material block was defined as aluminum. A new coordinate system was defined at the contact of the two surfaces, for defining different meshing operations with respect to the new coordinate system. Fig. 2-25 depicts the image of the new coordinate system used in the model.

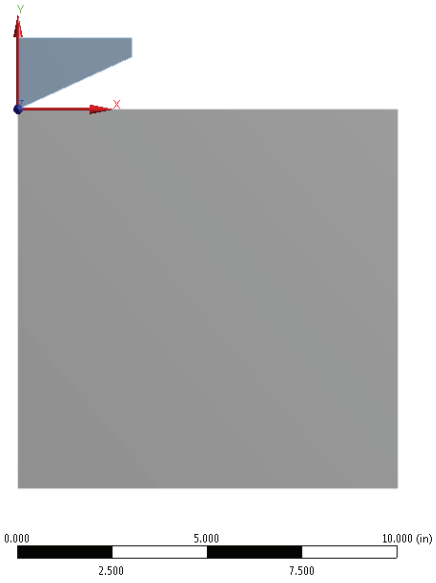

Figure 2-25 Co-ordinate system used in the model

Further, the contact between the two parts was defined as frictionless contact, bonded with each other. For the contacts, the target edge was selected as the indenter edge while the contact surface was selected as the aluminum part edge. Here, the formulation of the model can be used as program controlled as well as the pure penalty for this analysis.

2.9.2 Meshing

For meshing six different operations were used. Three each for indenter and part, respectively. All triangles method was used for meshing both the parts, as it was found to be more convenient in producing denser mesh for the contact region. Further body sizing operation for overall mesh was used to make the mesh elements finer. Overall mesh size for both the bodies was used as 0.1 in, which has a size of the hundredth part of the material block. Although most of the part would hardly affect the simulation result, the mesh size was chosen fine to take precautionary measures.

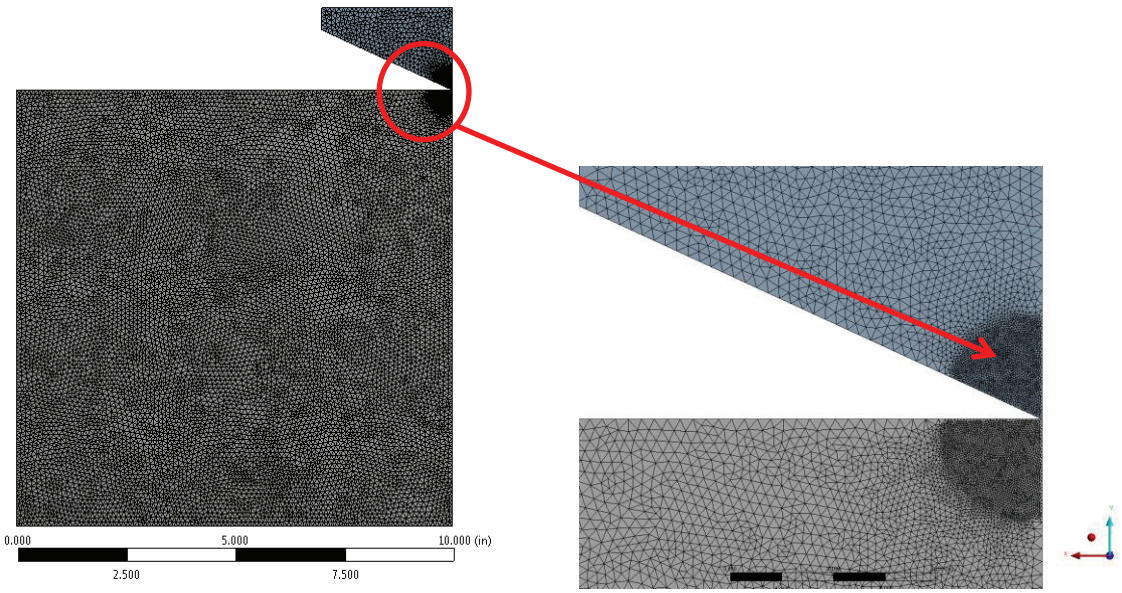

(a) (b)

Figure 2-26 Mesh details, (a) profile view, (b) detail view of mesh for the contact region

As shown in Fig. 2-26 the mesh for the contact region was made denser using sizing operation governed by a sphere of influence method. This helps in making the mesh denser only in the area of the sphere of influence. Two spheres of influence with radius 0.5 in and 0.1 in were used, to make the mesh transition smoother while progressing towards the contact area. The mesh size for a sphere with radius 0.5 in was taken as 0.01 inch while the mesh size for a sphere with a radius of 0.1 inches was 0.002 inch. The end results as shown in Fig. 2-26 were not the best but were still appropriate for the goal of the simulation.

Chapter 3 Results and discussion

3.1 Thermal analysis using Differential Scanning Calorimetry (DSC)

Ni-Mn-Ga alloy possesses two phases, a parent phase (austenitic phase) with the cubic crystal structure, while the second with non-cubic (tetrahedral, monoclinic, orthorhombic, etc.) crystal structure known as a martensitic phase. The phase transformation from austenitic to martensitic phase is due to shifting of atoms at crystallographic level, can be caused due to temperature change, magnetic field, or external loading. The shift of atoms produces twin defects, known as martensitic twins. In this research, there were three different types of samples prepared namely, austenitic martensitic and 3D printed sample. So, to confirm the actual phase of different samples at room temperature DSC analysis was carried out. Differential scanning calorimetry (DSC) is a thermal analysis to note the exchange of energy between the test sample and reference sample in the form of heat. [43] The core reason for conducting the DSC test on Ni-Mn-Ga samples was to define the phase change temperature of the sample from austenite to martensite phase and vice-versa. This would help in defining the phases of material at room temperature (298 K).

3.1.1 Austenitic sample

Fig. 3-1 shows the heating and cooling curves obtained from the bulk Ni-Mn-Ga alloy sample suspected of having austenitic phase at room temperature (RT). The blue curve which is the cooling cycle shows the martensitic formation below M_s = 241 K. Here, the martensitic start temperature (M_s) is 241 K and martensitic finish temperature (M_f) is 225 K. This clarifies that the austenitic phase change to the martensitic phase on the cooling

cycle took place at a very low temperature, way below RT. Similarly, from the red curve which is from the heating cycle, shows the phase transformation from the martensitic to the austenitic phase. The austenitic start temperature (A_s) is at 253 K and austenitic finish temperature is 265 K.

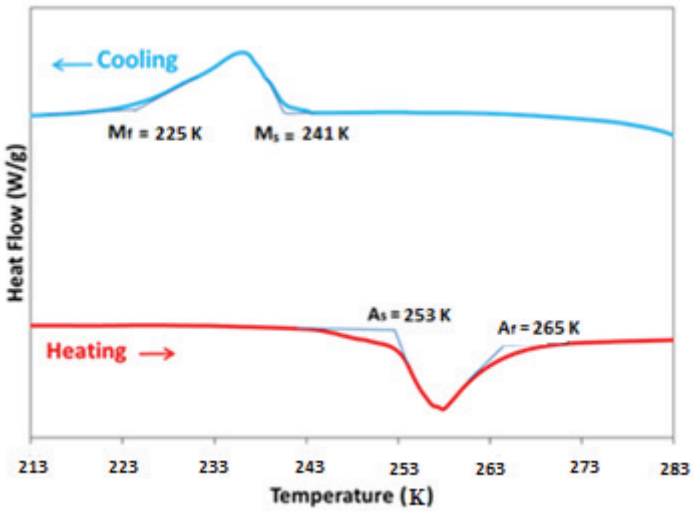

Figure 3-1 DSC result for austenitic sample

This confirms that the sample was in the austenitic phase for any temperature above 265 K. Thus, it can be concluded that the sample was in the austenitic phase at room temperature.

3.1.2 Martensitic sample

Fig. 3-2 depicts a DSC plot for the martensitic sample. The cooling curve (blue) shows that the martensitic phase transformation took place at very high temperature. Martensitic start temperature is at 478 K and martensitic end temperature at 464 K. This confirms that for temperature below 464 K the sample would be in the martensitic phase.

Similarly, on the heating curve, the austenitic start temperature is at 489 K and austenitic finish temperature at 505 K.

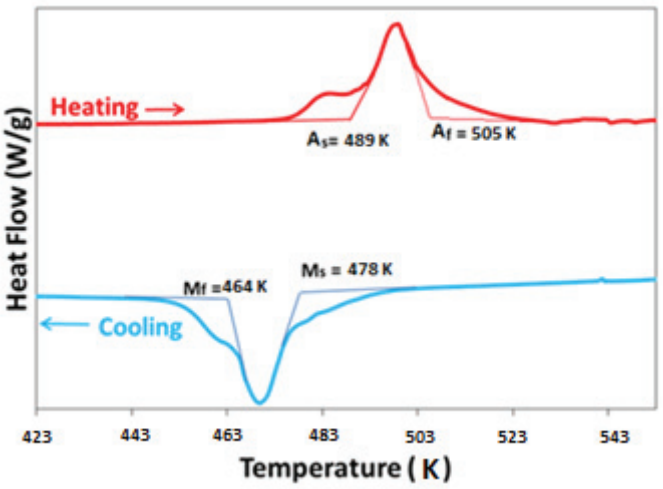

Figure 3-2 DSC result for martensitic phase sample

Thus, in conclusion at room temperature, the sample was in the martensitic phase.

3.1.3 3D Printed sample

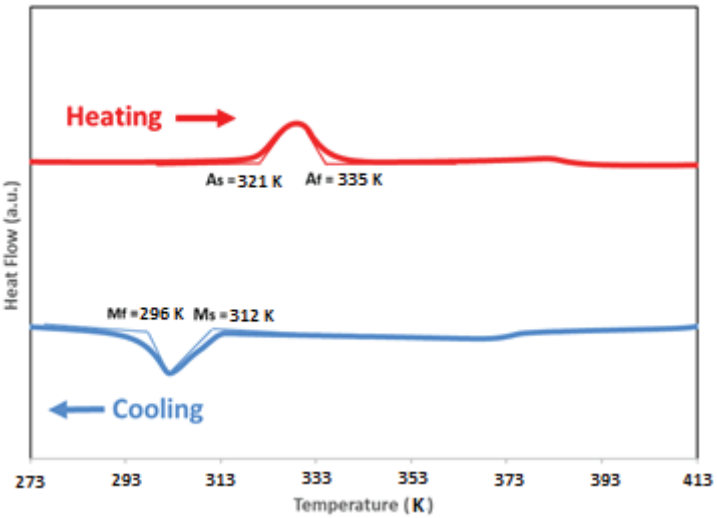

Figure 3-3 DSC result for 3D printed sample

Fig. 3-3 shows the DSC curve of 3D printed samples. It should be noted here that the phase transformation into the austenitic phase takes place between 321 K and 335 K temperature. Also, from the cooling cycle, the martensitic phase transformation takes place between 296 K and 312 K temperature. This determines that the 3D printed samples had both austenitic and martensitic phase at room temperature.

3.2 Light Microscopy

3.2.1 Electrochemically etched samples

Optical or light microscopy was initially used to analyze the polished surface of the samples. These micrographs were critical in defining pore sizes, surface flaws (scratches) and arteffects due to contamination, as shown in Fig. 3-5, before moving towards nanoindentation and microhardness testing.

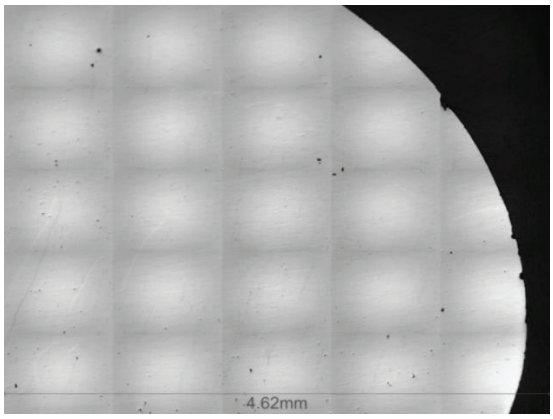

Figure 3-4 Austenitic phase sample after electrochemical etching

Figs. 3-4 and 3-5 are the micrographs for both austenitic and martensitic phase bulk sample after conducting the electrochemical etching process.

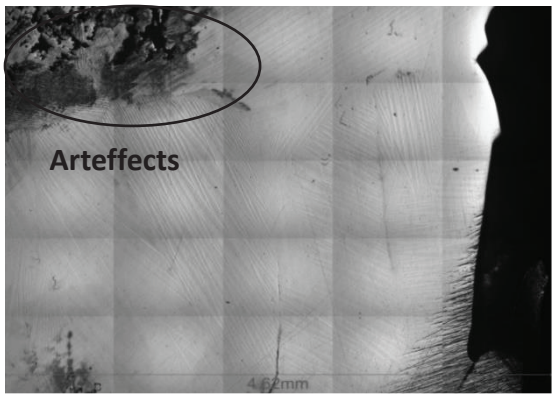

Figure 3-5 Martensitic phase sample after electrochemical etching

It clearly shows that the pit size is apparently reduced for both the samples and the surface looks ideal for conducting the nanoindentation and microhardness testing.

3.2.2 Nanoindents

It becomes very important to initially analyze the location of indent and its shape after the test is conducted. If the surface is not flat enough, the indentation test will have an error in defining the projected area at the max depth of indentation. This would result in calculation error and eventually, the hardness, elastic modulus, and yield strength data could not be validated according to International Standards. [45] So, the first step to validate the results was to analyze the indents under the light microscope. Figs. 3-6 and 3-7 are the light microscopy images of the martensitic and austenitic phase sample surface after conducting the indentation test. There are set of six and four indents done at equidistance in horizontal, as well as vertical direction on both the samples, respectively. It can be seen that the small triangular indent is depicting an equilateral triangle, confirming the indent was done on a flat surface. Also, no piling up or sinking occurred around the indent which determines that the tests were considerably accurate.

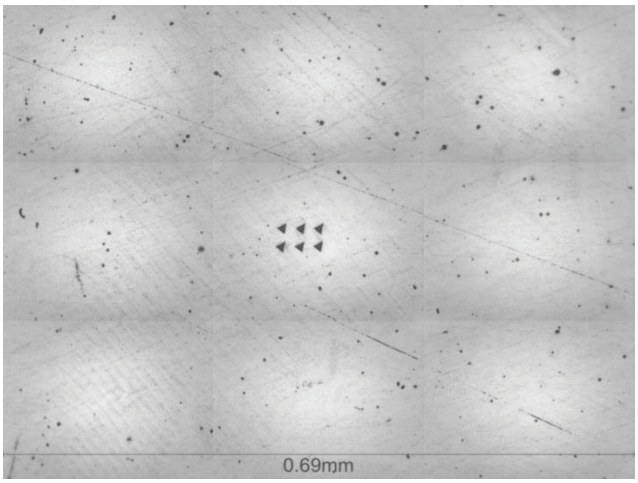

Figure 3-6 Nanoindents on martensitic sample

One more important aspect which was analyzed was to confirm the space between the two indents. A distance of three times the indentation radius has to be left in between two indents or any surface deformity. This is done to assure that the test is not affected by any stress field produced due to a previous indentation or material flaw. Secondly, the values from the first indent should be compared with results from the second indent to confirm the effect if there is any, due to the first indent. [45] Taking into consideration the guidelines, a distance of around 15 to 20 μm was left between two indents. Fig. 3-8 is the micrograph of nanoindentation testing done on 3D printed sample. A large number of pores made it difficult to choose a perfect spot for indentation on 3D printed samples. But, optical microscopy was useful in selecting proper indentation spot, as well as confirming the test results of nanoindentation.

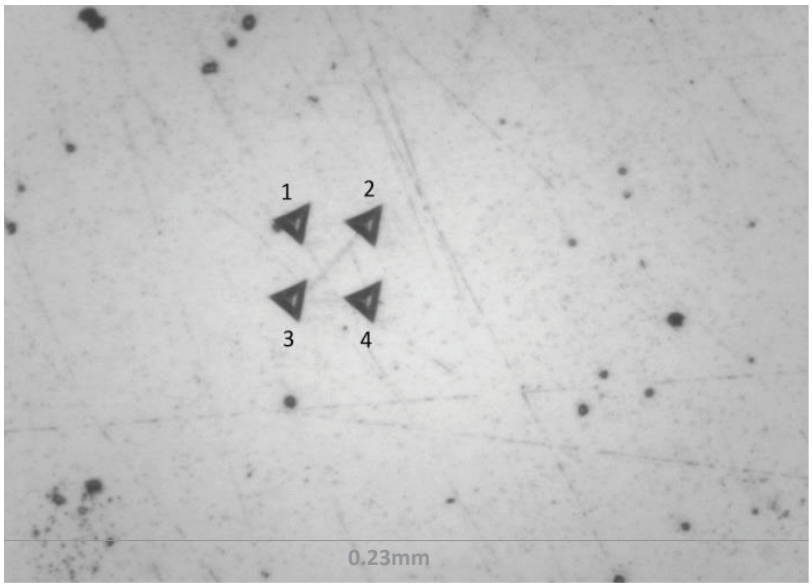

Figure 3-7 Nanoindents on austenitic sample

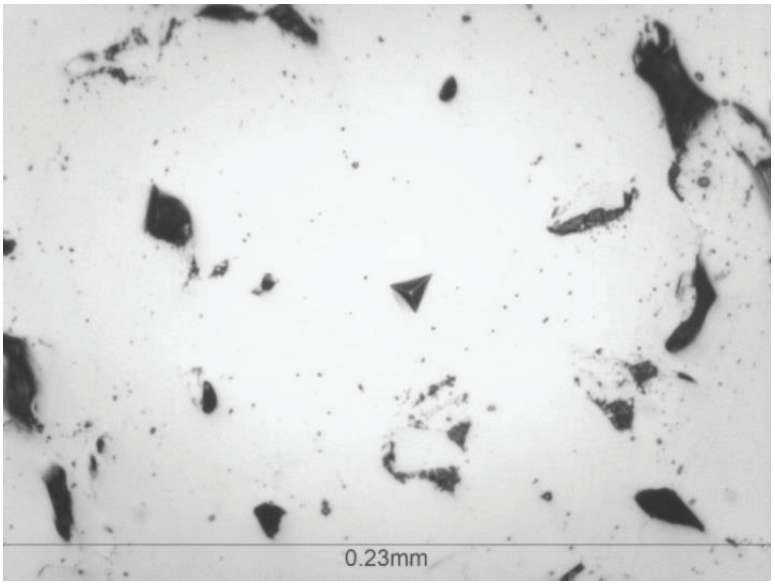

Figure 3-8 Nanoindent on 24 hrs. sintered 3D printed sample

3.2.3 Light microscopy for fracture toughness analysis

Light microscopy was very useful in initially defining the cracking load for different types of samples. It helped in understanding the phenomena of strain induced martensitic

transformation in austenitic Ni-Mn-Ga alloy which occurred while conducting fracture toughness tests.

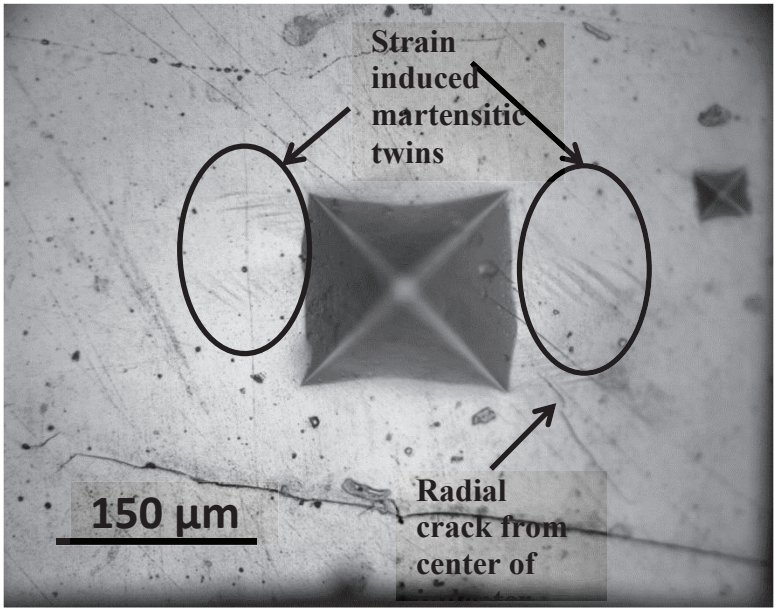

Figure 3-9 Microindent on austenitic phase sample

Fig. 3-9 shows the bright field image of microindent analyzed under an optical microscope. Twin variant could be seen orienting in different directions around the indent, which shows the phenomenon of phase transformation from the parent phase to the martensitic phase under an applied load. It also helps in confirming the crack nucleation in material, determining material failure under that particular amount of load. However, scanning electron microscope (SEM) was used to determine the crack length, but optical microscopy helped in assuring the material actually cracked.

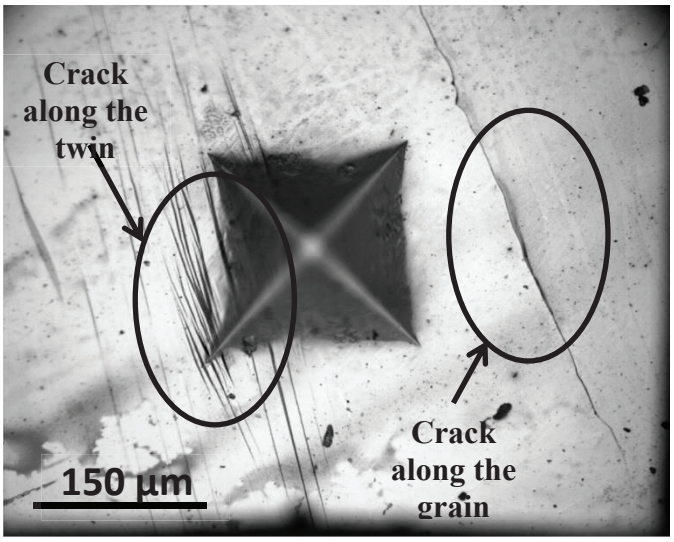

Figure 3-10 Fracture toughness testing on the martensitic phase sample

Different samples, such as the martensitic sample, and 3D printed samples were first analyzed under an optical microscope to determine the location of indent as well as crack nucleation in the material. Light microscopy image of microindentation testing on martensitic phase sample could be seen in Fig. 3-10.

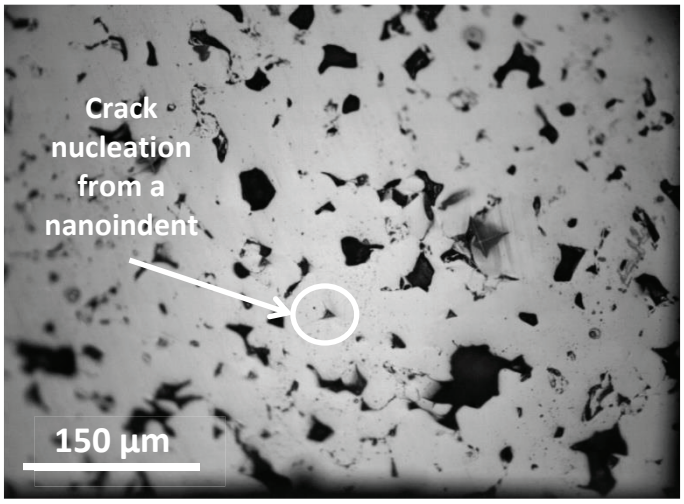

Figure 3-11 Fracture toughness testing using nanoindentation instrument on a 24 hrs. sintered 3D printed sample

Here, the optical micrographs helped in confirming the crack propagation along the twin boundaries in martensitic phase samples. A crack was also observed away from the indent, perhaps along a grain boundary. This behavior was observed for several microindents, indicating fracture toughness of the grain boundaries in the martensitic sample.

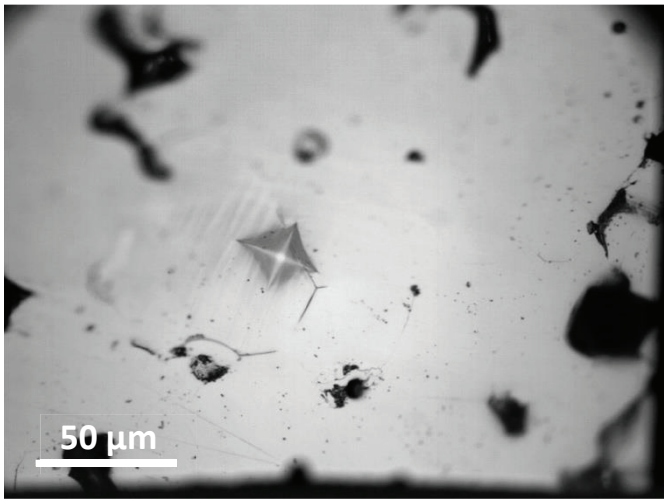

Figure 3-12 Microindentation testing on a 40 hrs. sintered 3D printed samples

Additively manufactured samples had pits and flaws throughout the surface of the material which could be seen in Figs. 3-11 and 3-12. In this case, optical microscopy helped in selecting the perfectly flat surface, for conducting the fracture toughness testing. Also, to determine the validity of the indent result optical microscopy gave a good idea. With the help of these optical images, it became easier to locate the indents when the sample was placed in the SEM for investigation.

3.3 Nanoindentation results

Nanoindentation was carried out using M1 Hardness tester by Nanovea. The etched samples were glued to a firm base, to avoid any sample movement during nanoindentation testing. This was considered to be the best way to test the 3D printed samples, due to their porosity. In case of embedding the 3D printed samples in epoxy, there are chances that the epoxy entrapped in the pores of 3D printed sample might affect the true mechanical properties of the sample.

3.3.1 Hardness and elastic modulus results

3.3.1.1 Austenitic phase sample

The surface of the austenitic phase sample was flat, with small pits and clear grain boundaries as shown in Fig. 3-13.

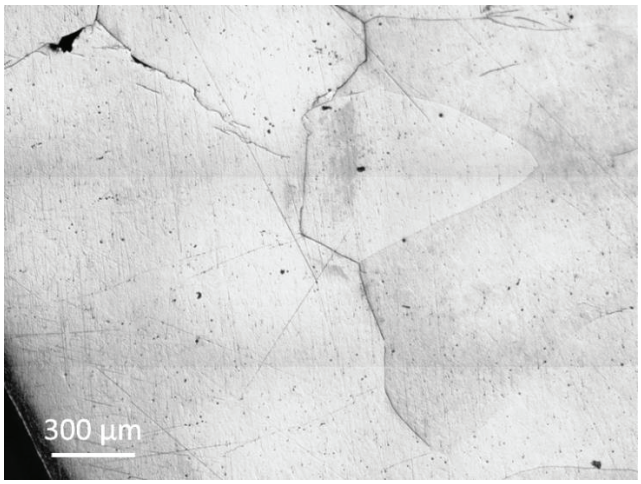

Figure 3-13 Austenitic phase sample

Nano-indentation was straight forward on the austenitic phase sample as compared to the martensitic phase sample. It was due to the absence of twin boundaries in the austenitic phase sample which are present in the martensitic sample. The additional hold period of

the 60s at the maximum load was applied for all the tests. The maximum depth or displacement of the indenter was found to be somewhere between 1.75 to 1.85 µm in case of bulk samples. The maximum load used for the bulk sample was 200 mN, which was applied with a loading rate of 300 mN/min.

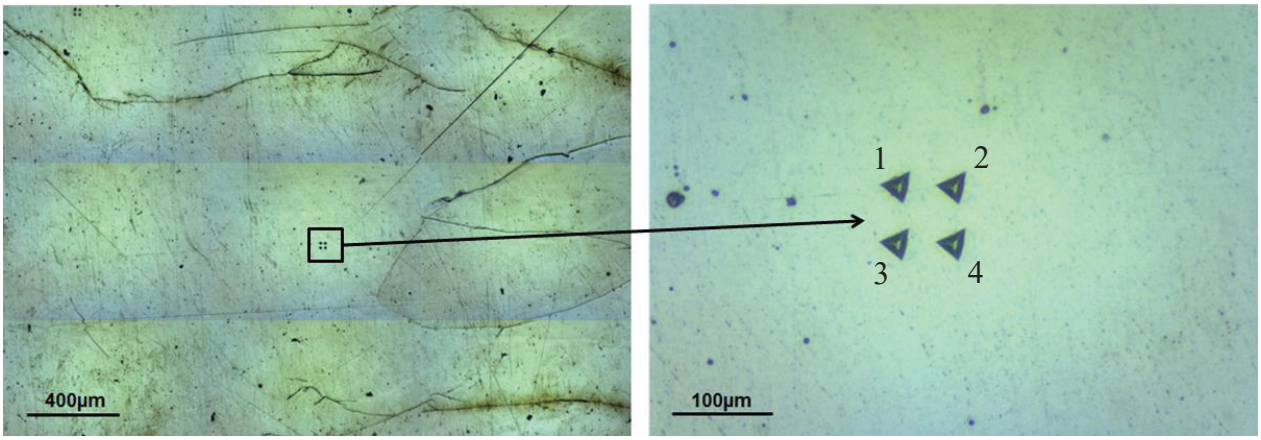

(a) (b)

Figure 3-14 Set of indents on the surface of austenitic phase sample (a) surface appearance at low magnification, (b) magnified image of indents

To statistically confirm the results, approximately 45-55 indents were done on the austenitic phase sample in sets of 4 and 6 indents. A set of four indents could be seen in Fig. 3-14 which was done using mapping function available in Nanovea software. This function helps to do multiple indents at an equidistant space defined by the user. The minimum distance of 15-20 µm was used between two indents to avoid any effect or stress around the indented surface of next indent. [28] Also, to confirm that the results are not affected due to any other external factor during 'mapping operation', many separate indents were done on the different parts of the sample, one at a time. The results from

such solo indents were found to be close to the results from mapped indents done in groups. This confirms that the experimental conditions were quite consistent and that there was no external factor affecting the indentation process. The tests results were recorded, as well as the location of indents was noted by giving numbers to the indent as shown in Fig. 3-14. Further, the load versus depth curve from a set of an actual test of indents is shown in Fig. 3-15. There is not much deviation in the curve, as well as the maximum depth of the indent. This confirms the consistency of the results.

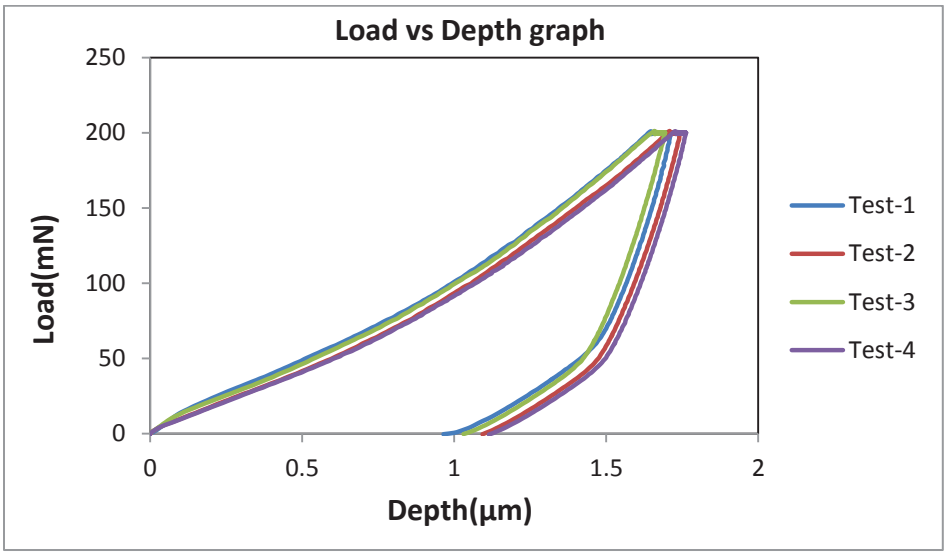

Figure 3-15 Load vs depth curve from a set of indents done on austenitic phase sample

Pseudoelasticity was also noticed during the hold period, which was expected in the material. It is the material reformation elastically after undergoing deformation due to external loading. Detail discussion on pseudoelasticity is done in subchapter 3.4.2. Fig. 3-16 depicts the image of the phenomenon encountered during the test. It is important to know that as discussed before pile-up around the indent was found for a few tests and were not considered for calculation of the mechanical properties.

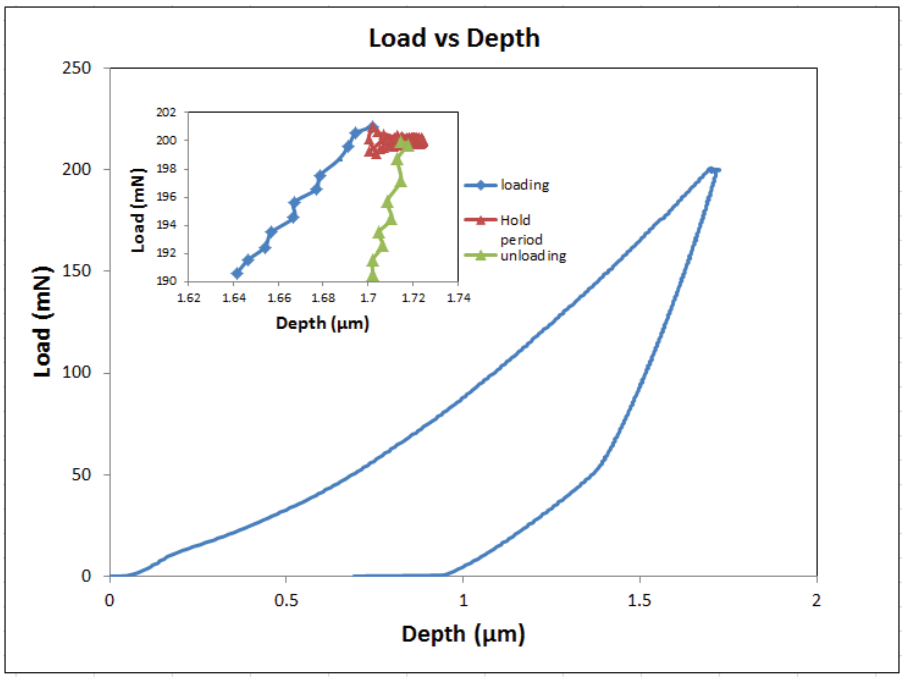

Figure 3-16 Pseudo-elasticity in austenitic sample

Out of 45 tests done on the austenitic sample, 39 tests were selected for calculation of hardness and elastic modulus of the material. They were selected on the basis of maximum depth of indent and visually analyzing the indent shape. The yellow highlighting on the number shows beginning of results for new sets of indents.

Table 3-1 Nanoindentation results for austenitic sample

	No.	Hardness (GPa)	Elastic Modulus (GPa)
Set-1	1	3.234341248	56.24878941
	2	3.364785869	57.37687804
	3	4.342565431	69.21943687
	4	5.464671771	79.44210202
	5	4.551373212	70.03416395
	6	3.819553411	62.3437236
	7	3.936607224	62.52097993

	No.	Hardness (GPa)	Elastic Modulus (GPa)
	8	5.086546895	73.51501521
	9	4.973544486	73.08730109
Set-2	10	3.816575923	61.55965769
	11	3.424635534	59.48033512
	12	2.968360457	55.73877722
Set-3	13	3.275112812	89.96867468
	14	2.904747683	77.97881182
	15	3.30456769	84.30543035
	16	3.207740173	83.38230027
	17	3.388469191	85.7735107
Set-4	18	3.696129991	68.83506881
	19	3.483191745	67.28352886
	20	3.590180442	66.42981042
	21	3.533196098	66.24054986
Set-5	22	4.227113311	95.75230124
	23	3.639333178	86.93099546
	24	3.906859005	90.53232884
	25	3.545645824	86.66737616
Set-6	26	3.707615852	86.76307196
	27	2.970425324	83.64828788
	28	2.910936626	77.24320269
	29	2.952512551	80.09508394
Set-7	30	3.033751628	79.95971926
	31	3.583098415	90.54298346
	32	3.688286647	88.75718051
	33	3.64523079	89.31581408
Set-8	34	4.913802432	93.22662723
	35	4.28560964	78.45622736

	No.	Hardness (GPa)	Elastic Modulus (GPa)
	36	5.539274084	91.98970393
Set-9	37	3.471719611	103.3951921
	38	4.27092657	95.71546471
	39	5.461053212	111.3638277
	Avg.	**3.823592102**	**79.00308293**
	SD	**0.740223651**	**13.59988134**

The analytical results obtained are documented in Table 3-1, along with the average value and the respective standard deviation. It is important to note here that all tests were done at RT. Analyzing the results it is prominent that the results were found to be in three different ranges, 3-4 GPa, 4-5 GPa and 5-5.5 GPa for hardness result. Also, with a higher range of results, the elastic modulus value corresponding to it also increases. It is suspected to be related to different grain orientation.

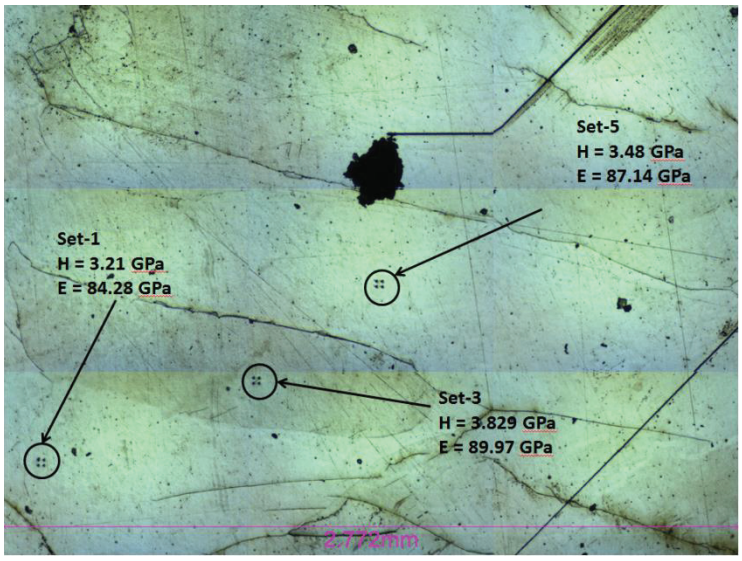

Figure 3-17 Mapped image with indents on different grains

The change in results with the grain orientation was confirmed by mapping the sets of indents in a single collated micrographs and compare the average results obtained from different sets. Fig. 3-17 depicts the image for austenitic sample, for comparison of results. It should be noted that the deviation in results could be seen on different grains. One of the future tasks would be to obtain an electron backscattered diffraction data of the surface using SEM, to scrutinize the results according to grain orientation. This would solidify the explanation and give profound knowledge of the effect of grain orientation on the mechanical properties of the material.

3.3.1.2 Martensitic sample

Twin boundaries as well as grain boundaries had been observed on the surface of the martensitic phase sample and can be seen in Fig. 3-18. The pits and unevenness of the surface make the indentation process challenging as compared to when done on a flat surface.

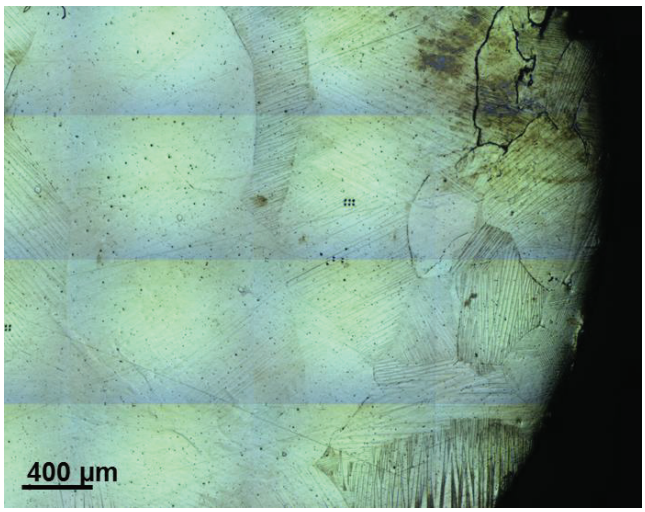

Figure 3-18 Martensitic phase sample

Fig. 3-19 (a) and (b) displays the indentation test conducted on a flat surface which is mostly in case of austenitic phase sample, while Fig. 3-19 (c) and (d) exhibit the nanoindentation test on a cross-section of the twin boundary surface.

Figure 3-19 Indentation test on different types of surfaces: (a) before indentation on a flat surface, (b) after indentation on flat surface, (c) indentation on the twinned surface, (d) after indentation on the twinned surface

In Fig. 3-19 (d), an indentation on the edge of a twin, which is suspected to eventually end up in piling up of material around the indent and thus the test result, may have some error. It is very important to confirm that indent is done on flat surface so as to get a perfect triangular plastically deformed area from the test.

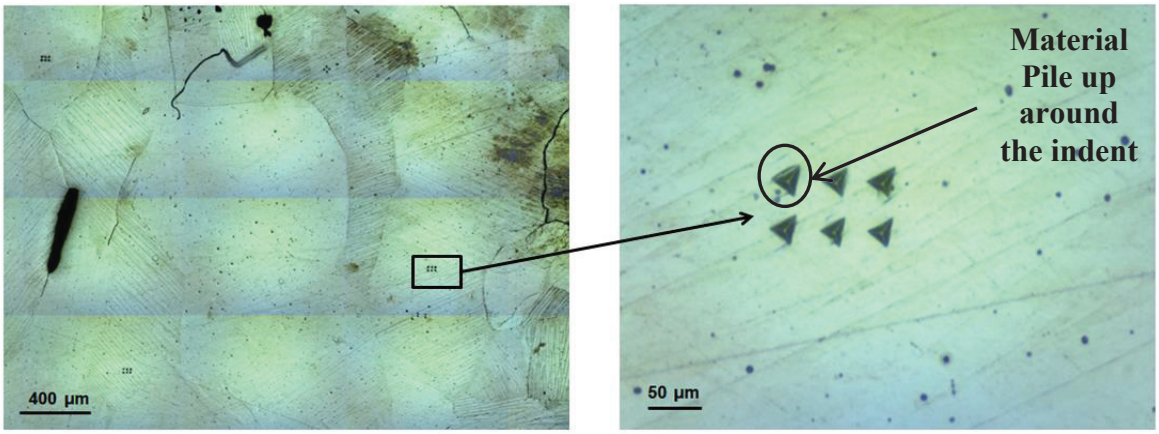

Figure 3-20 Indentation on the martensitic sample: (a) surface view, (b) magnified image of indents

Fig. 3-20 depicts the nanoindentation done on the martensitic sample, wherein Fig. 3-20 (b) a pile up around one of the indents can be seen clearly. The parameters used for

indentation on the martensitic sample were the same as that were used in the austenitic phase sample to be consistent with testing parameters. Fig. 3-21 shows the load versus depth curve from a set of tests conducted on the martensitic sample.

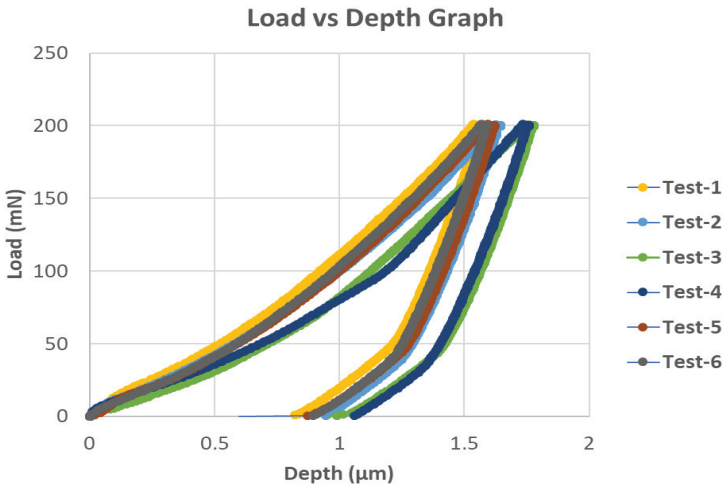

Figure 3-21 Load vs Depth curve from a set of actual indents done on martensitic phase sample

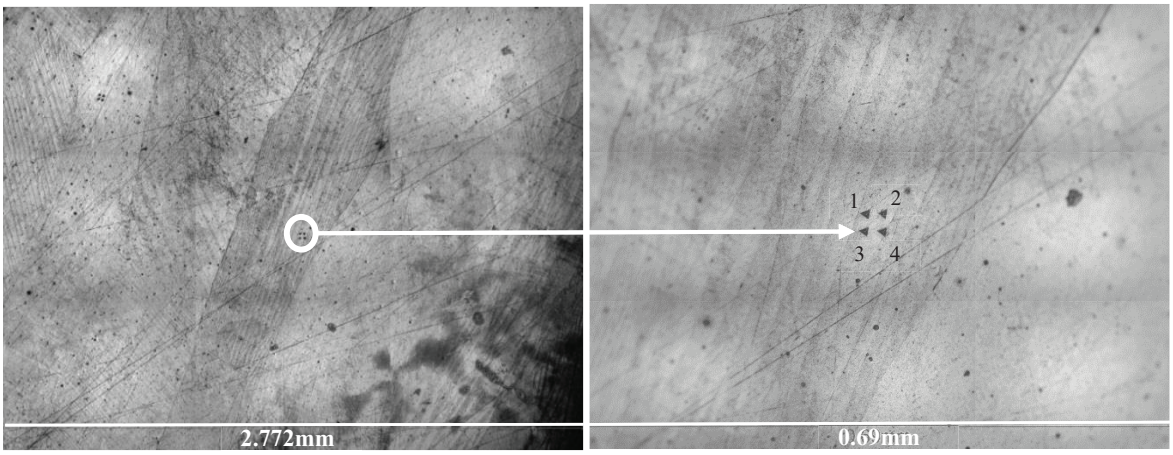

(a) (b)

Figure 3-22 Indents on twin boundaries in the middle of a grain: (a) surface view, (b) magnified image of indents

The plots shown are consistent, and the average depth was close to what was found in the austenitic phase sample. Also, the shape of the indents helps confirm that the projected area is quite sharp. There were several tests conducted on the twin boundaries, grain boundaries and in the middle of the grain, as shown in Fig. 3-22.

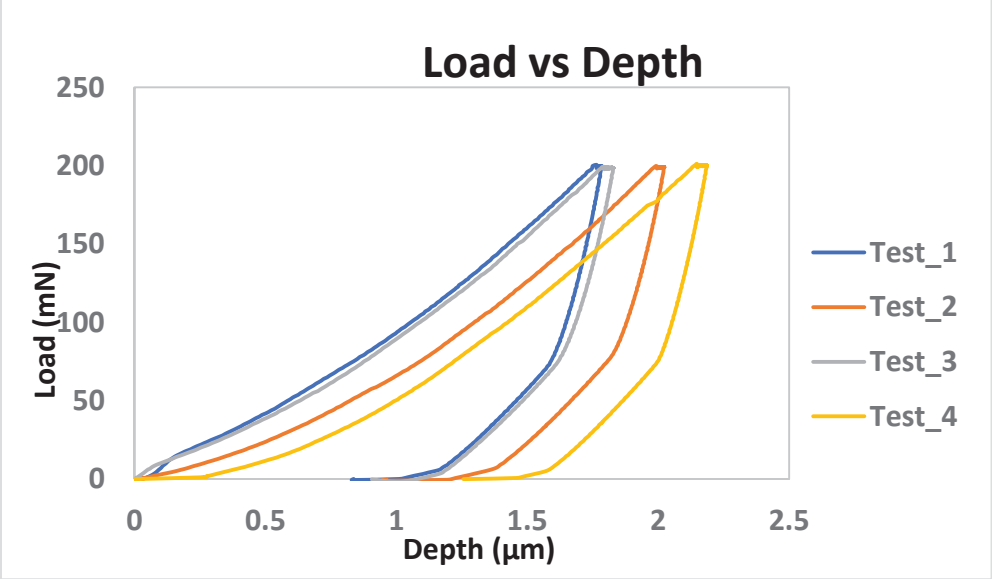

Figure 3-23 Plots from indents done at the middle of the grain in a martensitic sample: (1) Test-1: on a twin surface, (2) Test-2: on transition of two twins, (3) Test-3: on corresponding twin, (4) Test-4: on the twin at lower height as compared to first twin

In Fig. 3-23 from the plot for test-2, it could be determined that due to indent location on the transition of two twins, the depth increased by few hundread nanometers as compared to test-1. Also, the plot for test-4 is from indent-4 in Fig. 3-22 (b), done on the twin boundary which had a different orientation as compared to the corresponding twin. This could be seen from the change of contrast in Fig. 3-22 (b) and thus resulted in higher indentation depth.

Table 3-2 Results from the tests done on different places of a twin domain

Test	Max Load (mN)	Max Depth (μm)	Hardness (GPa)	Elastic Modulus (GPa)
1	198.844	1748.40	3.540269	98.8070
2	198.666	1982.35	2.526029	76.4183
3	198.2552	1781.37	3.198517	86.6097
4	199.3909	2132.90	2.127401	75.6533
Avg.	198.7893	1911.25	**2.848054**	**84.3721**
SD	0.407871	156.183	**0.553405**	**9.38955**

There were few failed tests which were not considered for calculation. One of the failed set of indents is shown in Fig. 3-24. The issue with the indents was the shape of the triangular area. As seen in Fig. 3-24, the indent shape is not forming a perfect equilateral triangle and rather looks like an isosceles triangle. It is clear from the shape that, one of the triangle sides is shorter than the other two, depicting that the surface was not completely flat with respect to the indenter.

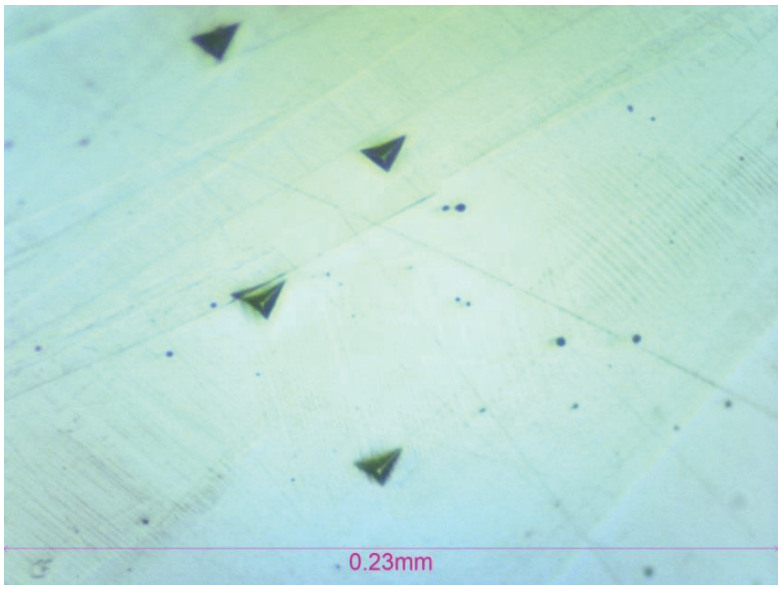

Figure 3-24 Failed tests

There were more than 75 indents done for martensitic phase sample, due to such complexity for test on this material. The indents with proper shape were chosen for calculating the average hardness and elastic modulus value of the martensitic sample. Table 3-3 below documents the values used for calculating the average hardness and elastic modulus of the material.

Table 3-3 Results from the martensitic sample

	Test no.	Hardness (GPa)	Elastic Modulus (GPa)
Set-1	1	1.534825017	69.73164479
	2	3.206818155	88.09313317
	3	3.021909316	88.2534986
	4	3.421723722	108.3941339
Set-2	5	3.366970007	99.28899657
	6	3.248308236	111.6353129
	7	3.444538545	105.4218594

	Test no.	Hardness (GPa)	Elastic Modulus (GPa)
	8	3.284876663	113.0496442
Set-3	9	3.540269019	98.80701889
	10	2.526028653	76.41829724
	11	3.198517155	86.60978762
	12	2.127401494	75.65329543
Set-4	13	1.282819055	98.10941448
	14	1.492221773	88.84282651
	15	3.066210069	106.1836102
	16	2.411345524	103.2796043
Set-5	17	2.762458432	66.88439873
	18	2.425726298	69.12917265
	19	3.09411243	131.4144064
	20	2.997835787	108.3065733
Set-6	21	2.058492988	71.36799632
	22	2.005004488	71.02932789
	23	2.958222892	91.91970417
	24	2.578589529	83.68696229
Set-7	25	2.847340041	88.67471016
	26	2.65317851	90.11852249
	27	3.16685651	103.3125473
	28	3.063188302	97.79227132
Set-8	29	3.569833731	110.7091546
	30	2.867746642	98.11362602
	31	3.335009028	110.5906484
	32	2.709289594	104.5233521
Set-9	33	2.882945231	70.36118177
	34	3.479963183	75.34208527
	35	3.167410544	71.47912586

	Test no.	Hardness (GPa)	Elastic Modulus (GPa)
	36	2.819406463	72.0922612
	37	3.611359226	82.36265842
	38	3.220071208	74.4367508
Set-10	39	3.904287113	131.7555646
	40	1.929528211	84.35223633
	41	2.700541887	106.348286
	42	2.935342019	105.0820116
	43	1.980483732	93.22704433
	44	1.063770417	64.3516769
Set-11	45	3.166137235	90.1838999
	46	2.203478935	72.03990433
	47	2.27322501	72.18913102
	48	1.632567177	62.45652746
	49	2.46909769	76.50540054
Set-12	50	1.49255291	67.67836288
	51	2.243616092	86.67884245
	52	1.839338232	82.17399435
	53	2.85489441	102.2300564
	54	2.41601716	94.03866609
Set-13	55	2.861006243	49.08527948
	56	2.812198434	48.77492069
	57	2.955426134	50.63043682
	58	3.136884991	52.65141098
	59	2.98828809	49.64834052
Set-14	60	2.313582315	56.34038042
	61	2.871280307	53.25606

	Test no.	Hardness (GPa)	Elastic Modulus (GPa)
	62	2.599368607	50.87911033
	63	2.703592955	49.41989181
	Avg.	**2.71103698**	**84.33963416**
	SD	**0.621109026**	**20.71805946**

In all, it was found a standard deviation of about 0.62 GPa in hardness, and about 20.72 GPa for elastic modulus. This clearly indicates the morphology of surface affected the results up to a great extent. Also, a decrease in hardness was found when compared to austenitic sample, which was in accordance with the expectation. It is important to note that all tests were conducted at room temperature, and thus the samples were in the martensitic phase, as mentioned previously. There are several reasons for standard deviations in the results, which includes small calibration errors in the instrument as well as human error while testing.

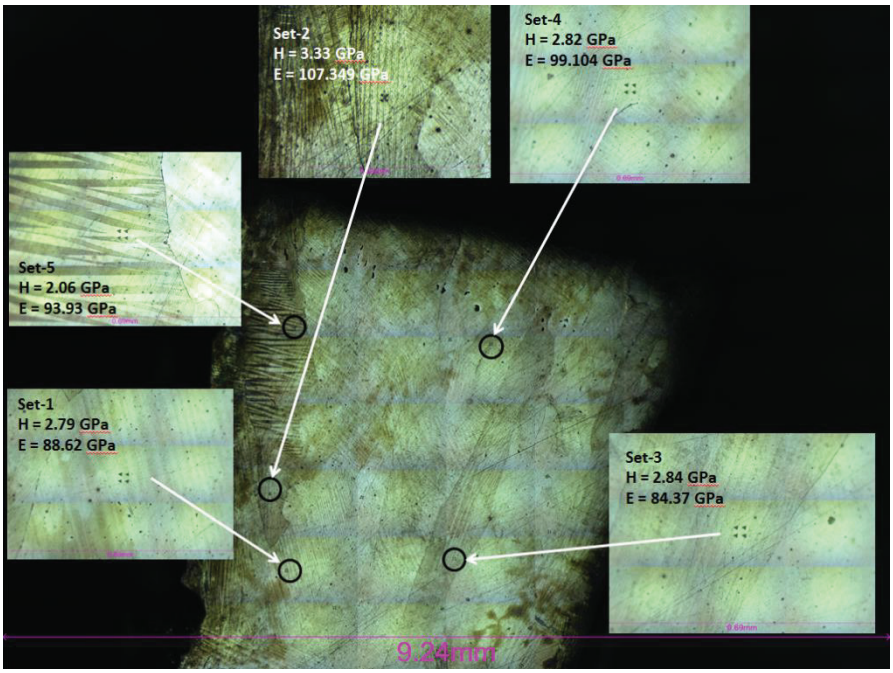

Figure 3-25 Mapped image with indents on different grains

Another explanation might be related to the different crystallographic orientation of grains in the material as found in the austenitic phase sample. Fig. 3-25 shows the indentation results from a different set of results on the martensitic sample. Due to crystallographic anisotropy, grain orientation relative to the indentation direction affected the experimental results, which could be confirmed from different hardness (H) and elastic modulus (E) results.

3.3.1.3 3D Printed sample

Additively manufactured samples were porous and were difficult to polish as compared to the bulk samples. Due to the porosity, it was very important to select proper spots on the surface for nanoindentation testing. Fig. 3-26 depicts the morphology of the 3D printed sample surface.

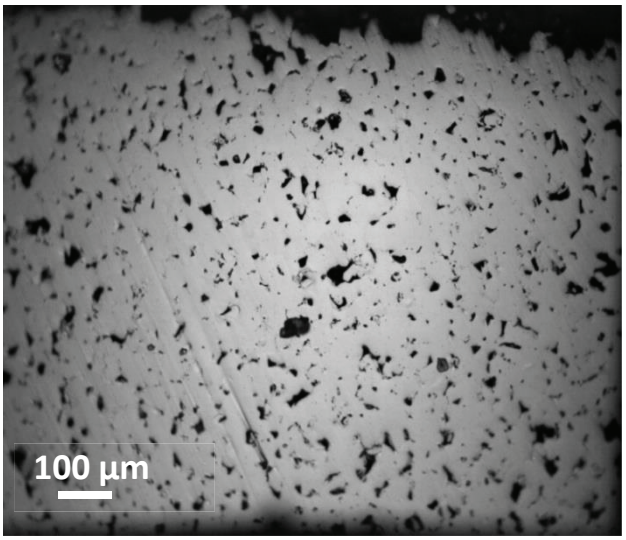

Figure 3-26 24 hrs. sintered 3D printed sample

Due to different flaws on the sample surface as well as below the surface, it becomes very important to analyze the indent shape and distance between the nearest pore or deformity. The area around the indent should also be thoroughly checked for any signs of surface deformity or pit which could act as a stress concentrator.

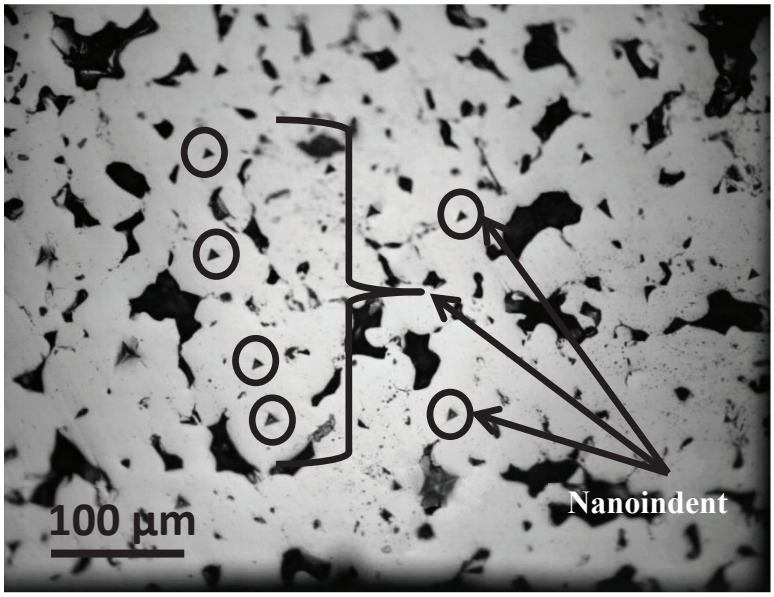

Figure 3-27 Group of indents done on 24 hrs. 3D printed sample

As shown in Fig. 3-27 nanoindentation tests were carried out at different spots for checking the consistency in the results. It was difficult to conduct indentation, as the distance of the indent from any surface deformity was not more than three indents. But to statistically analyze the tests, a standard deviation was found for the results and averaged out value was calculated. Also, any crack nucleation from the nearby surface was checked, so as to see if any flaw has affected the indentation test. Samples were sintered at 1353 K temperature for three different time periods were, 24 hrs., 40 hrs., and 50 hrs. It was found that with an increase in the time period the density of the sample increased making it less porous and allotting more space for indentation on the surface. It was found that the change in results for the samples sintered for the 24 hrs., 40 hrs., and 50 hrs. time period was negligible for hardness and elastic modulus. In Fig. 3-28, an indent did on the surface deformity is shown. It is clear from the optical micrograph that the triangular indent is completely distorted, and the result of mechanical property cannot be considered accurate.

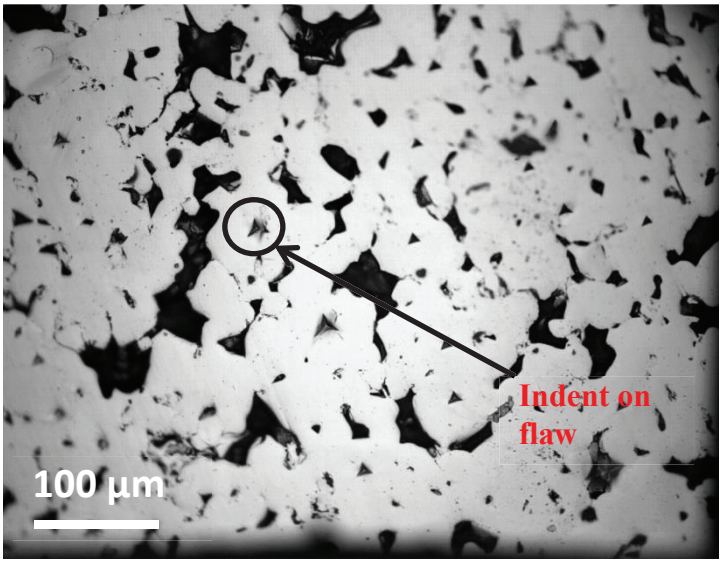

Figure 3-28 Failed test on 24 hrs. sintered sample

Further, the experimental parameters used for the 3D printed samples were kept similar to what was used for bulk samples for consistency in results.

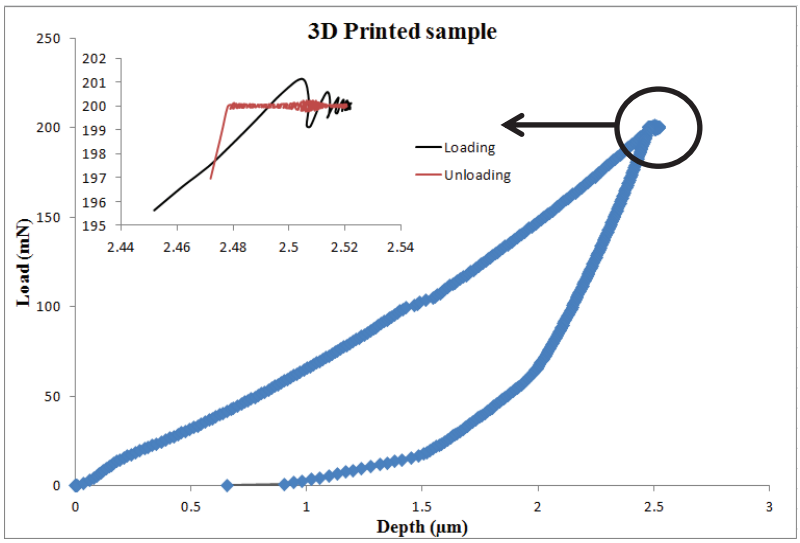

Figure 3-29 Load vs depth plot for 24 hrs. 3D printed sample

It was interesting to see the viscoelastic nature of the material shown by the smaller plot in Fig. 3-29. Fig. 3-29 is the load versus depth plot obtained from nanoindentation testing conducted on 24 hrs. 3D printed sample. The detail view of the hold period in the small plot on the left is quite interesting as we can see the negative depth on the plot. Normally while conducting a test with the hold period, it is expected that the depth would change positively or would stay constant. But, Ni-Mn-Ga alloy possess pseudoelasticity, which means with time the material makes effort to reform its original shape which would eventually end up as sink-in of material. In general cases, the hold period might not play an important role if the material has no pseudoelasticity. But, Ni-Mn-Ga is a shape memory alloy, and it tries to recover from the stress-induced deformation and thus the negative depth can be seen on the plot. It is quite interesting to note that the material itself

is trying to push the indenter in upward direction, while the test is still been conducted. This type of behavior was also noted in pure austenitic phase sample, and so hold timing played an important part in the experiment.

Table 3-4 Results for 3D printed sample

Test	**Hardness (GPa)**	**Elastic Modulus (GPa)**	**Sintering time (hrs.)**
Test 1	1.825604952	24.71078481	24
Test 2	1.965794624	23.66466451	
Test 3	2.338897228	34.46614475	
Test 4	2.05594485	29.67535569	
Test 5	2.624846354	36.1517522	
Test 6	2.54151986	35.43729893	
Test 7	2.045110796	28.90419595	
Test 8	1.808270195	22.45799823	
Test 9	0.9075442	13.75542888	
Test 10	1.921740877	19.12965619	
Test 11	1.853937528	19.73435727	
Test 12	1.470327235	45.0229484	
Test 13	1.543641408	49.34919975	
Test 14	1.687078809	47.82587215	
Test 15	1.269472404	48.05693537	
Test 16	2.10276251	31.6754977	
Test 17	2.301631954	40.1031067	
Test 18	2.151740744	41.21420086	
Test 19	2.220873658	30.92311418	
Test 20	2.025452494	41.21013446	

Test	Hardness (GPa)	Modulus (GPa)	
Test 21	2.717711754	43.58268589	
Avg.	**1.97047164**	**33.66911109**	
SD	**0.440690473**	**10.4974308**	

The depth of indentation also increased as compared to the bulk part, and it determines that the material when 3D printed losses some amount of mechanical strength resulting in low hardness value. Table 3-4 displays the hardness and elastic modulus values obtained from 3D printed sample.

3.4 Yield strength results

Yield strength tests were more complex in comparison to the nanoindentation testing with Berkovich indenter, as flat tip indenter had to be used. It is used because of the constant area of contact between indenter tip and surface, which makes the elastic-plastic deformation transition smooth. Several indents were done on the surface of all the three types of sample, using the flat tip indenter, to statistically determine the yield strength of the material.

3.4.1 Bulk Ni-Mn-Ga sample

The tests for austenitic and martensitic samples were conducted using the same nanoindentation technique used for evaluating the hardness and elastic modulus, but with a different shape of the indenter. The tests were conducted at 150 mN, 200 mN, 250 mN, 300 mN, and 375 mN as the maximum load at different spots on the sample. The loading-

unloading rate was used as 300 mN/ min. It is because, at a very small loading rate, the material was rigorously forcing the indenter in the backward direction while unloading as shown in Fig. 3-30.

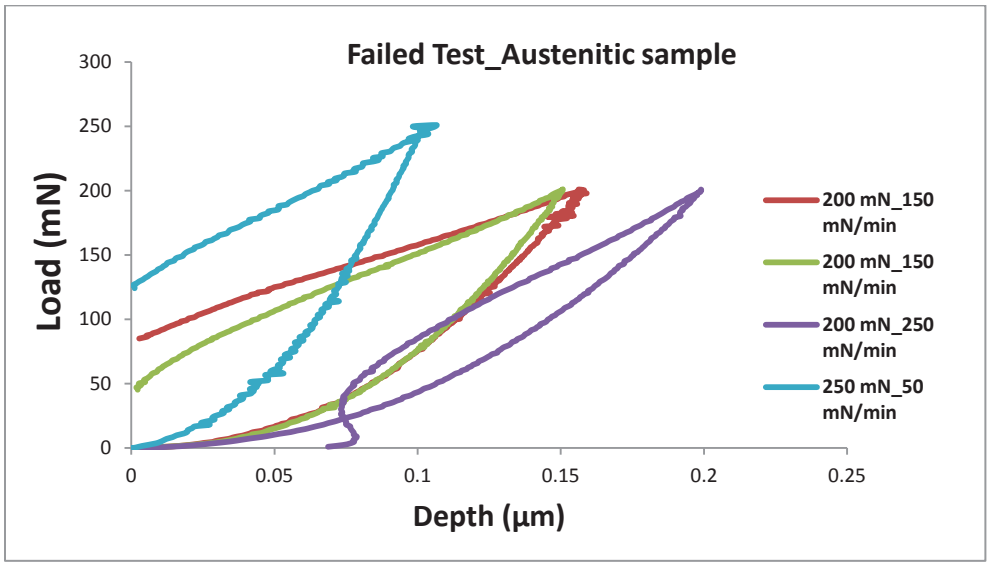

Figure 3-30 Load vs depth plot for failed test on austenitic sample

At low unloading rates, consistency could not be achieved in the results. Fig. 3-30 shows the plots obtained while testing the austenitic sample, with very low loading and unloading rate between 50 to 250 mN/min. Although the depth was expected to decrease as the flat indenter was used, but from the plot, we can see the depth is almost negligible which looks inaccurate. One of the reasons for such behavior of the material is its ability to regain its shape spontaneously, which means the material was actively trying to resist the deformation elastically while loading cycle. The additional push from the material was noted by the negative depth seen on the plot in Fig.3-30. So, to overcome this error, the loading rate used was 300 mN/ min. Further, it was suspected that the maximum load

used was not enough to deform the material plastically, due almost full recovery of the deformation.

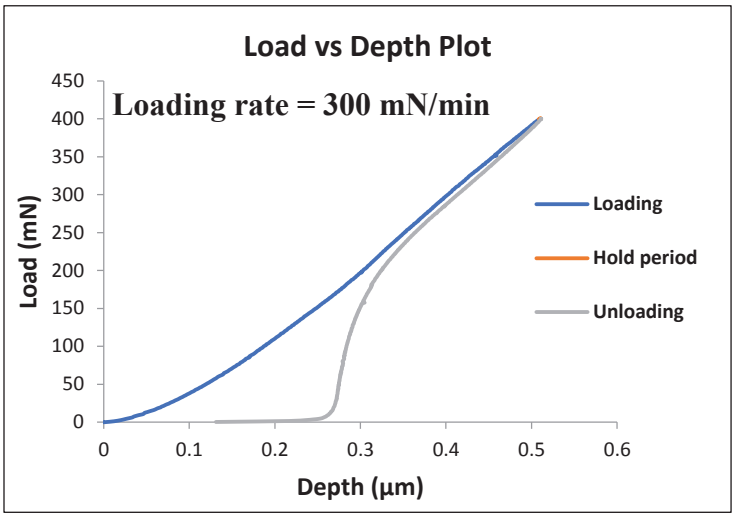

Figure 3-31 Load versus depth plot for austenitic sample

Fig. 3-31 depicts the plots from the initial test done for the maximum force of 390 mN that could be applied using nanoindentation machine, at a loading-unloading rate 300 mN/min. Material has a nature to transform from austenitic to martensitic phase under external loading, which further undergoes twin rearrangement in martensitic phase with the excess load. During the whole phase transformation and rearrangement, the deformation is mostly elastic and can undergo total shape recovery. The same phenomenon is suspected to happen in this case. More detailed discussion on the phenomenon of pseudoelasticity is provided in Section 3.4.3. In conclusion, it was determined that the maximum load for testing was not enough to yield or at least force the material to deform plastically.

The martensitic sample was also tested using the same technique with different maximum loads. Again, as it was a bulk sample, the loading rate used was 300 mN/ min for testing. Few tests were also conducted at 250 mN/min to see the difference in maximum depth, as well as material behavior in the martensitic phase.

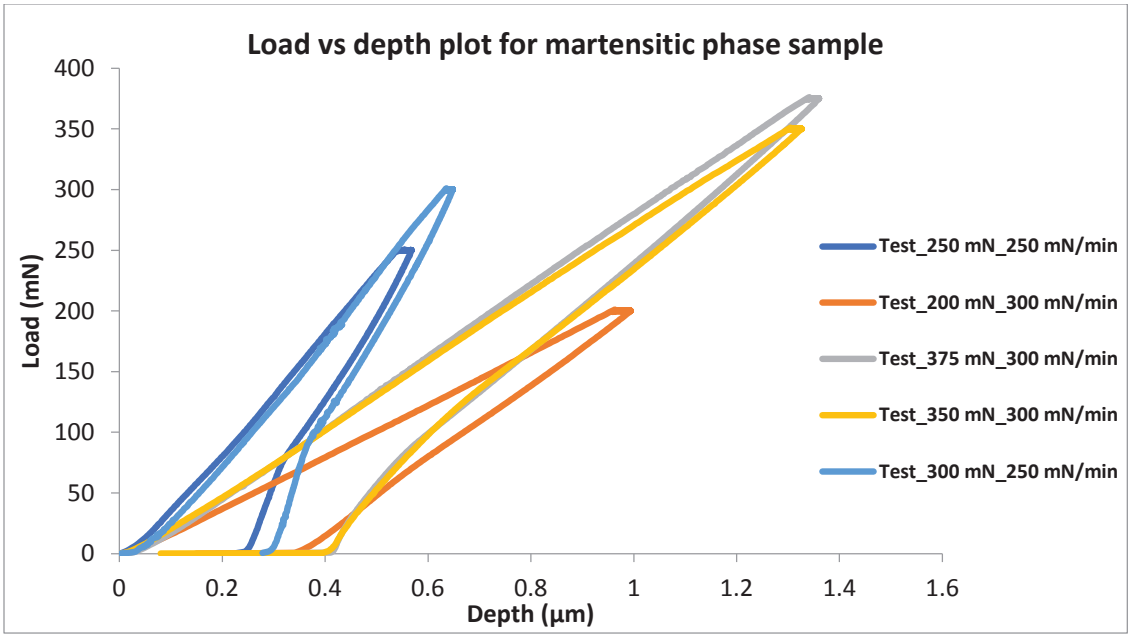

Figure 3-32 Plots for martensitic phase sample for different loading rates

The plot showed in Fig. 3-32 depicts the material behavior in the martensitic phase for different loading rates. Material resistance was proved from the previous test plots. So, test for 200 mN load was expected to have lower depth than for the test done for 250 mN and 300 mN as maximum load, as the total load to be applied was lower. But the loading rate for 200 mN load was higher than as compared to the other two tests done for 250 mN and 300 mN load. And thus, we can see the slope for loading curve for the test done at a lower loading rate is higher as compared to tests done with high loading rate. For austenitic sample, the phase change would resist the yielding of material, but in this case,

the sample was already in the martensitic phase. So, the question arises what was resisting the material from yielding? It was due to twin reorientation in the material. It is demonstrated that the martensitic twins are quite mobile and requires less force to change its orientation. [3] Thus, the martensitic twin reorientation is suspected to have resisted material's yielding by dispersing the stress in the form of twin reorientation. In conclusion, the load applied was again not enough to yield the material. This is one of the limitations of the nanoindentation machine, that the maximum load that could be applied is 400 mN, and which is not enough to plastically deform the material. Also, the material is brittle in nature, which means the yielding in the material would be very small. It is expected that the material after undergoing plastic deformation, would directly nucleate a crack or fail without yielding.

3.4.2 Pseudoelasticity

Ni-Mn-Ga alloy possesses a shape memory effect governed by a magnetic field as already discussed previously. But, the material also possesses pseudoelasticity, when comes under external loading. Ferromagnetic shape material shows deformation recovery up to 10 %, in the martensitic phase, under external magnetic field or mechanical load respectively. The response is caused due to pseudoelasticity in material, occurring due to the reorientation of twins in the tetragonal or monoclinic phase. [46] This makes the material unique and highly functional for several applications. Also, the recovery due to twinning is very fast, making the actuation frequencies of up to 2 kHz. [46] [47] The same phenomenon is occurring while conducting different indentation tests. Under external loading, the material undergoes a phase transformation from the austenitic to

martensitic phase. Here, the twin variants reorient while the loading cycle, to absorb the stress without undergoing failure. While the loading cycle stops and holds period starts, the load does not increase and is kept constant during this period. During this time period, the material tries to recover again, and this is considered to be a manifestation of the pseudoelastic effect. Fig. 3-16 and 3-29 depict the phenomenon occurring in Ni-Mn-Ga alloy. It is very unique to see such kind of behavior while conducting the nanoindentation test. As the deformation is mostly plastic while conducting the tests with Berkovich, it is expected that elastic recovery would be small. But, looking at the material behavior, it is highly active and starts pushing the indenter right from holding period. It is very complicated to get the stress-strain curve from load versus depth data for the indentation technique. [48] Future work, should focus on getting a clear idea about the amount of strain recovery by developing a model to convert the load versus depth plot to stress versus strain plot.

3.4.3 3D printed sample

Particularly, for the 3D printed samples, the test was more difficult. It was because the point of contact is a flat circular tip which has a larger diameter (20 μm) as compared to the sharp indenter. Fig. 3-33 depicts the yield strength test done on 3D printed sample. A perfect circular indent is visible, which was done at a maximum load of 400 mN. Fig. 3-34 displays the failed yield strength test done on 3D printed sample. It could be understood from Fig. 3-33 and 3-34 the difficulty with spot selection for the test as well as the surface deformities present on the 3D printed sample.

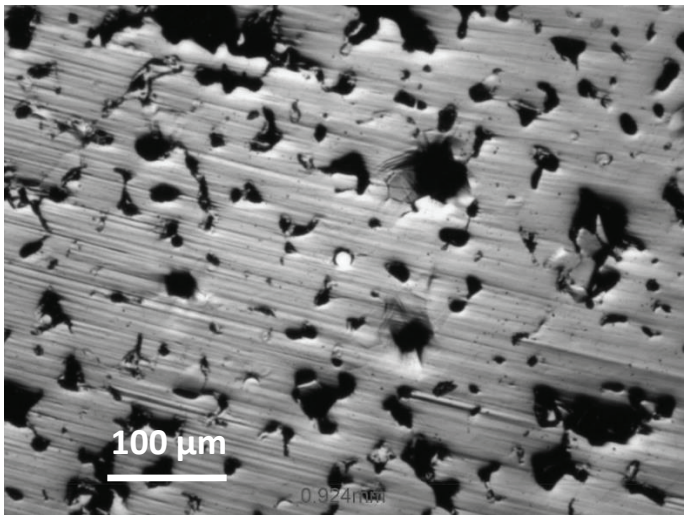

Figure 3-33 Yield strength test on 3D printed sample 50 hrs.

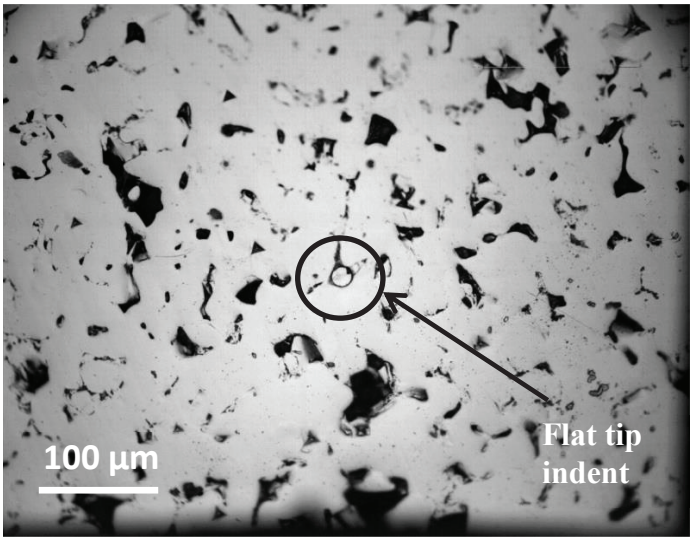

Figure 3-34 Failed test (yield strength) on 3D printed sample on 24 hrs.

There were several indents done on the 3D printed sample and Fig. 3-35 depicts the plots from different tests. It should be noted that the 3D printed sample had a mixture of both phases, austenitic and martensitic, at RT.

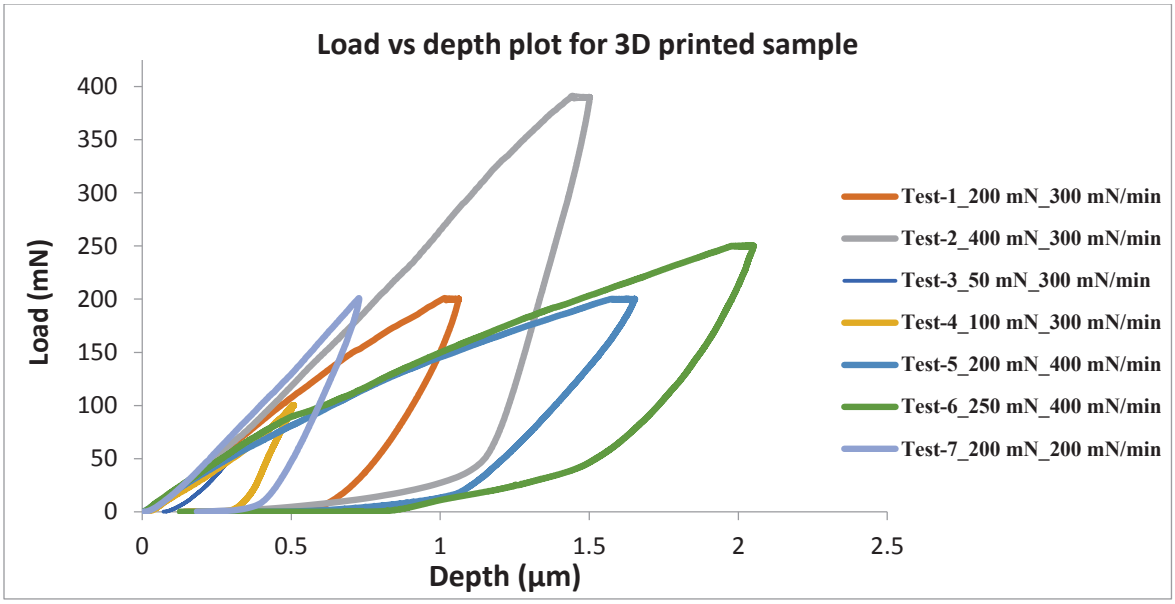

Figure 3-35 Plots for 3D printed sample sintered for 24 hrs., 40 hrs., and 50 hrs. for different loading rates

Test 1, 5 and 7 were done with the same maximum load of 200 mN, but with different loading rate. As seen in the austenitic and martensitic sample, the depth increases with increase in loading rate.

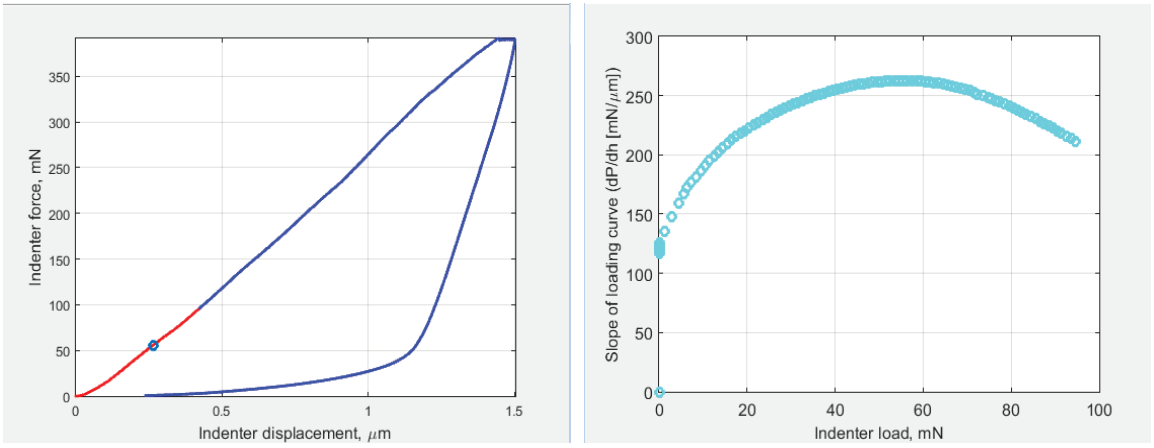

(a) (b)

Figure 3-36 MatLab plots (a) Load vs depth plot, (b) Slopes from loading curve vs indenter load

Several tests were conducted at different total load. The yield strength calculation was carried out for the 3D printed sample, using MatLab plots, as shown in Fig. 3-36. Firstly, analysis of result was done by keeping the loading and unloading rate same as 300 mN/min and results for 50 mN to 400 mN with an increase of 50 mN in each test. Results from the test are shown in Table 3-5. From Table 3-5, it is clear that the change in yield strength occurred after the maximum load of 200 mN. So further few tests were done at load higher than 200 mN force and eventually 300 mN load was set as a maximum load to conduct tests. The results from the analysis are tabulated in Table 3-6 with the average yield strength value and standard deviation respectively. The parameters highlighted in Table 3-5, for test-5 was further used to conduct tests at different spots on 50 hrs. sintered sample.

Table 3-5 Results for the 3D printed sample with different loads

Test no.	**Loading rate (mN/min)**	**Maximum load (mN)**	**Yield strength (MPa)**
1	300	50	483.18
2	300	100	491.07
3	300	200	634.19
4	300	250	561.42
5	300	300	553.46
6	300	350	536.39
7	300	400	638.49

Results were in a certain range, with deviation in accordance with what was found during the normal testing with a maximum load of 300 mN. Thus, from different tests results an averaged-out result was found to determine the yield strength of the material, which is as shown in Table 3-6. The value for yield strength obtained through the nanoindentation test would be somewhat high than the actual yield strength of the material. This is because indentation tests were done on separate grains and give data from a local grain on the material. While in the commonly used testing method the yield strength result obtained by plastic deformation of whole material part and this would give the averaged result.

Table 3-6 Results for the 3D printed sample sintered 50 hrs

Test no.	**Loading/Unloading rate (mN/min)**	**Maximum load (mN)**	**Yield strength (MPa)**
2	300	300	586.5
3			549.44
4			631.89
5			588.8
6			480.34
7			429.82
Avg.			**545.75**
SD			**69.197**

3.5 Fracture toughness results

As discussed in the experimental methodology chapter, there were two different types of models used based on crack type to determine the fracture toughness of Ni-Mn-Ga alloy samples. These models were based on radial and Palmqvist crack. [42] Table 3-7 shown below gives detail information about the different type of models used.

Table 3-7 Details about models used for fracture toughness calculations

Sample type	Tip used	Model type	Model detail	Ref.
Austenitic and Martensitic	Vickers	Radial crack	Anstis model	[40]-[42]
			Laugier's	
			Niihara's	
	Vickers	Palmqvist	Laugier's	
Sample type	**Tip used**	**Model type**	**Model detail**	
			Niihara's	
3D printed sample (sintered	Vickers	Radial crack	Antsis model	
			Laugier's	
			Niihara's	
3D printed sample	Berkovich	Palmqvist	Laugier's	

3.5.1 Austenitic phase sample

Nanoindentation technique was initially used to fracture the bulk part. But, the maximum force that could be applied using the nanoindentation instrument was 400 mN. This was not enough to yield the material itself as seen in previous sections 3.4.1 and 3.4.2, so there was no chance to nucleate a crack in the bulk samples with that load. Thus, microindentation machine was used whose maximum force capability was 100 N, to fracture the material. The amount of force available using microindentation machine was enough to crack the bulk part. The load used to crack the austenitic sample was found to

be 92.8 N. Fig. 3-37 shows a microindent done on the austenitic sample with 92.8 N force. It is interesting to note the formation of strain-induced martensitic twins around the material. This helps us understand the material behavior, namely austenitic to martensitic phase transformation, due to external loading. Ni-Mn-Ga alloy in the austenitic phase when comes under external force, it transforms into martensitic phase. This phenomenon occurs without any crack nucleation in the material and shows that material deforming elastically.

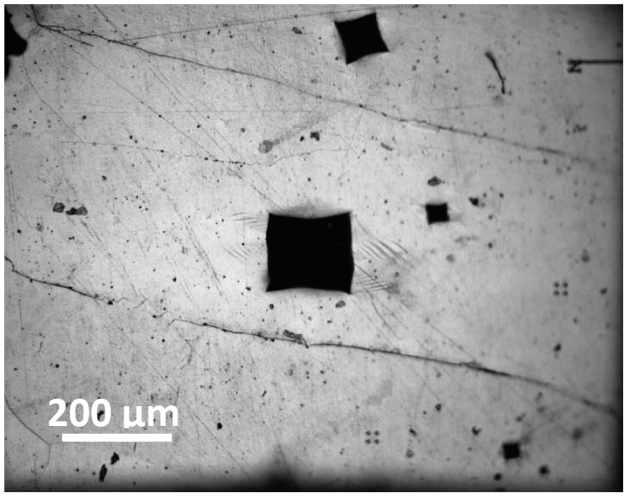

Figure 3-37 Microindent on the austenitic sample with martensitic twins around the indent

Further, on applying extensive load the material starts cracking from different indenter ends in line with the indent diagonal.

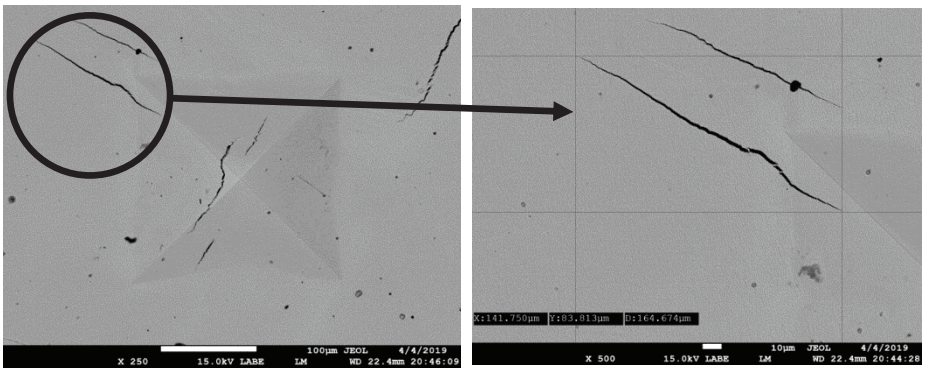

(a) (b)

Figure 3-38 SEM image of the microindent on austenitic phase sample: (a) top view of the indent, (b) detail view of the crack to calculate the crack length

So, the whole cycle of crack nucleation for austenitic part includes phase transformation into the martensitic phase and then fracture across the grain. It also depicts the material strength while it is in the austenitic phase (bulk part). Fig. 3-38 depicts SEM of the microindentation test done on austenitic phase sample. Scanning electron microscopy was used to determine the crack length as it is one of the most important aspects in determining the fracture toughness using indentation technique. All the models used, to calculate the fracture toughness highly relay on crack length. As shown in Fig 3-38 (b) the crack lengths were determined with high accuracy using SEM. There were three radial crack models were used to determine the fracture toughness: (1) Anstsis model, (2) Laugier's model and (3) Niihara's model. [42] Also, there were two Palmqvist models used which were proposed by both Laugier's and Niihara's with a minor change in the fitting constant and crack length ratios. [42]

Calculations:

From Fig. 3-38 (a) and (b) the following information were found:

Avg. diagonal length (a) = 150 µm, crack length (l) = 164.67 µm

❖ **Anstsis model:**

Equation is given as: $$K_{IC} = A * \left(\frac{E}{H}\right)^{1/2} * \left[\frac{P}{c^{\frac{3}{2}}}\right]$$

A = 0.016 (radial crack model), E = 3.8 GPa, H = 80.88 GPa, P = 92.8 N, c = 0.00031467 m (total crack length = avg. diagonal length + crack length)

$$K_{IC} = 0.016 * \left(\frac{(80.88)}{(3.8)}\right)^{\frac{1}{2}} * \frac{92.8}{0.00031467^{3/2}}$$

$$K_{IC} = \mathbf{1.227\ Pa\sqrt{m}}$$

❖ **Laugier's model (radial crack):**

Equation is given as: $$K_{IC} = X_v * \left(\frac{a}{l}\right)^{\frac{1}{2}} * \left(\frac{E}{H}\right)^{\frac{2}{3}} * \left(\frac{P}{c^{\frac{3}{2}}}\right)$$

X_v = 0.01, a = 0.000150 µm, l = 0.00016467 µm

$$K_{IC} = 0.01 * \left(\frac{(0.00015)}{(0.000165)}\right)^{\frac{1}{2}} * \left(\frac{(80.88)}{(3.8)}\right)^{2/3} \frac{92.8}{0.0003146^{3/2}}$$

$$K_{IC} = \mathbf{1.8522\ Pa\sqrt{m}}$$

❖ **Laugier's model (Palmqvist crack):**

Equation is given as: $$K_{IC} = X_v * \left(\frac{a}{l}\right)^{\frac{1}{2}} * \left(\frac{E}{H}\right)^{\frac{2}{3}} * \left(\frac{P}{c^{\frac{3}{2}}}\right)$$

$X_v = 0.015$, a = 0.000150 µm, l = 0.00016467 µm

$$K_{IC} = 0.015 * \left(\frac{(0.00015)}{(0.000165)}\right)^{\frac{1}{2}} * \left(\frac{(80.88)}{(3.8)}\right)^{2/3} \frac{92.8}{0.0003146^{3/2}}$$

$$K_{IC} = \mathbf{1.827\ Pa\sqrt{m}}$$

❖ **Niihara's model (radial crack):**

Equation is given as: $$K_{IC} = X_v * \left(\frac{E}{H}\right)^{\frac{2}{3}} * \left(\frac{P}{c^{\frac{3}{2}}}\right)$$

$X_v = 0.0309$

$$K_{IC} = 0.0309 * \left(\frac{(80.88)}{(3.8)}\right)^{\frac{1}{2}} * \frac{92.8}{0.0003146^{3/2}}$$

$$K_{IC} = \mathbf{2.5323\ Pa\sqrt{m}}$$

❖ **Niihara's model (Palmqvist crack):**

Equation is given as: $$K_{IC} = X_v * \left(\frac{E}{H}\right)^{\frac{2}{3}} * \left(\frac{P}{c^{\frac{3}{2}}}\right)$$

$X_v = 0.0089$

$$K_{IC} = 0.0089 * \left(\frac{(80.88)}{(3.8)}\right)^{\frac{1}{2}} * \frac{92.8}{0.0003146^{3/2}}$$

$$K_{IC} = \mathbf{1.502\ Pa\sqrt{m}}$$

The crack lengths from different tests used for calculating fracture toughness are documented in Table 3-8. There is some consistency in the crack length which could be found by comparing the lengths with average crack length value.

Table 3-8 Crack lengths obtained for different tests done on austenitic phase sample

Sample	Average diagonal length (m)	Crack length (m)	Total crack length (m)
Austenitic sample	0.00015	0.00016467	0.00031467
	0.00015	0.000123603	0.000273603
	0.00014375	0.00018373	0.00032748
Avg.	**0.000147917**	**0.000157334**	**0.000305251**

Table 3-9 Austenitic phase sample results

Sr. no.	Model	K_{IC} (radial) average value (Pa√m)	K_{IC} (Palmqvist) average value (Pa√m)
1	Anstis	1.298±0.189	
2	Laugier	1.9818±0.4066	2.0086±0.5271
3	Niihara	2.7094±0.5587	1.574±0.139
	Avg.	**1.996±0.706**	**1.7915±0.307**

The calculations were carried out for all the cracks, and results obtained from the analysis were as shown in Table 3-9. It is suspected that the indentation test on Ni-Mn-Ga alloy, produces a stress area in a shape of half-penny under the surface, with a radius of radial crack from indent. [11] In such condition the radial crack models would be considered to be accurate. So, averaged out the result from the radial crack model which is 1.996 Pa√m, can be concluded as fracture toughness of the material.

3.5.2 Martensitic phase sample

As seen earlier the twin boundaries were present all over the surface. It was found that initially, the material started cracking along the twin boundaries as seen in Fig. 3-39.

Generally, while focusing on something if the surface is perfectly flat or everything is at the same level, the whole field of view is focused to gather. But, the sample was in the martensitic phase and also tends to reform itself. So, it can see in Fig. 3-39 (b) that diagonals and center of indent cannot be focused together.

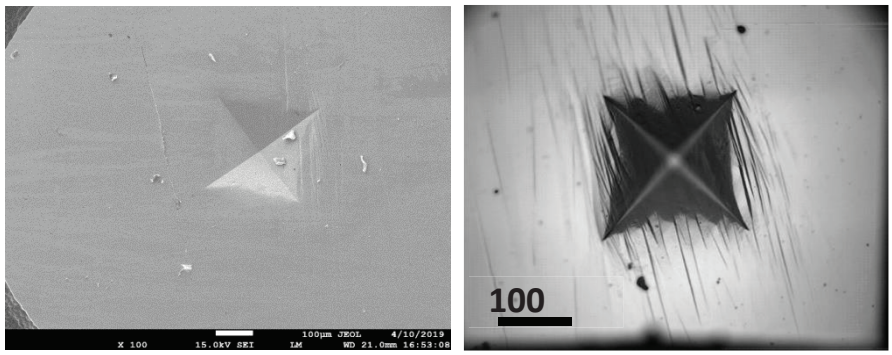

(a) (b)

Fig. 3-39 Microindent on the martensitic phase sample (a) SEM image, and (b) bright field light microscopy image showing the deformation of twins

Therefore, in conclusion by using only the optical microscope it was difficult to focus the whole indent area in a single image and so crack measurement using an optical microscope would be inaccurate. Fig 3-39 (a) depicts the SEM of crack propagation along the twin boundaries in the martensitic phase. It is very interesting to see that the material resisted the crack propagation across the twin boundary, and rather dissipate most of the load along the twin boundaries. The load used to crack the martensitic phase sample was 92.8 N which is the same as that used for the austenitic sample. A large amount of shifting of twin boundaries, as well as twin reorientation in a different direction, was noted around the indent shown in Fig. 3-40. This shows that the material

before undergoing failure tries to dissipate the externally imposed strain in a different direction through twin reorientation and shifts.

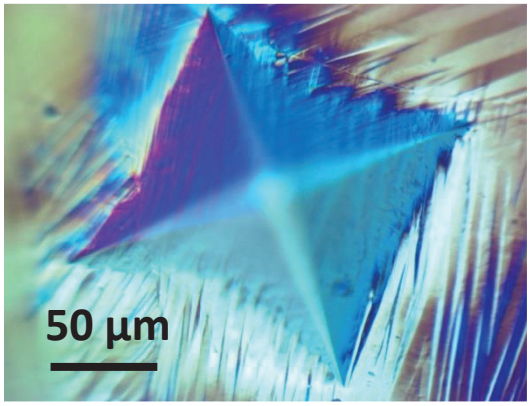

Figure 3-40 DIC image of twin orientation around the microindnet

Differential interference contrast (DIC) images display different orientation or surface twins by different colors as it could be seen in Fig. 3-40. Further, the models used for calculating the fracture toughness of martensitic samples were the same as the ones used for the austenitic sample. Same types of models were used in case of the martensitic sample as used for the austenitic sample. Table 3-10 below indicates the crack lengths obtained from different indentation tests.

Table 3-10 Crack lengths obtained for different tests done on martensitic phase sample

Sample type	Average diagonal length (m)	Crack length (m)	Total crack length (m)
Martensitic sample	0.00019	0.00053344	0.00072344
	0.000182	0.00014523	0.00032723
	0.00019375	0.0005829	0.00077665
	0.00016875	0.000451504	0.000620254
	0.000188	0.000209927	0.000397927
	0.000202	0.00019535	0.00039735
Avg.	**0.000187417**	**0.000353059**	**0.000540475**

From the average crack lengths, it can be concluded that the lengths increased as compared to the austenitic sample. This was expected as in the austenitic phase sample, the material undergoes phase transformation, reorientation and then eventually fail, while in the martensitic sample, there is no phase transformation. It undergoes only twin reorientation and tries to dissipate the stress along with the twin variants before cracking. Table 3-11 displays the result obtained for the martensitic phase sample.

Table 3-11 Fracture toughness results for martensitic sample

No.	Model	K_{IC} (radial) average value (Pa√m)	K_{IC} (Palmqvist) average value (Pa√m)
1	Anstis	0.808±0.417	
2	Laugier	0.897±0.463	1.963±0.926
3	Niihara	2.142±1.131	1.482±0.416
	Avg. value	**1.2823±0.745**	**1.7225±0.340**

The crack nucleation was found to be from diagonal ends of the indent but was not in line with the diagonal. This might lead to a question about what type of model could be considered accurate for the calculation. So, visually analyzing the crack under SEM, the twin boundaries were the first to crack. And the length of the crack was longer than indent diagonal length, suggesting the half-penny stress area is possibly formed under the surface. Considering that, the radial crack model was considered to be more accurate and fracture toughness for the martensitic sample was determined as 1.2823 Pa$\sqrt{m}$. There could be seen a decrease in the fracture toughness value of the martensitic sample, which was as expected. Austenitic phase samples are tougher to crack, as a large amount of force is used in transforming austenitic in to martensitic. Then the rest amount of work done is used for nucleating a crack in the material. Also, as seen in the martensitic phase sample, material tries to dissipate the stress along the twin boundaries by undergoing twin shifts and reorientation. And the same phenomenon occurs in the austenitic phase sample after it transforms into the martensitic phase. So, it can be concluded that more effort is needed to crack an austenitic phase sample, eventually resulting in higher fracture toughness than the martensitic phase.

Further, the percentage difference in the results for different models for the same sample was determined to understand the deviations in the results. Also, comparison of the results for austenitic and martensitic samples was done to determine the percentage difference in results for fracture toughness. This analysis for important to understand which models showed some consistency in the results, and which type of model was more accurate (radial or Palmqvist). Table 3-12 shows the comparison, and it determines

that there was more consistency in results for Laugier's and Anstis model for radial crack, as compared to Niihara's model. Also, the percentage difference for different sample such as austenitic and martensitic was inconsistent for all the models. (Note: In Table 3-1, with respect to is abbreviated as w.r.t.)

Table 3-12 Percentage difference in different models based on radial crack

	Radial crack models			
		Aust	**Mart**	**% difference between austenitic and martensitic**
	Anstis	1.298 Pa√m	0.81 Pa√m	37.596302
	Laugier	1.982 Pa√m	0.897 Pa√m	54.74268416
	Niihara	2.709 Pa√m	2.141 Pa√m	20.96714655
Laugier	% diff w.r.t. Anstis	52.69	10.74	
Niihara	% diff w.r.t. Laugier	108.70	138.68	

Similarly, the percentage difference for Palmqvist models was also prepared, and surprisingly it showed a less deviation in percentage difference of the results. Table 3-13 shows the table with results for an austenitic and martensitic sample.

Table 3-13 Percentage difference in different models based on Palmqvist crack

	Palmqvist crack			
		Aust	Mart	% difference between austenitic and martensitic
	Laugier	2.008 Pa√m	1.96 Pa√m	2.39
	Niihara	1.574 Pa√m	1.48 Pa√m	5.97
Niihara	% diff w.r.t. Laugier	21.61	24.48	

3.5.3 3D Printed samples

Additively manufactured samples were much weaker as compared to the bulk samples. It is probably due to the porosity present in 3D printed samples. One more issue with the 3D printed sample was the available area for conducting the microindentation on the material. As seen in the nanoindentation process, the amount of surface flaws is higher in 3D printed samples. Due to such reasons, the sintering time for the 3D printed sample was increased to enhance the necking between two particles of the material. The sintering process is conducted for 3D printed samples in argon environment to enhance their mechanical strength. The samples were sintered at 1353 K temperature for three different time periods, (1) 24 hrs, (2) 40 hrs, and (3) 50 hrs. The increase in sintering time helped in increasing the density of the material. On the contrary, from the results obtained for different samples, it was found that the increasing sintering time made the material more fragile and prone to cracking. 3D printed samples are porous and so some amount

of oxygen might be still entrapped between the particles, even after evacuating and purging the system with argon gas couple of times. This oxygen would then produce oxide layer in the necking between two particles while sintering process, disrupting the proper bonding of different particles. 3D printed sample strength depends upon the bonding of the particles, and in the case of oxidation, the material becomes more brittle. Thus, an increase in sintering time increases the density of the material but due to high oxidation internally, the part becomes more fragile. This could also be confirmed with a comparison of the crack lengths of the 50 hrs. sintered sample, and 24 hrs. sintered sample. There was an increase in the crack length for sample sintered for a longer time. This probably was the reason for the decrease in stress concentration factor (K_{IC}) substantially with an increase in sintering time.

3.5.3.1 Sample-1 (sintered 24 hrs.)

This sample was sintered for the least time period as compared to other samples. Figs. 3-41 and 3-42 show the top view surface of the sample. There are many pits and depressions all over the sample. For this reason, it had hardly any space to do a microindent on the surface. But, as the porosity in the material was higher it resulted in early fractures and at a comparatively lower load than the bulk samples. And thus, it cracked on a few instances while using nanoindentation machine.

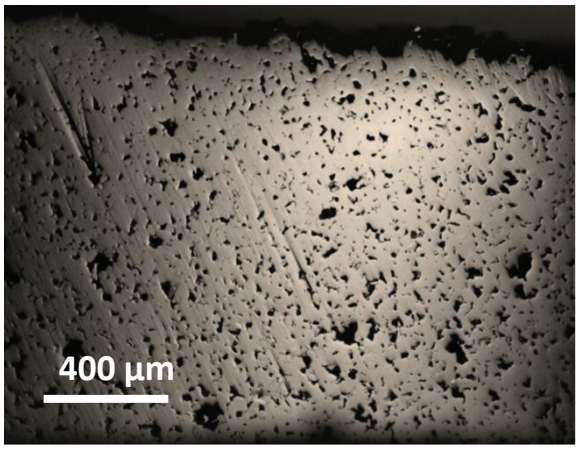

Figure 3-41 3D printed sample sintered 24 hrs.

Figs. 3-42 (b) and (c) shows the crack nucleation from a nanoindent. In Fig. 3-42 (a), on the right of the nanoindent, there is a failed microindentation test done using Vickers indenter.

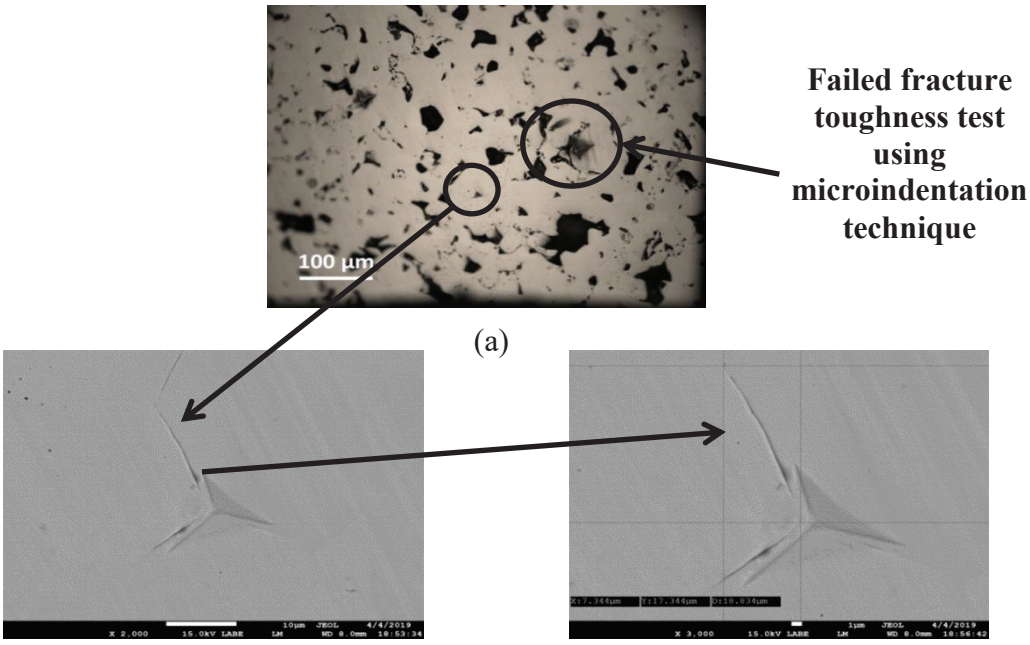

Figure 3-42 Light microscopy image and SEM image (a) Light microscopy of fracture toughness analysis using nanoindentation technique, (b) SEM of nanoindent b Berkovich indent, (c) crack length calculation

Calculation:

❖ **Laugier's model for Berkovich indenter (Palmqvist crack):**

The equation is given as: $$K_{IC} = X_v * \left(\frac{a}{l}\right)^{\frac{1}{2}} * \left(\frac{E}{H}\right)^{\frac{2}{3}} * \left(\frac{P}{c^{\frac{3}{2}}}\right)$$

X_v = 0.016, a = 0.0000153 µm, l = 0.00003528 µm, c = 0.000050608 µm, E = 33.67 GPa, H = 1.97 GPa, P = 1.25 N

$$K_{IC} = 0.016 * \left(\frac{(0.000012)}{(0.000009708)}\right)^{\frac{1}{2}} * \left(\frac{33.67}{1.97}\right)^{2/3} \frac{1.25}{0.000021708^{3/2}}$$

$$K_{IC} = \mathbf{1.459\ Pa\sqrt{m}}$$

The crack lengths obtained from different tests are tabulated below in Table 3-14. From the results obtained for the length of the crack, only those tests were considered for calculation, where crack length was less than or equal to the average diagonal length. It is because the model available for Berkovich indenter is dependent on Palmqvist crack. Here, the half penny-shaped stress area is not considered to be created due to indentation, and so the lengths of cracks are to be analyzed. The results in yellow from Table 3-14 were considered for fracture toughness calculation. The fracture toughness results obtained from various crack were calculated and the average value and standard deviation are shown below in Table 3-15. The results obtained for this sample were according to only one model based on Berkovich indenter.

The future work for this sample would be to conduct a focused ion beam analysis to look at the cross-section of the indent and area around it. It would help in confirming the results calculated for 24 hrs. sintered sample.

Table 3-14 Average crack lengths for 24 hrs. sintered sample

Sample type	Average diagonal length (m)	Crack length (m)	Total crack length (m)
3D printed sample sintered 24hrs.	0.00001533	0.000035278	0.000050608
	0.0000078	0.000010051	0.000017851
	0.0000083	0.00000565	0.00001395
	0.000012	0.000009708	0.000021708
	0.0000094	0.000007541	0.000016941
	0.0000094	0.00001757	0.00002697
	0.0000087	0.000018834	0.000027534
Avg value	1.01329E-05	1.49474E-05	2.50803E-05

Table 3-15 Fracture toughness results for 24 hrs. sintered sample (PQ – Palmqvist)

Model	Average value of K_{IC} (Pa$\sqrt{m}$)
Laugier's (PQ)	1.841 $\pm$1.016

3.5.3.2 Sample-2 (sintered 40 hrs.)

This sample was sintered for a longer time and had more surface area for conducting the microindentation tests to evaluate the fracture toughness value of the material. Vickers indenter was used to conduct the tests with a maximum load of 1.25 N on the surface. It is important to note that to propagate a crack from any flaw or deformity around the indent a certain amount of load has to be applied. [40] That load was found to be around 1.3- 1.4 N force by conducting a few tests near the flaws at different loads. It was found to be higher than the crack nucleation load in the material which was 1.25 N.

And thus, it was assumed that any flaw on or below the surface did not affect the test results indirectly.

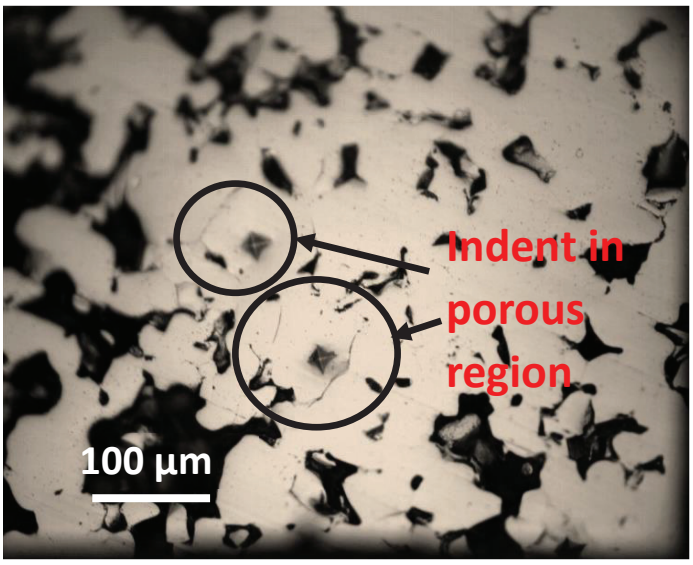

Figure 3-43 Failed test of 3D printed sample sintered for 40 hrs.

An important thing to note here is the visual analysis of the indent. In a few cases, the whole region below the surface was found to be hollow after the test was conducted. The whole region would crumble down after indentation in such cases. Fig. 3-43 depicts an image of one such test, where we can see the whole region been cracked. Also, the cracks lead to nearest deformity and the whole area is disrupted. Fig. 3-44 shows the SEM image of crack nucleation from a microindent on 40 hrs. sintered sample.

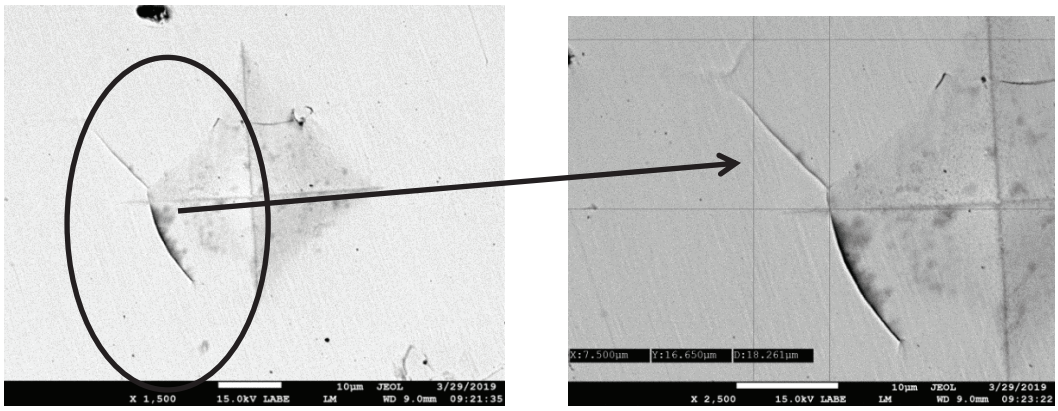

(a) (b)

Figure 3-44 SEM image of microindent: (a) indent profile, (b) crack measurement for sample-2

It can be seen that the crack is not in line with the diagonal of indent and was found to be rather perpendicular to the diagonal. One of the reasons for such behavior is suspected to be due to crack propagation along the grain boundary. As the grain size is smaller it is easier for material to crack through the boundaries rather than through the material. The crack lengths from various tests are documented in Table 3-16 below.

Table 3-16 Average crack lengths for 40 hrs. sintered sample

Sample type	Average diagonal length (m)	Crack length (m)	Total crack length (m)
40 hrs. sintered 3D printed sample	0.00002571	0.00001651	0.00004222
	0.00001929	0.00001494	0.00003423
	0.00002321	0.00001826	0.00004147
	0.00002036	0.00002821	0.00004857
	0.00002107	0.000035102	0.000056172
	0.0000211	0.00001726	0.00003836
	0.00002	0.000016415	0.000036415
	0.0000222	0.0000218	0.000044

Sample type	Average diagonal length (m)	Crack length (m)	Total crack length (m)
40 hrs. 3D printed sample	0.0000176	0.00000879	0.00002639
	0.00001964	0.0000165	0.00003614
Avg value	**0.000021018**	**1.93787E-05**	**4.03967E-05**

Consistency was found in crack lengths as compared to 24 hrs. sintered sample. And thus, there were again five different models based on Vickers indenter used to determine the stress concentration constant (K_{IC}). It includes three models based on radial crack while two models are based on Palmqvist crack.

Calculations:

From Fig. 3-37 (a) and (b) the following information were found:

Avg. diagonal length (a) = 0.000002571 m, crack length (l) = 0.00001651 m

❖ **Anstsis model: (radial crack)**

Equation is given as: $$K_{IC} = A * \left(\frac{E}{H}\right)^{1/2} * \left[\frac{P}{c^{\frac{3}{2}}}\right]$$

A = 0.016 (radial crack model), E = 33.67 GPa, H = 1.97 GPa, P = 1.25 N, c = 0.00004222 m (total crack length = avg. diagonal length + crack length)

$$K_{IC} = 0.016 * \left(\frac{(33.67)}{(1.97)}\right)^{\frac{1}{2}} * \frac{1.25}{0.00004222^{3/2}}$$

$$K_{IC} = \mathbf{0.3014\ Pa\sqrt{m}}$$

❖ **Laugier's model (radial crack):**

Equation is given as: $$K_{IC} = X_v * \left(\frac{a}{l}\right)^{\frac{1}{2}} * \left(\frac{E}{H}\right)^{\frac{2}{3}} * \left(\frac{P}{c^{\frac{3}{2}}}\right)$$

X_v = 0.01, a = 0.00002571 m, l = 0.00001651 m

$$K_{IC} = 0.01 * \left(\frac{(0.00002571)}{(0.00001651)}\right)^{\frac{1}{2}} * \left(\frac{(33.67)}{(1.97)}\right)^{2/3} \frac{1.25}{0.00004222^{3/2}}$$

K_{IC} = **0.3023 Pa√m**

❖ **Laugier's model (Palmqvist crack):**

Equation is given as: $$K_{IC} = X_v * \left(\frac{a}{l}\right)^{\frac{1}{2}} * \left(\frac{E}{H}\right)^{\frac{2}{3}} * \left(\frac{P}{c^{\frac{3}{2}}}\right)$$

X_v = 0.0089, a = 0.00002571 m, l = 0.00001651 m

$$K_{IC} = 0.0089 * \left(\frac{(0.00002571)}{(0.00001651)}\right)^{\frac{1}{2}} * \left(\frac{(33.67)}{(1.97)}\right)^{2/3} \frac{1.25}{0.00004222^{3/2}}$$

K_{IC} = **0.4566 Pa√m**

❖ **Niihara's model (radial crack):**

Equation is given as: $$K_{IC} = X_v * \left(\frac{E}{H}\right)^{\frac{2}{3}} * \left(\frac{P}{c^{\frac{3}{2}}}\right)$$

X_v = 0.0309

$$K_{IC} = 0.0309 * \left(\frac{(33.67)}{(1.97)}\right)^{\frac{1}{2}} * \frac{1.25}{0.00004222^{3/2}}$$

K_{IC} = **0.4382 Pa√m**

❖ **Niihara's model (Palmqvist crack):**

Equation is given as: $$K_{IC} = X_v * \left(\frac{E}{H}\right)^{\frac{2}{3}} * \left(\frac{P}{c^{\frac{3}{2}}}\right)$$

$X_v = 0.0089$

$$K_{IC} = 0.0089 * \left(\frac{(33.67)}{(1.97)}\right)^{\frac{1}{2}} * \frac{1.25}{0.00004222^{3/2}}$$

$$K_{IC} = \mathbf{0.4119\ Pa\sqrt{m}}$$

Results obtained for fracture toughness are shown in Table 3-17.

Table 3-17 Fracture toughness results for 40 hrs. sintered 3D printed sample

Sr. no.	Model	K_{IC} (radial) average value (Pa√m)	K_{IC} (Palmqvist) average value (Pa√m)
1	Anstis	0.3462±0.1136	
2	Laugier	0.3473±0.1139	0.5895±0.235
3	Niihara	0.5035±0.165	0.4119±0.113
	Avg.	**0.399±0.0905**	**0.5007±0.1255**

There was an appreciable amount of decrease in the fracture toughness value of 40 hrs. sintered sample, compared to the 24 hrs. sintered sample. One of the important reasons is the increase in sintering time of the material, as well as chances of oxidation during the sintering process. Radial crack model for Vickers indenter is considered more accurate than the Palmqvist model. [42] So, the result for the radial crack model is considered as a fracture toughness value for 40 hrs. sintered sample.

3.5.3.3 Sample-3 (sintered 50 hrs.)

This sample was sintered for the longest time and was comparatively denser than all the other 3D printed samples. Although it had more area to conduct the microindentation test, it was found to be more brittle as compared to other samples. Indent profile and the crack length measured using SEM is shown in Fig. 3-45 (a) - (c).

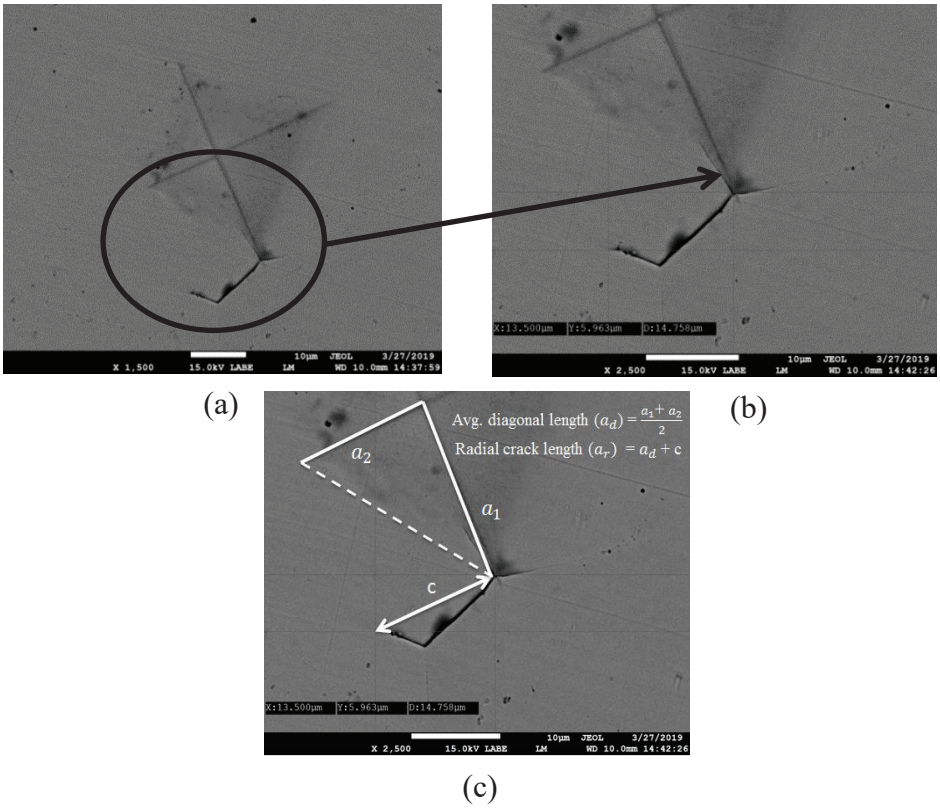

Figure 3-45 SEM image: (a) microindent profile, (b) crack detail, and (c) radial crack length measurement

It is important to note here, that the crack propagation is suspected to be along the grain boundary first rather than across the grains. This was derived from the crack propagation in the material which was found to be not in line with the diagonal of the indent. Thus, the radial crack length was calculated by taking the sum of average crack length and

crack length outside the indent, as shown in Fig. 3-45. The average crack lengths for sample 3 are documented in Table 3-18 with respective standard deviation in the results.

Table 3-18 Crack length measurement

Sample type	Average diagonal length (m)	Crack length (m)	Total crack length (m)
3D printed sample sintered 50 hrs.	0.0000206	0.0000144	0.000035
	0.00001929	0.00001956	0.00003885
	0.0000225	0.00003125	0.00005375
	0.00002217	0.00003344	0.00005561
	0.0000276	0.00005826	0.00008586
	0.00001153	0.0000123	0.00002383
	0.00002391	0.00002769	0.0000516
Avg value	**2.10857E-05**	**2.81286E-05**	**4.92143E-05**

Results obtained for 50 hrs. sintered sample are shown in Table 3-19. In comparison to the 40 hrs sintered sample, the value is not much different. This again leads us to the fact that with an increase in the sintering time the decrease in fracture toughness reduced. By comparing the fracture toughness results from 40 and 50 hrs. sintered sample, it was found that the value for stress concentration factor (K_{IC}) was close to each other, however, had a small standard deviation in results from radial crack models.

Table 3-19 Fracture toughness results for 50 hrs. sintered 3D printed sample

Sr. no.	Model	K_{IC} (radial) average value (Pa√m)	K_{IC} (Palmqvist) average value (Pa√m)
1	Anstis	0.3125±0.2	
2	Laugier	0.3135±0.201	0.4565±0.324
3	Niihara	0.4544±0.292	0.3961±0.235
	Avg.	**0.360±0.0816**	**0.4263±0.0427**

Also, for Vickers indenter the radial crack model is considered more reliable and so fracture toughness for 3D printed sample is considered to be in a range of 0.3 to 0.5 Pa√m.

Table 3-20 Percentage difference in different models based on radial crack

	Radial crack			
	3D printed samples			
		50 hrs	40 hrs	% difference between 50 hrs and 40 hrs
	Anstis	0.3125 Pa√m	0.3463 Pa√m	10.816
	Laugier	0.3135 Pa√m	0.3473 Pa√m	10.78
	Niihara	0.4544 Pa√m	0.5034 Pa√m	10.78
Laugier	% diff w.r.t. Anstis	0.32	0.288	
Niihara	% diff w.r.t. Anstis	45.408	44.94	

Results for 24 hrs. sintered sample is not so convincing, due to less reliability of Palmqvist model used for calculation. Also, the surface of sample-1 has larger pores which are not favorable for fracture toughness test through indentation, as chances of errors increase while conducting the tests. For further analysis, FIB should be done on various samples, and the actual stress area under the surface should be analyzed.

The percentage difference in the results was determined as previously evaluated for bulk samples. There was good consistency found in the 3D printed samples, for 40 hrs. and 50 hrs. sample. Table 3-20 and 3-21 documents the results obtained for both radial and Palmqvist models.

Table 3-21 Percentage difference in different models based on Palmqvist crack

	Palmqvist crack			
	3D printed samples			
		50 hrs	40 hrs	% difference between 50 hrs and 40 hrs
	Laugier	0.456 Pa√m	0.5896 Pa√m	29.29
	Niihara	0.396 Pa√m	0.4119 Pa√m	4.015
Laugier	% diff w.r.t. Niihara	13.15	30.13	

3.5.4 Stress comparison

Previously, it was suspected that the load used for yielding the bulk material was not enough. To thoroughly analyze this fact, stresses from the yield strength testing for the maximum load using nanoindentation, and the stresses obtained from the fracture toughness test were calculated to get an idea about the difference in the stress value.

True stress calculation from yield strength test done on bulk Ni-Mn-Ga sample using nanoindentation:

The true stress for the material is defined as the ratio of load applied with the change in the instantaneous area. But, in the case of flat tip indenter, the area (A_i) of contact is always constant. So, the stress can be given as equation (3.2). [49]

$$\boldsymbol{\sigma_T = \frac{F}{A_i}} \tag{3.1}$$

For bulk samples: F = 0.4 N, radius of tip (r) = 10 µm = 10^{-5} m, $A_i = 3.14 * (r)^2 = 3.141 \times 10^{-10}$ m^2

$$\sigma_T = \frac{0.4}{3.141 \times 10^{-10}}$$

$$\sigma_T = 1273479780 \frac{N}{m^2}$$

$$\sigma_T = 1.27 \text{ GPa}$$

Fracture stress from microindentation test done for bulk Ni-Mn-Ga part:

The stress calculation from the microindent can be calculated if the depth of indent (h) can be accurately defined. The projected area for Vickers indenter is given by [34]

$$A = 24.5 (h^2) \tag{3.2}$$

From the projected area the stress can be calculated using the same equation (9), used for calculation stress from yield strength data. But, the microhardness tester had no facility to track the maximum depth with respect to load apply. So, the approach here is to determine the depth of indent from the relation between the indent diagonal and the maximum depth of indent. The model suggested by the author defines that if elastic recovery is not taken into consideration, the relation between the depth of indent (h) and length of diagonal (a) is given by (3.3), for a typical Vickers indenter having a face angle of 136°. [50] Here, 'a' was defined from the diagonal length of one of the tests done on the austenitic sample as shown in Fig. 3-38

$$a = 7 * h \tag{3.3}$$

Using the assumption and model suggested, the stresses for bulk samples were calculated.

Bulk sample

a = 0.0003 m, h = a/ 7 = 4.286 x 10^{-10} m, F = 92.8 N,

$$\sigma_F = \frac{92.8}{24.5 * (4.286 * 10^{-10})^2}$$

$$\sigma_F = 2061947287 \ \frac{N}{m^2}$$

$$\sigma_F = 2.062 \text{ GPa}$$

Comparing the results, the fracture stress is considerably high as compared to the stress from the yield strength test. Although the scales for testing were different, still the stresses were calculated in accordance with the material volume indented and so the results can still be valid. This confirms the material would not yield at such a low load (400 mN) available in the nanoindentation machine. Another important aspect about

brittle material is the yield stress and fracture stress is almost equal, as there is a negligible amount of yielding in brittle. So, in conclusion, it can be determined that the maximum load on the nanoindentation instrument was not enough to yield the Ni-Mn-Ga material, and the assumption made before is convincing.

3.6 Setup and results for numerical modeling

3.6.1 Boundary conditions

The model was simulated using a static structural module in ANSYS 19.1, to reduce the complexity in the process. There were two constraints used for this model, including the support to the model and the displacement of the indenter. Here, the bottom edge of the material was fixed to prevent any movement of the part while the nanoindentation process. The second constraint was used as a remote displacement of indenter with an increase in time as per defined by the user. This was done to replicate the actual indentation process where there is a very slow loading of indenter with respect to time. To define the motion of the indenter, increment in the displacement of 0.0005 inches was given in 0.005 seconds. Fig. 3-46 is the image of the model with constraints. MS Excel 2010 was used to determine displacement in 22 time steps till reaching the maximum time of 1 second. This incremental displacement could be given to either the top edge of the indenter or the plane of the indenter. In both cases, the indenter displacement would be the same.

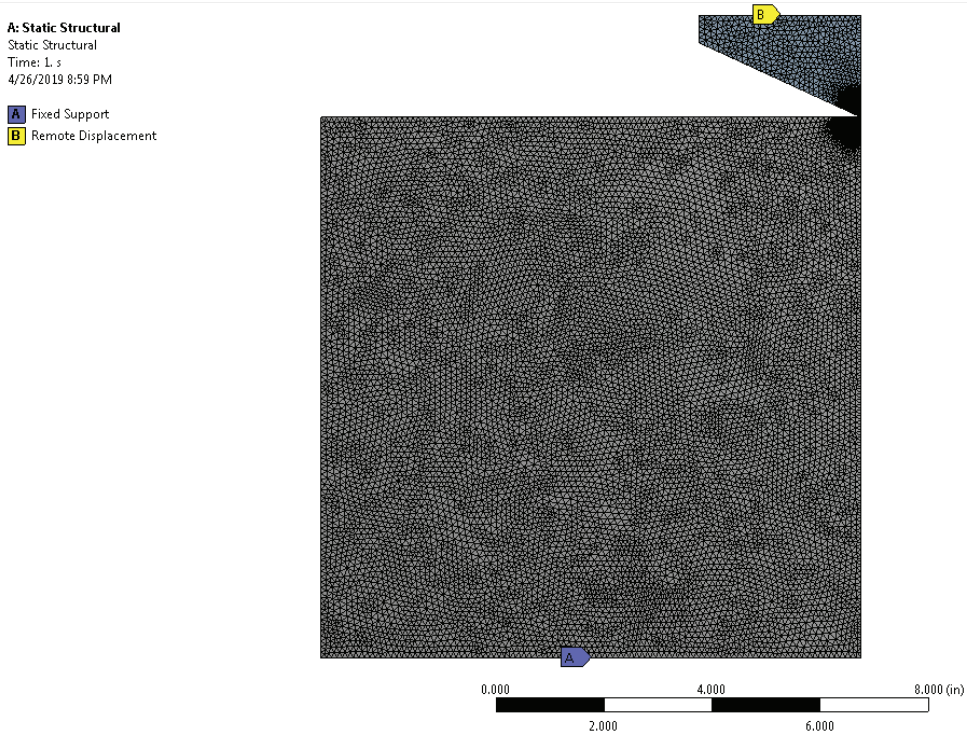

Figure 3-46 Constraints on model

Here, a question might arise, why was full indenter geometry and body part was not used? But the only reason for that is to reduce the simulation time. The results could be also verified by using the 2D axisymmetric operation to check the deformation and strain in the material.

3.6.2 Numerical modeling results

The modeling results confirmed two things for which the simulation was conducted. The first was to investigate the material stress at the indenter tip, while the second was to see the maximum strain due to the indentation testing. As shown in Fig. 3-47, the FEA result confirms that the maximum strain in material occurs right below the contact of the indenter tip. This hoop stress produced below the indenter, later on, becomes the reason for the material failure. [11] Also, the shape of the stress produced is close to a semicircle.

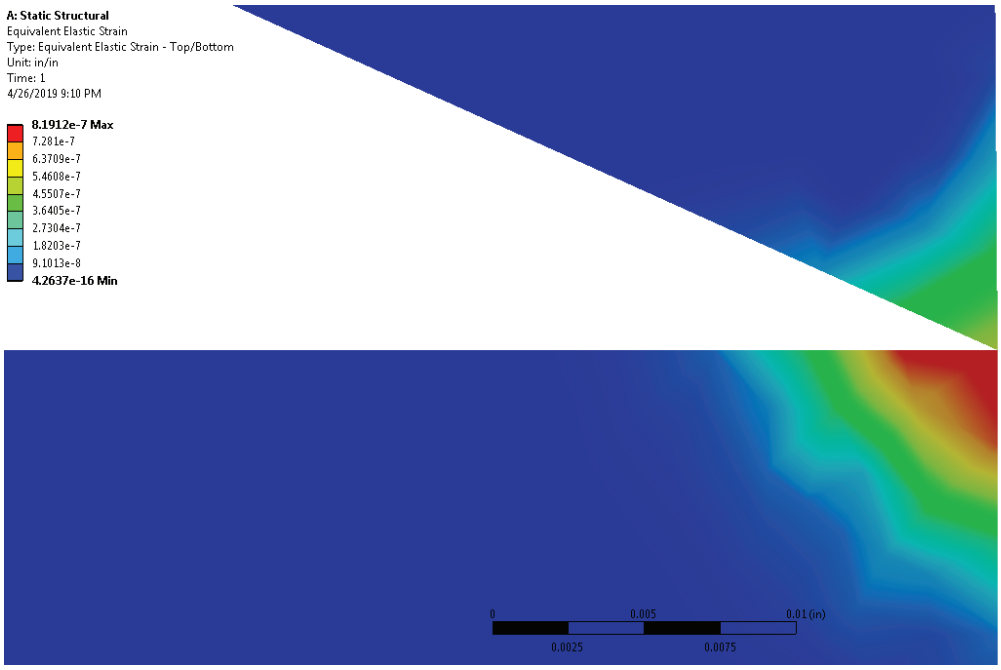

Figure 3-47 FEA results for maximum strain in the material

This confirms the assumption of the half-penny area produced under the surface due to indentation while fracture toughness tests and so radial crack models are more reliable than Palmqvist crack**.**

Chapter 4 Conclusions and future work

The mechanical properties for 3D printed parts were found to be weak, as compared to the bulk polycrystalline Ni-Mn-Ga alloy. The high porosity in 3D printed material affected the mechanical strength as well as the material resistance to cracking. After testing the three different types of samples using nanoindentation and microindentation technique it can be concluded that:

- Hardness for the austenitic phase sample was found to be higher than martensitic and 3D printed samples.
- Elastic modulus of the martensitic sample was highest among the samples. The large standard deviation might be explained by the existence of surface irregularities (related to the surface morphology of the twin boundaries) and crystallographic orientation of individual grains
- For the bulk parts, the maximum load available in the nanoindentation instrument (400 mN) was not sufficient to produce the yield. The yield stress (σ_y) estimated from microhardness experiments for the austenitic sample was about 2.06 GPa.
- 3D printed materials were weak as compared to the bulk parts and had a yield strength (σ_y) of 545.5 MPa.
- Pseudoelastic behavior was observed in both bulk and 3D printed materials during experiments using a sharp indenter which is unique for nanoindentation testing.
- Fracture toughness values for 3D printed samples were found to be lower as compared to the bulk part, due to the material porosity.

- Sintering time for 3D printed sample affects the fracture toughness of the material. The increased sintering time might produce the oxygen segregation and the weakening of the grain boundaries in the printed material.
- Future work includes determining a model or a technique to convert the load versus depth data to true stress-strain data in order to quantify the strain recovery and to asses the pseudoelastic effect.
- Also, crystallographic analysis using electron backscattered diffraction (EBSD) technique to correlate mechanical properties with different grain orientations.
- To directly determine the stress-induced phase transition during the nanoindentation experiments.

References

[1] Y. Ge, O. Heczko, O. Söderberg, and V. K. Lindroos, "Various magnetic domain structures in a Ni–Mn–Ga martensite exhibiting magnetic shape memory effect," *J. Appl. Phys.*, vol. 96, no. 4, pp. 2159–2163, Aug. 2004.

[2] J. Liu, N. Scheerbaum, S. Kauffmann- Weiss, and O. Gutfleisch, "NiMn-Based Alloys and Composites for Magnetically Controlled Dampers and Actuators," *Adv. Eng. Mater.*, vol. 14, no. 8, pp. 653–667, 2012.

[3] H. Hosoda, S. Takeuchi, T. Inamura, and K. Wakashima, "Material design and shape memory properties of smart composites composed of polymer and ferromagnetic shape memory alloy particles," *Sci. Technol. Adv. Mater.*, vol. 5, no. 4, p. 503, Jul. 2004.

[4] A. Annadurai, "Experimental investigations on the nanomechanical properties of sputter deposited Ni-Mn-Ga ferromagnetic shape memory thin films," *Int. J. Eng. Technol.*, vol. 4, no. 4, p. 4, 2012.

[5] Y. Aydogdu, A. S. Turabi, M. Kok, A. Aydogdu, H. Tobe, and H. E. Karaca, "Effects of the substitution of gallium with boron on the physical and mechanical properties of Ni–Mn–Ga shape memory alloys," *Appl. Phys. A*, vol. 117, no. 4, pp. 2073–2078, Dec. 2014.

[6] A. Jayaraman, M. S. R. N. Kiran, and U. Ramamurty, "Mechanical Anisotropy in Austenitic NiMnGa Alloy: Nanoindentation Studies," *Crystals*, vol. 7, no. 8, p. 254, Aug. 2017.

[7] L. Zhou, A. Giri, K. Cho, and Y. H. Sohn, “A Combinatorial Study for Interdiffusion, Crystallography and Mechanical Behavior of Ni-Mn-Ga Alloys,” *Defect Diffus. Forum*, vol. 371, pp. 153–159, Feb. 2017.

[8] L. Gao, W. Cai, A. L. Liu, and L. C. Zhao, “Martensitic transformation and mechanical properties of polycrystalline Ni50Mn29Ga21−xGdx ferromagnetic shape memory alloys,” *J. Alloys Compd.*, vol. 425, no. 1, pp. 314–317, Nov. 2006.

[9] I. Aaltio *et al.*, “Nanoscale surface properties of a Ni–Mn–Ga 10M magnetic shape memory alloy,” *J. Alloys Compd.*, vol. 577, pp. S367–S371, Nov. 2013.

[10] L. Zhou, A. Giri, K. Cho, and Y. Sohn, “Mechanical anomaly observed in Ni-Mn-Ga alloys by nanoindentation,” *Acta Mater.*, vol. 118, pp. 54–63, Oct. 2016.

[11] V. Goanţă and C. Ciocanel, “Fracture Toughness Evaluation of a Ni2MnGa Alloy Through Micro Indentation Under Magneto-Mechanical Loading,” *ACTA Univ. Cibiniensis*, vol. 69, no. 1, pp. 89–99, Dec. 2017.

[12] M. Kohl, D. Brugger, M. Ohtsuka, and T. Takagi, “A novel actuation mechanism on the basis of ferromagnetic SMA thin films,” *Sens. Actuators Phys.*, vol. 114, no. 2, pp. 445–450, Sep. 2004.

[13] S. Vinodh Kumar, M. Mahendran, M. Manivel Raja, V. L. Niranjani, and P. K. Mukhopadhyay, “Phase structure evolution on Ni-Mn-Ga/Si (100) thin films: Effect of substrate temperature,” *Intermetallics*, vol. 101, pp. 18–26, Oct. 2018.

[14] S. V. Kumar, R. K. Singh, M. M. Raja, A. Kumar, S. Bysakh, and M. Mahendran, “Microstructure and nanomechanical properties of Mn-rich Ni–Mn–Ga thin films,” *Intermetallics*, vol. 71, pp. 57–64, Apr. 2016.

[15] C. Liu, Z. Y. Gao, X. An, H. B. Wang, L. X. Gao, and W. Cai, “Surface characteristics and nanoindentation study of Ni–Mn–Ga ferromagnetic shape memory sputtered thin films,” *Appl. Surf. Sci.*, vol. 254, no. 9, pp. 2861–2865, Feb. 2008.

[16] O. L. Warren and T. J. Wyrobek, “Nanomechanical property screening of combinatorial thin-film libraries by nanoindentation,” *Meas. Sci. Technol.*, vol. 16, no. 1, pp. 100–110, Dec. 2004.

[17] M. Chmielus, X. X. Zhang, C. Witherspoon, D. C. Dunand, and P. Müllner, “Giant magnetic-field-induced strains in polycrystalline Ni–Mn–Ga foams,” *Nat. Mater.*, vol. 8, no. 11, pp. 863–866, Nov. 2009.

[18] A. Mostafaei *et al.*, “Microstructural evolution and magnetic properties of binder jet additive manufactured Ni-Mn-Ga magnetic shape memory alloy foam,” *Acta Mater.*, vol. 131, pp. 482–490, Jun. 2017.

[19] M. P. Caputo, A. E. Berkowitz, A. Armstrong, P. Müllner, and C. V. Solomon, “4D printing of net shape parts made from Ni-Mn-Ga magnetic shape-memory alloys,” *Addit. Manuf.*, vol. 21, pp. 579–588, May 2018.

[20] M. Caputo, M. Krizner, and C. V. Solomon, “Investigation Of 3D Printing Parameters Of Shape Memory Alloy Powders.” MS&T, 2015.

[21] M. Caputo, C. V. Solomon, P.-K. Nguyen, and A. E. Berkowitz, “Electron Microscopy Investigation of Binder Saturation and Microstructural Defects in Functional Parts Made by Additive Manufacturing,” *Microsc. Microanal.*, vol. 22, no. S3, pp. 1770–1771, Jul. 2016.

[22] L. Zhou and Y. H. Sohn, “Diffusion and its Application in NiMnGa Alloys,” *Diffusion Foundations*, 2019. [Online]. Available: https://www.scientific.net/DF.19.80. [Accessed: 05-Mar-2019].

[23] J. Mohd Jani, M. Leary, A. Subic, and M. A. Gibson, “A review of shape memory alloy research, applications and opportunities,” *Mater. Des. 1980-2015*, vol. 56, pp. 1078–1113, Apr. 2014.

[24] O. Gutfleisch, M. A. Willard, E. Brück, C. H. Chen, S. G. Sankar, and J. P. Liu, “Magnetic Materials and Devices for the 21st Century: Stronger, Lighter, and More Energy Efficient,” *Adv. Mater.*, vol. 23, no. 7, pp. 821–842, Feb. 2011.

[25] M. A. Willard, F. Johnson, J. Claassen, R. Stroud, M. McHenry, and V. Harris, “Soft Magnetic Nanocrystalline Alloys for High Temperature Applications,” *Mater. Trans.*, vol. 43, no. 8, pp. 2000–2005, 2002.

[26] A. Gebert, S. Roth, S. Oswald, and L. Schultz, “Passivity of polycrystalline NiMnGa alloys for magnetic shape memory applications,” *Corros. Sci.*, vol. 51, no. 5, pp. 1163–1171, May 2009.

[27] N. Hansen, “Hall–Petch relation and boundary strengthening,” *Scr. Mater.*, vol. 51, no. 8, pp. 801–806, Oct. 2004.

[28] I. Weißensteiner, P. Voigt, H. Clemens, and V. Maier-Kiener, “Strain-Induced Martensitic Transformation in a Co-Cr-W-Mo Alloy Probed by Nanoindentation,” in *Proceedings of the International Conference on Martensitic Transformations: Chicago*, A. P. Stebner and G. B. Olson, Eds. Cham: Springer International Publishing, 2018, pp. 247–250.

[29] Eduardo Vega-Lozada, Issaco Stephen, and Samuel Mistretta, "Failure Analysis report on Additive Manufacturing of Shape Memory Alloy Ni-Mn-Ga, for MECH 6915 Failure Analysis class." Youngstown State University, Apr. 2018.

[30] M. Caputo, "4-Dimensional Printing and Characterization of Net-shaped Porous Parts Made from Magnetic Ni-Mn-Ga Shape Memory Alloy Powders," PhD Thesis, Youngstown State University, 2018.

[31] Y. Ge, O. Heczko, O. Söderberg, and S.-P. Hannula, "Magnetic domain evolution with applied field in a Ni–Mn–Ga magnetic shape memory alloy," *Scr. Mater.*, vol. 54, no. 12, pp. 2155–2160, Jun. 2006.

[32] "A review of nanoindentation continuous stiffness measurement technique and its applications - ScienceDirect." [Online]. Available: https://www.sciencedirect.com/science/article/pii/S1044580302001924. [Accessed: 16-Apr-2019].

[33] "Measurement of hardness and elastic modulus by instrumented indentation: Advances in understanding and refinements to methodology | Journal of Materials Research | Cambridge Core." [Online]. Available: https://www.cambridge.org/core/journals/journal-of-materials-research/article/measurement-of-hardness-and-elastic-modulus-by-instrumented-indentation-advances-in-understanding-and-refinements-to-methodology/D81F6EBA71598A8C6EE338BF5A3D5AE7. [Accessed: 16-Apr-2019].

[34] A. C. Fischer-Cripps, *Nanoindentation*, 3rd ed. New York: Springer, 2011.

[35] X.-L. Gao, “An expanding cavity model incorporating strain-hardening and indentation size effects,” *Int. J. Solids Struct.*, vol. 43, no. 21, pp. 6615–6629, Oct. 2006.

[36] M. Rodríguez, J. M. Molina-Aldareguía, C. González, and J. LLorca, “Determination of the mechanical properties of amorphous materials through instrumented nanoindentation,” *Acta Mater.*, vol. 60, no. 9, pp. 3953–3964, May 2012.

[37] J. J. Mecholsky, “Fracture mechanics principles,” *Dent. Mater.*, vol. 11, no. 2, pp. 111–112, Mar. 1995.

[38] K. Niihara, R. Morena, and D. P. H. Hasselman, “Evaluation of brittle solids by the indentation method with low crack-to-indent ratios,” *J. Mater. Sci. Lett.*, vol. 1, no. 1, pp. 13–16, Jan. 1982.

[39] G. M. Pharr, D. S. Harding, and W. C. Oliver, “Measurement of Fracture Toughness in Thin Films and Small Volumes Using Nanoindentation Methods,” in *Mechanical Properties and Deformation Behavior of Materials Having Ultra-Fine Microstructures*, M. Nastasi, D. M. Parkin, and H. Gleiter, Eds. Dordrecht: Springer Netherlands, 1993, pp. 449–461.

[40] B. R. Lawn and A. G. Evans, “A model for crack initiation in elastic/plastic indentation fields,” *J. Mater. Sci.*, vol. 12, no. 11, pp. 2195–2199, Nov. 1977.

[41] K. Niihara, “A fracture mechanics analysis of indentation-induced Palmqvist crack in ceramics,” *J. Mater. Sci. Lett.*, vol. 2, no. 5, pp. 221–223, May 1983.

[42] D. Casellas, J. Caro, S. Molas, J. M. Prado, and I. Valls, “Fracture toughness of carbides in tool steels evaluated by nanoindentation,” *Acta Mater.*, vol. 55, no. 13, pp. 4277–4286, Aug. 2007.

[43] M. Kasper, “G.W.H. Höhne, W.F. Hemminger, H.-J. Flammersheim: Differential scanning calorimetry,” *Anal. Bioanal. Chem.*, vol. 380, no. 3, pp. 366–367, Oct. 2004.

[44] “Errors in FEA and Understanding Singularities (Beginners’ Guide),” *SimScale*, 30-Jun-2016. [Online]. Available: https://www.simscale.com/blog/2016/06/errors-in-fea-and-singularities/. [Accessed: 26-Apr-2019].

[45] International Standard (ISO 14577-1), "Metallic materials - Instrumented indentation test for hardness and materials parameters" ISO, 01-Oct-2002.

[46] S. Glock, L. P. Canal, C. M. Grize, and V. Michaud, “Magneto-mechanical actuation of ferromagnetic shape memory alloy/epoxy composites,” *Compos. Sci. Technol.*, vol. 114, pp. 110–118, Jun. 2015.

[47] H. E. Karaca, I. Karaman, A. Brewer, B. Basaran, Y. I. Chumlyakov, and H. J. Maier, “Shape memory and pseudoelasticity response of NiMnCoIn magnetic shape memory alloy single crystals,” *Scr. Mater.*, vol. 58, no. 10, pp. 815–818, May 2008.

[48] T. F. Juliano, M. R. VanLandingham, T. Weerasooriya, and P. Moy, “Extracting Stress-Strain and Compressive Yield Stress Information From Spherical Indentation,” p. 24, Army research laboratory, Sept. 2007.

[49] William D. Callister Jr., *Reference Materials Science and Engineering an Introduction*, 5th ed. John Wiley & Sons, Inc., 2000.

[50] E. Broitman, “Indentation Hardness Measurements at Macro-, Micro-, and Nanoscale: A Critical Overview,” *Tribol. Lett.*, vol. 65, no. 1, Mar. 2017.